HIGH ENERGY DENSITY CATHODE FOR LITHIUM BATTERIES:

FROM $LiCOO_2$ TO SULFUR

A Dissertation

by

XIONG PU

Submitted to the Office of Graduate and Professional Studies of
Texas A&M University
in partial fulfillment of the requirements for the degree of

DOCTOR OF PHILOSOPHY

Chair of Committee,	Choongho Yu
Committee Members,	Perla Balbuena
	Haiyan Wang
	Partha Mukherjee
Head of Department,	Ibrahim Karaman

August 2014

Major Subject: Materials Science and Engineering

ABSTRACT

Lithium batteries are receiving increasing interest worldwide due to the urgent demand for higher energy density, longer cycling life, cheaper price, and better safety, so that long-distance electric vehicles and stationary energy storages can be viable. This dissertation, motivated with these aims, investigated both Li-ion batteries and Li-S batteries.

$LiCoO_2$, though it has been commercialized in Li-ion batteries, still has the potential to achieve higher energy density, since its practical capacity is limited to half of its theoretical capacity due to the overcharge problem. Surface coatings of lithium vanadate (Li_3VO_4) on $LiCoO_2$ nanoparticles were employed to overcome this issue. With 3.4-wt.% and 5.5-wt.% Li_3VO_4 coatings, both the cyclability and high-rate capability of $LiCoO_2$ cells were greatly improved when overcharged to voltages as high as 4.5 V and 4.7 V. The improvement was attributed to the structurally protective and Li-ion conductive Li_3VO_4 coating, which can suppress the side reaction and structure damage of $LiCoO_2$ nanoparticles, as indicated by TEM images after the cycling test.

Li-S batteries, promising due to the high energy density and low price, face two challenges that have not been well addressed, i.e. the safety hazard resulted from the Li dendrite formation on the Li metal anode and the poor cyclability arising from the polysulfides shuttle. Firstly, to overcome the safety issue, this dissertation reported a lithiated Si-S (LSS) battery that replaced the Li metal with a pre-lithiated Si anode. Due to the high theoretical capacity of Si, no sacrifice of the energy density was made. Stable cycling performances with capacity retention up to 80% were achieved in the organic electrolyte. The better safety of the LSS battery in terms of external and internal short-circuits was also demonstrated. Secondly, to suppress the polysulfides shuttle, a novel semi-liquid Li-S battery was designed with carbon nanotubes (CNT) sponges soaked by

liquid polysuflides as the cathode. Stable cycling performances were achieved over 300 cycles. Due to the absence of the polymer binder and metal current collector in this design, the energy density of the total electrode was improved significantly.

ACKNOWLEDGEMENTS

First, I'd like to sincerely thank my supervisor, Dr. Choongho Yu, for his patient guidance, support, advice and inspiration to my research throughout last four years. Dr. Yu's enthusiasm and commitment to the research is what I need to carry on in my future career. I also truly appreciate the help and suggestions from my committee members, Dr. Haiyan Wang, Dr. Perla Balbuena, and Dr. Partha Mukherjee.

Also, many thanks go to the members of Dr. Yu's group, Dr. Liang Yin, Dr. Hong Wang, Dr. Kyungwho Choi, Dr. Yeontack Ryu, Dr. Sang-Won Jee, Woongchul Choi, Gang Yang, Abdullah S Tazebay, Jui-Hung Hsu, Suk Lae Kim, Su-In Yi, Fang Hu, for their friendship and support. I'd like to thank Dr. Liang Yin and Dr. Miao Song's help on TEM and STEM analysis. I also thank Dr. Arum Han, Dr. Mi-jin Choi, and Celal Erbay for their collaboration and support.

I am grateful to my sponsor, China Scholarship Council, for their financial support throughout my research.

Lastly, I'd like to present my deep gratitude to my parents and my wife, for their numerous supports and sacrifices.

TABLE OF CONTENTS

Page

LIST OF FIGURES

LIST OF TABLES

Page

CHAPTER I

INTRODUCTION AND LITERATURE REVIEW

1.1 Fundamentals of electrochemical energy conversions

Electrochemical power sources, comparing with energy generation from combustion of fossil fuels and biomass, are receiving increasing interest and investigations worldwide as long as they are more sustainable and environmentally friendly. Electrochemical power sources refer to devices that convert chemical energy into electricity. Their conversion efficiencies are generally higher than that of combustion engine. There are mainly three types of systems for electrochemical energy conversions: batteries, electrochemical capacitors (i.e. supercapacitors or ultracapacitors), and fuel cells.

They all have two electrodes (i.e. cathode and anode) separated by an ion-conductive but electron-insulating electrolyte. During the process of energy conversion, the electrons and ions separate at the electrolyte/electrode interface of one electrode, transport through the external circuit and electrolyte respectively, and then combine at the other electrode. Batteries and electrochemical capacitors are both energy storage devices, which can store electrical energy chemically and convert it back to electricity; while fuel cells can't store electricity. Batteries and fuel cells always have redox reactions; while an electrochemical capacitor may only have the so-called electric double layer capacitance (EDLC), which is generated not by redox reaction but by the orientation of the ions at the electrode/electrolyte interface. When the surface of the capacitor electrodes is attached with a thin layer of redox species, faradic charges and thus the so-called pseudo-capacitance will be produced. Batteries and electrochemical capacitors have closed system; the fuel cells have open system, so that the fuel (H_2, CH_4, etc.) and oxidant (O_2) can be filled into anode and cathode, respectively. As shown in figure 1.1[1], fuel cell has energy density as high as that of combustion engine but the power density is the lowest among the three systems.

On the contrary, electrochemical capacitor can deliver/store energy at very high rate, though the energy density is generally smaller than that of batteries and fuel cells.

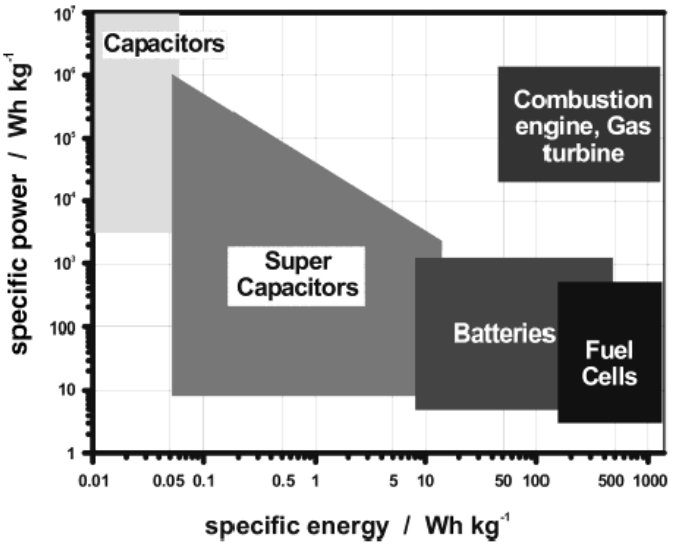

Figure 1.1 Ragone plot of three types of electrochemical energy conversion systems compared with combustion engine and traditional capacitors.[1] Adapted with permission from (Winter, M.; Brodd, R. J., What are batteries, fuel cells, and supercapacitors? *Chem. Rev.* 2004, 104 (10), 4245-4270). Copyright (2004) American Chemical Society.

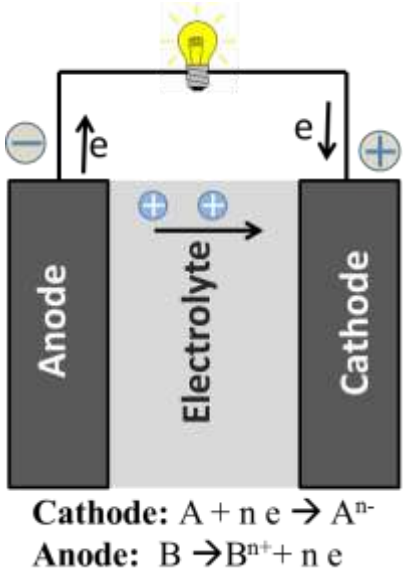

Figure 1.2 Schematic illustration of the discharge of an electrochemical cell

Though the detailed mechanisms of above three devices are different, they follow the same basic thermodynamic and kinetic formulations for their chemical reactions. For an electrochemical cell schemed in figure 1.2, the total cell reaction is:

$$A + B \rightarrow A^{n-} + B^{n+} \tag{1.1}$$

The Gibbs free energy of the reaction is ΔG^o when the reaction occurs at standard state at 25 ^oC and unit activity. Then the cell voltage can be written as

$$E^o = -\frac{\Delta G^o}{nF} \tag{1.2}$$

where n is the electrons transferred per mole of reactants, F is the faradic constant. Considering the effect of temperature and the activity of the products ($a_{A^{n-}}$, $a_{B^{n+}}$) and reactants (a_A, a_B), the cell voltage will be:

$$\mathrm{E} = E^o + \frac{\mathrm{RT}}{nF}\ln\left(\frac{a_{A^{n-}} a_{B^{n+}}}{a_A a_B}\right) \tag{1.3}$$

where R is the Boltzmann constant and T is the absolute temperature. Hence, the cell voltage and useful energy are determined by the cell reaction at equilibrium state.

Kinetic limitations should also be considered when the cell operates with an external loading. Polarizations or overpotentials cause the loss of energy. There are mainly three types of polarization as shown in figure 1.3[1]: (1) activation polarization, which refers to the kinetics of the redox reactions at electrode surface; (2) Ohmic polarization IR, which is due to the internal impedance; (3) concentration polarization, which relates to the limits of mass transport in the cell. Hence, the operational voltage of a cell should be written as:

$$E_{op} = E_{OCV} - \eta \tag{1.4}$$

where η represents the polarization, E_{OCV} is the open-circuit voltage at the equilibrium state. Figure 1.3 describes the typical voltage profile of electrochemical cell, showing the effect of the

three different polarizations during the cell operation. When the drawing current is larger (higher rate discharge), less energy will be converted into electricity, due to the higher Ohmic polarization.

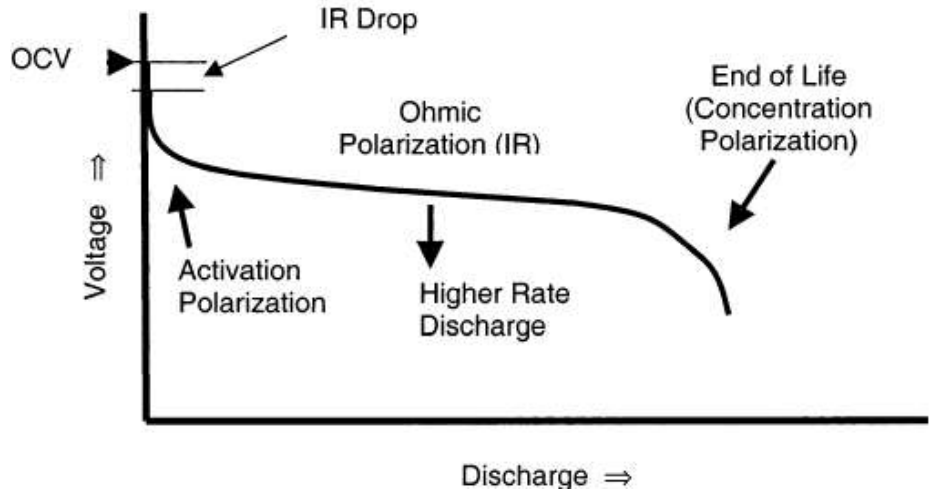

Figure 1.3 Typical discharge voltage profile of a battery showing different types of polarization.[1] Adapted with permission from (Winter, M.; Brodd, R. J., What are batteries, fuel cells, and supercapacitors? *Chem. Rev.* 2004, 104 (10), 4245-4270). Copyright (2004) American Chemical Society.

1.2 Lithium batteries

Batteries, due to their relatively high energy density and power density, are widely used as energy storage devices. In terms of reversibility, batteries can be divided into two categories: primary battery which has irreversible reactions and can only be discharged once, and secondary battery which is reversible and can be charged/discharged for many cycles. In terms of electrode materials, many different couples of electrodes have been designed. In this dissertation, only the secondary lithium batteries will be discussed.

1.2.1 Lithium ion batteries

1.2.1.1 History and working principles

The earliest design of lithium batteries coupled the anode of lithium metal or Li-Al alloy with the cathode of chalcogenides (TiS_2, etc.).[2] Later, efforts were tried to replace the metal anode because of the safety hazard caused by the lithium dendrite formation on the metal surface after repeated cycling, which leads to internal short-circuit and thermal runaway. In 1970s, carbonaceous materials (graphite, etc.) were developed to function as a host for the insertion of lithium ion at low potentials, and thus the lithium metal anode was replaced.[3] In 1980s, Goodenough[4] developed a layered-oxide ($LiCoO_2$) as the host of the insertion of lithium ion to replace chalcogenides, which showed both much higher capacity and voltage. These findings finally led to the first commercial lithium ion battery by SONY in 1991 with $LiCoO_2$ as cathode and carbon as anode. The intercalation mechanism refers to the insertion/extraction of lithium ions into the layered structure of electrode materials ($LiCoO_2$, graphite, etc.)

Li-ion batteries are typical rechargeable batteries that involve reversible transport of Li ions between the anode (negative) and cathode (positive) through the electrolyte, and electrons through the external circuit. During charging, the cathode releases Li ions into electrolyte and electrons into the external circuit, and is oxidized; the anode captures electrons and Li ions, and is reduced. During the discharging, the process is reversed. As for Lithium intercalation mechanism, Li ions will be hosted into the interstices between the layered lattice structures of the electrode materials. A schematic illustration of the operation of a Li-ion battery is shown in figure 1.4, where both the cathode and the anode are of Li intercalation mechanism.

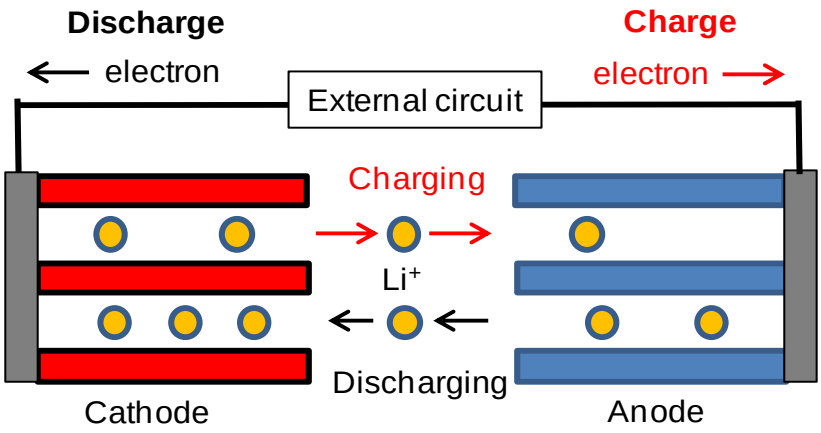

Figure 1.4 Schematic illustration of the operation of a Li-ion battery

Figure 1.5 shows the energy diagram of electrode materials and electrolyte of a battery. The cell voltage is determined by the potential or work function differences of the anode and cathode materials. It's better to choose the anode or cathode materials that have their redox potentials between the highest occupied molecular orbitals (HOMO) and lowest unoccupied molecular orbitals (LUMO) of the electrolyte, otherwise electrolyte will be oxidized or reduced at the electrolyte/electrode interface, forming a solid-electrolyte interface (SEI) layer, which consumes active materials and impedes the charge transfer. In other words, the maximum possible voltage of a Li-ion battery is also determined by the band gap of the electrolyte. Currently, organic solvents are widely used as electrolyte, and the maximum voltage for a single cell is around 5 V.

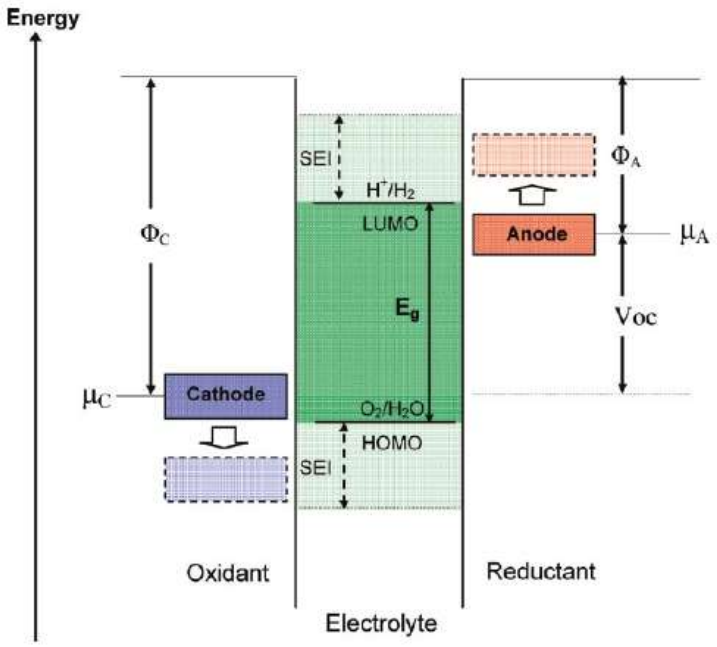

Figure 1.5 Schematic illustration of the open-circuit energy diagram of an aqueous battery cell. Φ_A, Φ_C refers to the work function of anode and cathode, E_g is the bandgap of the electrolyte, V_{OC} is the open-circuit voltage.[5] Adapted with permission from (Goodenough, J. B.; Kim, Y., Challenges for rechargeable Li batteries. *Chem. Mat.* 2009, 22 (3), 587-603). Copyright (2009) American Chemical Society.

Other than Li intercalation ($LiCoO_2$, graphite, $LiFePO_4$, $LiMnO_2$, etc.)[6], several other mechanisms of the redox reactions of active materials in Li-ion battery have also been investigated, i.e. Li alloying (Si, Sn, Ge, etc.)[7], and conversion reaction (metal oxides, metal sulfides, etc.)[8]. Representative electrode materials of different mechanisms are listed in table 1.1.

The operation of Li-ion batteries is mainly kinetically limited by the diffusion of the charges (electrons and Li ions) through the solid phase of active materials. Given enough time, Li ions and electrons will diffuse into the inner core of the active particles. According to kinetics, characteristic time constant (t) is given by $t = L^2/2D$,[9] where L and D is the diffusion length and the diffusion coefficient, respectively. Therefore, to have an electrode with excellent electrochemical performance, it is of key importance to reduce the diffusion lengths of charges

by reducing the size of active particles, and making porous electrode so as to have better contact of the electrolyte with the active materials. Meanwhile, most of the active materials in Li ion batteries have very low electrical conductivity, so light-weight conductive carbonaceous materials (carbon black, CNT, graphene, etc.) have been utilized as the conductive additives in the electrode. Therefore, a porous thin film of active materials mixed with carbon additives and polymer binder on metal current collector is the common design for the electrode in Li ion battery.

Table 1.1 Typical electrode materials in Li-ion batteries.

	Represent-atives	Reactions	Potential (V vs. Li/Li^+)	Theoretical capacity (mAh/g)
Lithium intercalation	$LiCoO_2$	$LiCoO_2 \rightleftharpoons Li_xCoO_2+(1-x)\ Li^+ + e^-$	~3.8	274
	$LiFePO_4$	$LiFePO_4 \rightleftharpoons FePO_4 + Li^+ + e^-$	~3.5	170
	Graphite	$LiC_6 \rightleftharpoons 6\ C + Li^+ + e^-$	0.1~0.2	372
Lithium alloying[10]	Si	$Li_{22}Si_5 \rightleftharpoons 5Si + 22Li^+ + 22\ e^-$	0.1~0.2	~4200
Conversion[8]	Metal oxides,	$MB_x + xy\ e^- + xy\ Li^+ \rightleftharpoons x\ Li_yB + M$ (M = Metal; B = S, O, P)	~1	800~1000

1.2.1.2 Cathode materials

Lithium layered oxides. $LiCoO_2$ is the cathode used in the first commercial Li-ion batteries[11] and still dominates the current market (more than 90% share in the market).[12] As shown in figure 1.6, $LiCoO_2$ has a layered structure same as α-$NaFeO_2$, with alternatively

stacked layers of CoO_2 and Li. Li^+ and Co^{3+} occupy the octahedral sites, and O^{2-} has a cubic close-packed array with ABCABC stacking sequence. The layered structure provides paths for fast diffusion of Li ions. The $Co^{4+/3+}$ redox couple has a ~4 V potential Vs. Li/Li^+. Meanwhile, it can be easily synthesized by solid state reaction. All these characteristics make it ideal for the cathode in lithium ion battery. However, there are also several disadvantages. First, cobalt is expensive due to its limited resources and is not environmentally friendly. Second, only half of the capacity of the $LiCoO_2$ can be utilized in practice. Theoretically, $LiCoO_2$ can yield a capacity of 272 mAh/g when fully delithiated. Whereas, when Li_xCoO_2 is delithiated to $x < 0.5$, a hexagonal-monoclinic transformation occurs.[13] Capacity fading is quick upon deep delithiation, due to the increased phase instability, loss of oxygen[14], and electrolyte decomposition.[15] Rate capability and structural instability of the layered oxide cathode materials can be improved by surface coating of inert thin layer of nanoscale metal oxides, such as Al_2O_3, RuO_2, MgO, and so on,[16] or by cationic/anionic substitution[17]. Meanwhile, the safety issue related to the cathodes can also be improved. For example, Sun *et al*. reported that with a new coating material AlF_3, the capacity retention and C-rate performances of $LiCoO_2$ were greatly improved comparing with the pristine $LiCoO_2$.[16b]

Because of the toxicity and high price of cobalt, efforts have been made by using manganese and nickel to replace cobalt, forming $LiMnO_2$ and $LiNiO_2$ with isostructure of $LiCoO_2$. $LiNiO_2$ has a reversible capacity 200 mAh/g, higher than that of $LiCoO_2$. But, some of the Ni^{3+} ions are reduced to Ni^{2+} during the Synthesis, which will severely increase the irreversible capacity and decrease the diffusion rate of Li ions, due to the increased disorder of cation site.[18] The layered $LiMnO_2$ is not the most thermodynamically stable form and is a little distorted from the ideal structure.[19] Therefore, the phase transition to spinel $LiMn_2O_4$ during cycling leads to poor electrochemical performances.[20] All these problems of $LiMnO_2$ and $LiNiO_2$

promoted the studies of solid-solution approaches by either cathionic substitution with M (M=Ni, Mn, Co, etc.),[21] or anionic substitution with S, F, etc.[22] For example, $Li(Ni_{1-x}Co_x)O_2$ shows a higher reversible capacity than $LiNiO_2$;[21b] while $Li(Ni_{0.8}Co_{0.15}Al_{0.05})O_2$ has been successfully commercialized. [21a] Another widely investigated cathode material is the solid solution between Li_2MnO_3 (i.e. $LiLi_{1/3}Mn_{2/3}O_2$) and $LiMO_2$, both of which have similar layered structure.[23] This solid solution cathode shows a very high reversible capacity about 200~300 mAh/g. [24] Though Li_2MnO_3 is not active between 3~4 V vs. Li/Li^+, it can be activated upon charging at 4.5 V vs. Li/Li^+. This "activation" process, however, introduces a large irreversible capacity for the first cycle due to the leaching of Li_2O. Surface coatings have also reported to improve the performances of this promising electrode material. [25]

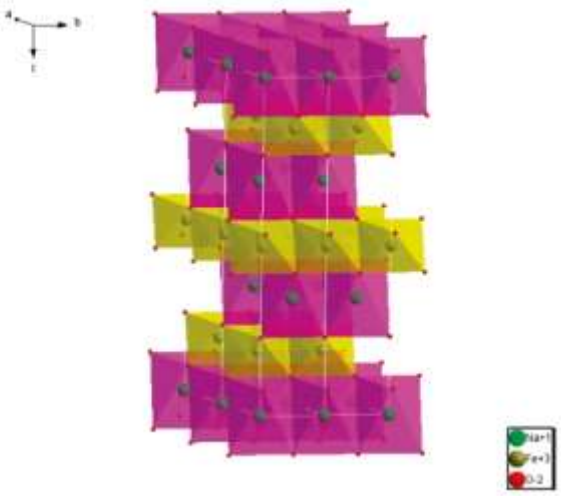

Figure 1.6 Crystal structure of layered α-$NaFeO_2$.[6] Adapted with permission from (Ellis, B. L.; Lee, K. T.; Nazar, L. F., Positive electrode materials for Li-ion and Li-batteries. *Chem. Mat.* 2010, 22 (3), 691-714). Copyright (2010) American Chemical Society.

Spinel. By taking advantages of the Mn^{4+}/Mn^{3+} redox couples, alternative materials spinel $LiMn_2O_4$[26] has been investigated extensively. Initially $LiMnO_2$, isostructural of $LiCoO_2$ was proposed to replace $LiCoO_2$, but the instability of the layered structure limits its application.

Instead, the structural stability of spinel $LiMn_2O_4$ has attracted extensive attention. $LiMn_2O_4$ has a crystalline structure of $Fd\bar{3}m$ space group, as shown in figure 1.7.[27] $LiMn_2O_4$ has advantages like abundant resources and non-toxicity. However, at an early stage, its rechargeable capacity is lower than that of $LiCoO_2$ and dramatic capacity fading occurs at elevated temperatures due to Mn dissolution[28], which impede the commercialization of this promsing cathode material. Fortunately, the performance of spinel $LiMn_2O_4$ has been found greatly improved by cationic substitution.[29] Due to its low price, safety and high power, $LiMn_2O_4$ is suitable for large-sized batteries. In 2004, it appeared in the market as the most popular electrode component in power sources for hybrid vehicles. In addition, it is also used as power source for electrical bicycles and motorcycles. [12]

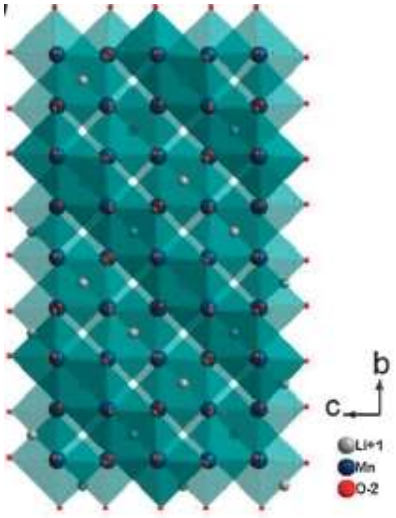

Figure 1.7 Crystal structure of spinel $LiMn_2O_4$.[27] Adapted from (Wang, H.; Dai, H., Strongly coupled inorganic-nano-carbon hybrid materials for energy storage. *Chem. Soc. Rev.* 2013, 42 (7), 3088-3113) with permission of The Royal Society of Chemistry.

Since the energy of a battery roughly equals to the product of its average voltage and capacity, batteries with higher energy density can be obtained by higher voltage. Several methods can be used to tailor the electrochemical potentials of materials. Studies revealed that

cationic substitutions of manganese ions in $LiMn_2O_4$ with cations such as Cr, Co, Ni, and Fe usually display two potential plateaus during discharge, i.e. one ~4 V and another ~5 V.[30] The 4 V plateau comes from the $Mn^{3+/4+}$ redox couple and the 5 V plateau is usually due to the substituted $M^{3+/4+}$ or $M^{2+/3+}$ redox couples. Among the cation-substituted systems, the high operating voltage ~4.7 V of spinel $LiMn_{1.5}Ni_{0.5}O_4$ with theoretical capacity of 147 mAh/g makes it an promising candidate for high-energy applications.[30d]

Olivine phosphate. The olivine structure has received extensive attention since the first demonstration of reversible lithium extraction and insertion in $LiFePO_4$ by Goodenough's group.[31] $LiFePO_4$ has an olivine structure and crystallizes in space group *Pnma*, as described in figure 1.8.[6] Oxygen forms a distorted hexagonal close-packed framework, with P occupying 1/8 of the tetrahedral sites, and Li and Fe occupying 1/2 of the octahedral sites. $LiFePO_4$ has very stable crystal structure, even the fully delithiated product $FePO_4$ maintains the original structure. It shows a delithiation voltage about 3.5 V vs. Li/Li^+, and a theoretical capacity of 170 mAh/g.

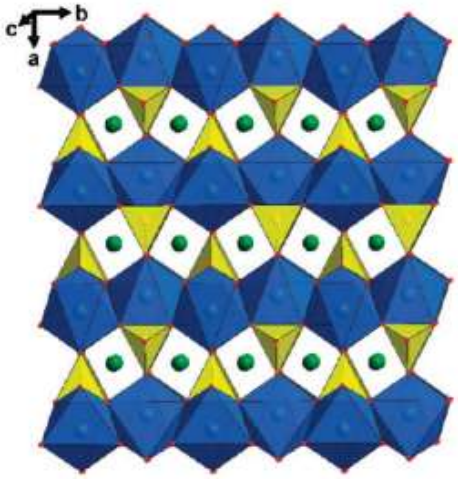

Figure 1.8 Crystal structures of $LiFePO_4$ (olivine structure).[6] Adapted with permission from (Ellis, B. L.; Lee, K. T.; Nazar, L. F., Positive electrode materials for Li-ion and Li-batteries. *Chem. Mat.* 2010, 22 (3), 691-714). Copyright (2010) American Chemical Society.

A major issue related to $LiFePO_4$ is its poor ionic and electronic conductivity. This limitation has been partially overcome by coating with conductive carbon on $LiFePO_4$ nanoparticles[32] and partially by doping approaches.[32a] The low price and high structural stability make $LiFePO_4$ also promising for large-scale applications and it has been used in industrial products by some corporations. Surface modification and cationic substitution have been applied to increase the electronic and ion conductivity of $LiFePO_4$. Dopants like Nb, Ti and Mg can improve the electrical conductivity of LiFePO4 [32a]. Amorphous carbon layer on the surface of $LiFePO_4$ provides transport paths for electrons. Continuous and uniform coating layer can be achieved by facile thermal decomposition of carbon source like sucrose. Hu et. al. reported a coating of both RuO_2 and carbon on $LiFePO_4$ which can further improve the rate capability. [33] Moreover, it's also important to have nanosized $LiFePO_4$, so that diffusion lengths for charges can be significantly reduced.[34] For example, comparing with thick plates, nanoplates of $LiFePO_4$ with a uniform coating of 5 nm thick amorphous carbon layer shows remarkable improvement in storage capacity (165 mAh/g close to the theoretical value of 170 mAh/g).[35]

Some isostructures of olivine $LiFePO_4$, such as $LiMnPO_4$, $LiCoPO_4$, and $LiNiPO_4$, have become attractive because of the high energy density promised by their high discharge potentials, i.e. 4.1, 4.8, 5.2 V vs. Li/Li^+, respectively.[36] However, other than the low conductivity for electrons and ions, another major issue with these high-voltage cathodes is the instability of the electrolyte. When the redox potential of cathode material is below the HOMO of the electrolyte, electrons in the HOMO of electrolyte will transfer to the cathode and the electrolyte will be oxidized, leading to the formation of SEI layer on the cathode/electrolyte interface. In order to improve these high-voltage cathode materials, it's important to develop novel electrolyte that can have higher band gap than current used organic solvent. The capacity and potential of common electrode materials in Li-ion batteries are shown in figure. 1.9.[5]

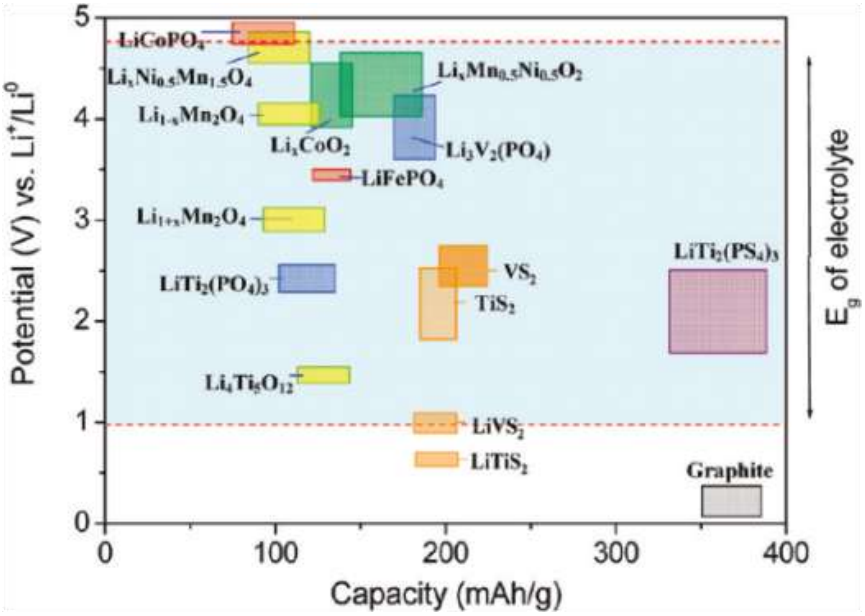

Figure 1.9 Potential versus capacity of several electrode materials relative to the electrochemical potential window of the electrolyte (1M $LiPF_6$ in EC/DEC).[5] Adapted with permission from (Goodenough, J. B.; Kim, Y., Challenges for rechargeable Li batteries. *Chem. Mat.* 2009, 22 (3), 587-603). Copyright (2009) American Chemical Society.

1.2.1.3 Anode materials

Lithium metal. Lithium metal was used as anode at the very early stage, owing to its high capacity (3860 mAh/g), but was later replaced by graphite because of the safety concern.

Graphite. Graphite has a layered structure and can act as a host of the intercalation and extraction of lithium ions. Every six carbon atoms of one hexahedron can hold one lithium ion (LiC_6), which leads to the theoretical capacity of 372 mAh/g. Because of the large space between the graphitic layers, exfoliation of graphite occurs upon cycling due to the intercalation of electrolyte molecules into the layered interstices. This was commonly found in propylene carbonate (PC) based electrolyte.[37] Additives like S_x^{2-} [38] and vinylene carbonate[39] were found to be able to prevent the exfoliation of graphite. Carbon nanotubes (CNT) and graphene have been investigated as anode materials as well. For CNT, capacity of 400 mAh/g and 500 mAh/g were reported for SWNTs[40] and MWNTs[41], respectively; For garphene, capacity much higher than

theoretical capacity was also reported by controlling the space between graphene layers, so called "pseudo-graphite". [42] [43] [44] However, both CNT and graphene show disadvantages of large irreversible capacity and rapid capacity fading.

Lithium alloying anode. Lithium alloying mainly refers to the reaction of lithium with several group IV elements: Si, Ge, and Sn. Silicon has been recently extensively investigated as anode material for Li-ion batteries, due to its promising high energy density. When fully lithiatied into $Li_{4.4}Si$, it produces a capacity of 4212 mAh/g, which is about an order higher than that of graphite. Meanwhile, its discharge profile, with a low potential (~370 mV) and a long plateau, is similar to graphite. The major challenge of Si is the rapid capacity fading resulted from the extremely large volume expansion upon complete lithiation (~300%). This large volume change during cycling will lead to the mechanical failure of the Si, creating fresh surface for more SEI layer and making Si particles inaccessible for charges diffusion and redox reactions. Exciting progresses have been made recently with many different approaches. First, various types of nanostructures, such as nanowires,[45] nanoparticles, nanotubes,[46] and mesoporous Si,[47] have shown both excellent capacity and cycling performances. The improvement is due to not only the increased surface area and shortened diffusion length, but also the increased mechanical strength of Si when the size falls into nanoscale. Second, different coating layers (metal, carbon, oxides) shows the capability to alleviated or confine the volume change of Si. Last, different binders have been tried to accommodate the large volume change and mechanical strained during the cycling of Si. Several literatures have achieved more than 1000 cycles of stable cycling, and preliminary commercialization has been reported. [46b, 48]The theoretical capacity of Ge and Sn is 1384 mAh/g and 933 mAh/g, respectively, both higher than that of graphite as well. However, same issue of fast capacity fading as Si is also the biggest challenge. 1000 cycles of

stable cycling have also been reported recently for anode of Ge nanowires[49] and graphene-supported Sn.[50]

Spinel $Li_4Ti_5O_{12}$. $Li_4Ti_5O_{12}$ is an anode material with several unique properties, especially very stable cycling performances. This is because the very low volume variation during lithiationo/delithiation (so called zero-strain insertion), and the unfavorable formation of SEI layer (its electrochemical potential is inside the band gap of the electrolyte). It has a discharge potential about 1.55 V vs. Li/Li^+ and a capacity about 175 mAh/g. However, this high potential in anode will considerably reduce the energy density of the full cell.

Oxides. Transition metal oxide is another type of widely investigated anode materials for Li-ion batteries. They have a conversion-type reaction with lithiu during discharge, forming metal and Li_2O particles upon the complete lithiation, as shown in table 1.1.[8] Typically, they can generate a capacity around 500~1000 mAh/g, much higher than that of graphite. Another advantage is that they can be easily synthesized into a variety of different nanostructures. However, the poor conductivity of transition metal oxides leads to the very poor rate capability. Another unfavorable property is their high discharge potentials, around ~1 V vs. Li/Li^+, which lowers down the voltage and energy density of the full cell. Meanwhile, the first cycle of metal oxides always shows a large irreversible capacity, and the cycling performances are not good. Recently, many literatures have reported improvements in the performances of metal oxides by either using different nanostructures or by utilizing the carbonaceous materials (CNT, graphene, etc.) as conductive supporting materials.[8]

1.2.1.4 Electrolyte

For a suitable electrolyte in Li-ion batteries, following requirements should be satisfied:[51]

(1) Excellent conductivity for Li ions but electrically insulating;

(2) Large band gap or electrochemical potential window so that higher voltage electrodes can be used;

(3) Excellent thermal stability within a wide range of temperatures;

(4) Chemically inert to any opponent in the battery cell;

(5) Non toxic and environmental friendly

To meet these criteria, lithium salt dissolved in organic solvent is currently used as electrolyte in commercial Li-ion batteries. Common used lithium salts include $LiPF_6$, $LiClO_4$, LiCl, $LiCF_3SO_3$, LiTFSI, etc. Cyclic esters (ethylene carbonate, etc.) and linear esters (dimethyl carbonate, Diethyl carbonate, etc.) are usually mixed as the solvent so as to achieve both high permittivity and low viscosity.

Though the organic electrolytes show excellent ionic conductivity near room temperature, they have many disadvantages as following: (1) safety concern due to the flammability of the solvent; (2) unable to be used at high temperature (>100 ^oC) and low temperature (<-20 ^oC); (3) causing complexity for battery design due to the leakage and evaporation of electrolyte; (4) difficulty for battery miniaturization. In order to overcome these problems, different types of solid phase electrolyte have been investigated. Figure 1.10 shows the thermal evolution of ionic conductivity of different types of electrolytes in lithium batteries.[52]

(a) Solid polymer electrolyte refers to the electrolyte that is formed by mixed lithium salts, such as $LiPF_6$, $LiCF_3SO_3$, with solvent-free solid polymers, such as PEO (poly (ethylene oxide)).[53] Adding inorganic nanoparticles, such as SiO_2, into the electrolyte can greatly improve the ionic conductivity.[54] Generally, this kind of all-solid electrolyte has low ionic conductivity at room temperature.

(b) Gel-type polymer electrolyte is formed by trapping the liquid organic electrolyte inside the solid polymer matrix. An example is 1 M $LiPF_6$ EC-PC inside PVDF-HFP.[55] This kind of

design combines the merits of high ionic conductivity of liquid electrolyte, and better mechanical property of the solid polymer electrolyte.

(c) Inorganic solid electrolyte contains a large group of Li-ion conductive materials, mainly including sulfides systems (Li_2S-P_2S_5, etc.) and oxides systems.[56] Typical oxide systems includes Li_3PO_4[57], NASICON-type phosphate ($LiTi_2(PO_4)_3$, etc.)[58] and pervoskite oxides ($Li_{3x}La_{2/3-x}TiO_3$[59], etc.).[56] Sulfides systems refer to the different mixtures of glassy, glassy-ceramic, and crystalline sulfides (Li_2S, GeS_2, SiS_2, P_2S_5, etc.). Glassy-ceramic $70Li_2S$-$30P_2S_5$, crystalline $Li_{3.25}Ge_{0.25}P_{0.75}S_4$ and crystalline $Li_{10}GeP_2S_{12}$ was reported to have ionic conductivity of 3.2×10^{-3}[60], 2.2×10^{-3}[61] and 1.2×10^{-2} S/cm[52] at room temperature, respectively. In general, ionic conductivity at the order of 10^{-3} S/cm can be achieved at room temperature for these inorganic solid electrolytes.

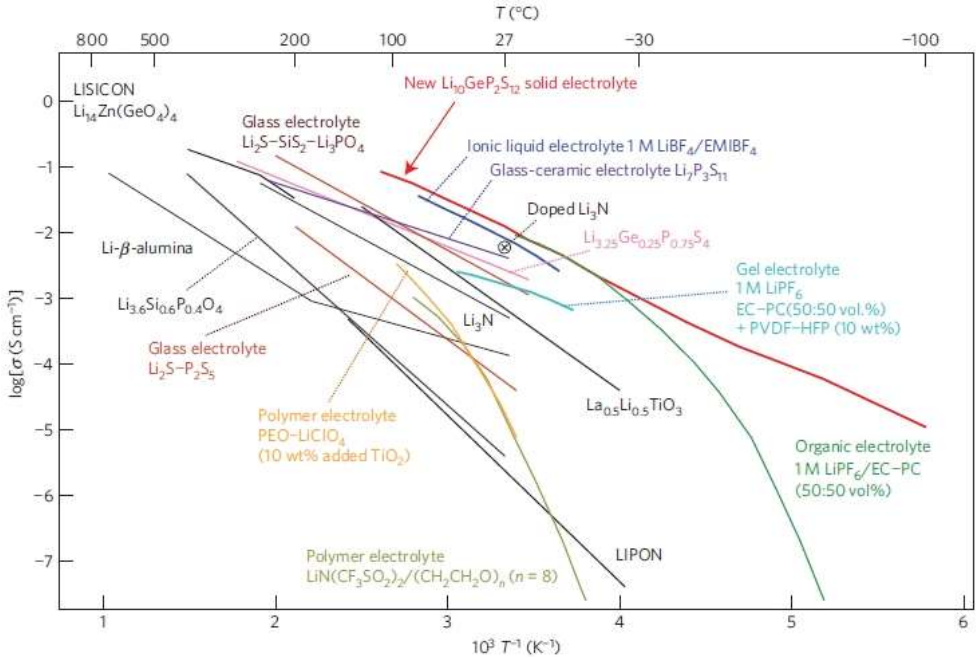

Figure 1.10 The thermal evolution of ionic conductivity of different types of electrolytes in lithium batteries. Adapted by permission from Macmillan Publishers Ltd: Nature Materials[52], copyright (2011).

1.2.2 High energy-density batteries beyond Li-ion batteries

High energy density storage systems are urgently demanded for (hybrid) electric vehicles (EVs, HEVs) and stationary energy storage for sustainable but unstable energy resources like wind and solar, which vary with seasons and geographical distributions. Though, Li-ion batteries have successfully powered mobile electronics for decades, the maximum energy the Li-ion batteries can store/deliver is still far below the requirements of mobile transportation and grid-scale stationary energy storage. For example, today's Nissan Leaf with Li-ion batteries can drive about 160 km per charge [1]; while the goal of EVs should be beyond 500 km. Therefore, the demand for exploration of new chemistry and new materials is urgent. Among various investigated candidates, Li-O_2 and Li-S batteries are two most promising solutions, owing to their much higher energy densities.

1.2.2.1 Li-O_2 battery

The design of Li-O_2 is a hybrid of battery with fuel cell. Li metal is utilized as anode, and the cathode is an open design same as in a fuel cell, so that O_2 gas can flow through the porous carbon and catalyst, where it will be reduced during discharge. As shown in figure 1.11, when non-aqueous electrolyte is used, the O_2 will be reduced into Li_2O_2 by Li ion during discharge; when aqueous electrolyte used, LiOH will be the product. For the design of aqueous electrolyte, a Li ion-conductive and Li metal-protecting membrane is a must to isolate the Li metal from the attack of water. The theoretical energy density of non-aqueous Li-O_2 battery can be as high as 3505 Wh/kg, nearly an order higher than 387 Wh/kg of today's $LiCoO_2$-C Li-ion battery.[62]

The first rechargeable non-aqueous Li-O_2 battery was reported by Abraham et. al., and has been extensively investigated recently due to its extremely promising energy density. Though many progresses have been reported, several major challenges have not been solved:

- Safety concern of Li metal anode: as mentioned above, the dendrite formation during

cycling and internal short-circuit is the reason that Li metal was excluded as anode materials in the history. But in order to achieve higher energy density, same challenge has to be addressed again by modifying the metal anode so as to suppressing the hazardous dendrite growth.

- To achieve a stable SEI layer on Li metal is another concern as the electrochemical potential of Li metal is lower than the LUMO of the current organic electrolyte.
- Suitable electrolyte is another big challenge. Other than excellent Li ion conductivity, it should have high solubility and diffusivity for O_2; it should be stable so as not to be oxidized by super oxide LiO_2, which is the intermediate product of cathode reaction.
- Cheap catalyst at cathode side is also crucial. With different catalysts, the charge-discharge voltage difference has been reported to be around 0.6 ~ 1.5 V, much smaller than bare porous carbon cathode. Other than precious metal, several studies have reported on using oxides as catalyst.
- The design of cathode should be porous with optimized pore size distribution and high surface are. Meanwhile, operation of the cell in the ambient air requires a membrane allowing the pass of O_2 but blocking the CO_2 and H_2O, which has been reported to form Li_2CO_3 and greatly reduce the reversibility of the cell.

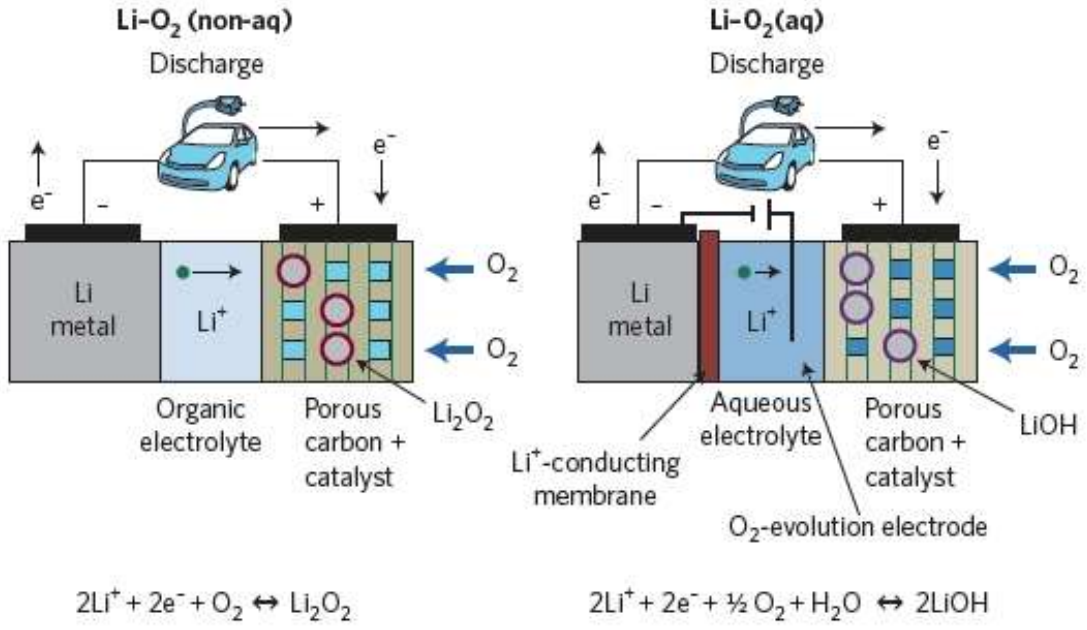

Figure 1.11 Schematic illustration of the operation of a non-aqueous (left) and aqueous (right) Li-O_2 battery. Adapted by permission from Macmillan Publishers Ltd: Nature Materials[62], copyright (2011).

1.2.2.2 Li-S battery

In a typical configuration of today's Li-S battery, lithium metal is the anode, and elemental S is the cathode. The major advantages of Li-S battery are: (1) much higher energy density than today's Li-ion batteries, as shown in table 1.2.[63] Lithium metal can store more Li-ions than commercialized graphite in Li-ion batteries; S has an overall redox reaction $S_8 + 16Li^+ + 16e^- \leftrightarrow 8Li_2S$, which gives a theoretical capacity of 1672 mAh/g.[10] The theoretical energy density can be as high as 2567 Wh/kg.[10, 63] (2) The cost of sulfur is low due to the abundant resource, and sulfur is non-toxic.

Table 1.2 Comparison between Li-S batteries and today's commercialized Li-ion batteries.[63]

	Theoretical specific capacity (mAh/g)	Cell voltage (V)	Theoretical specific energy (Wh/kg)	Theoretical energy density (Wh/l)
Li-S	1672	2.2	2, 567	2,199
$LiCoO_2$-C	~140	3.8	387	1,015

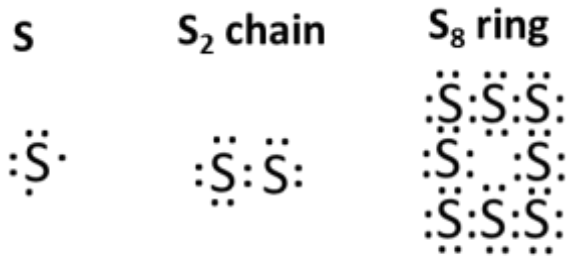

Figure 1.12 Lewis electron diagrams of sulfur

Li-S battery has a relatively complicated electrochemistry with many polysulfides involved as intermediates. For elemental sulfur molecule, two S atoms can make a "coordinate covalent" single bond, rather than the double bond in O_2. Sulfur can naturally form poly-sulfur with two, four, six or eight atoms, among which eight atoms with a ring structure S_8 is the most favorable, as shown in figure 1.12. Sulfur is easy to get electrons and become polysulfide ions. During discharge of Li-S battery in organic electrolyte, the reduction of S_8 into Li_2S typically has three steps with lithium polysulfides as intermediates, as shown in figure 1.13.[6, 10, 64] S_8 is first reduced into soluble Li_2S_4, and the oxidation state changes from S^0 to $S^{0.5-}$. Then, $S^{0.5-}$ is reduced into S^-, and insoluble Li_2S_2 is formed, which is slower due to the nucleation of solid phase. The third step with the conversions of solid Li_2S_2 into solid Li_2S is the most difficult, because of the diffusion of Li ions inside the solid bulk. As for oxidation process (i.e. charge), there is typically

one anodic current peak found in cyclic voltammetry, indicating fast oxidation of one polysulfide, which is believed to be S_8^{2-}.[65] Other polysulfides transformed into it by a non-charge transfer step with facile kinetics, which precedes the anodic current peak.[65]

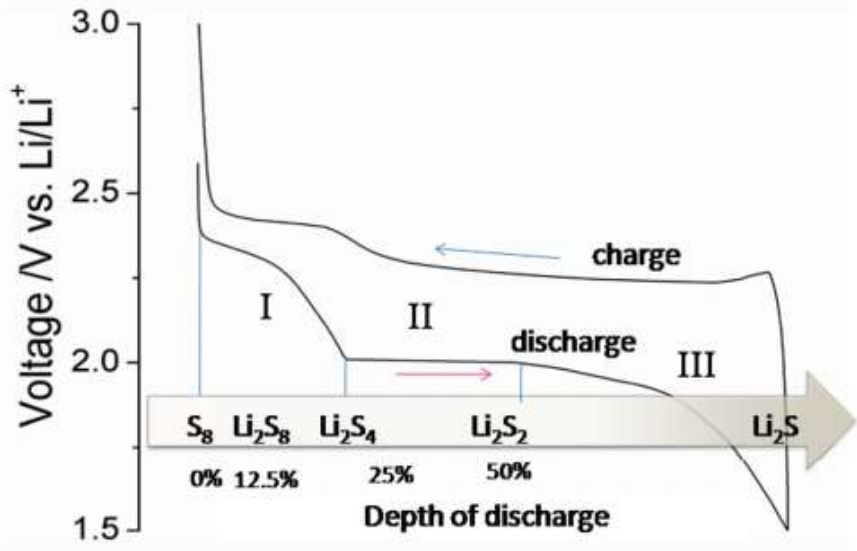

Figure 1.13 Discharge/charge profile of a Li-S battery.[6] Adapted with permission from (Ellis, B. L.; Lee, K. T.; Nazar, L. F., Positive electrode materials for Li-ion and Li-batteries. *Chem. Mat.* 2010, 22 (3), 691-714). Copyright (2010) American Chemical Society.

Li-S battery actually has a long history since late 1960s.[66] Despite the exciting advantages mentioned above, there are many big challenges, which are still not well solved even after decades of investigation. First, both elemental S and the reduced Li_2S after discharge are electrically insulating. Conductive additive with good electrical contact is a must in the electrode. The second, the most serious problem hindering its commercialization, is the fast capacity fading caused by the dissolution of intermediate polysulfides (Li_2S_n) in the organic electrolyte[67], which further results in a polysulfide shuttle phenomenon, as illustrated in figure 1.14. The soluble polysulfides S_n^{2-} are produced at the cathode side either by reduction of S_8 when discharging or by oxidation of Li_2S and Li_2S_2 when charging, as discussed above. Once the concentration

gradient built up, they can diffuse in the electrolyte, pass through the separator and arrive at the surface of the anode Li metal, where they are reduced by Li metal into solid Li_2S_2 or Li_2S.[64a] The solid products fully cover the surface of Li metal, and reduce newly arrived polysulfides into lower order S_{n-x}^{2-}, which will transfer back to the cathode side when concentrated. At the surface of cathode, those polysulfides will be reduced into solid Li_2S or Li_2S_2 upon the full discharge, some of which is delocalized, aggregated and becomes inaccessible to electrochemical reactions.[68] This shuttle phenomenon repeats with the charge/discharge cycling of the cell, reducing the active mass in the cathode, increasing the impedance of the cell, deteriorating the kinetics of the cell, and therefore leading to low columbic efficiency and fast capacity fading. A mathematical modeling for this shuttle phenomenon is presented by Mikhaylik et al. [69]

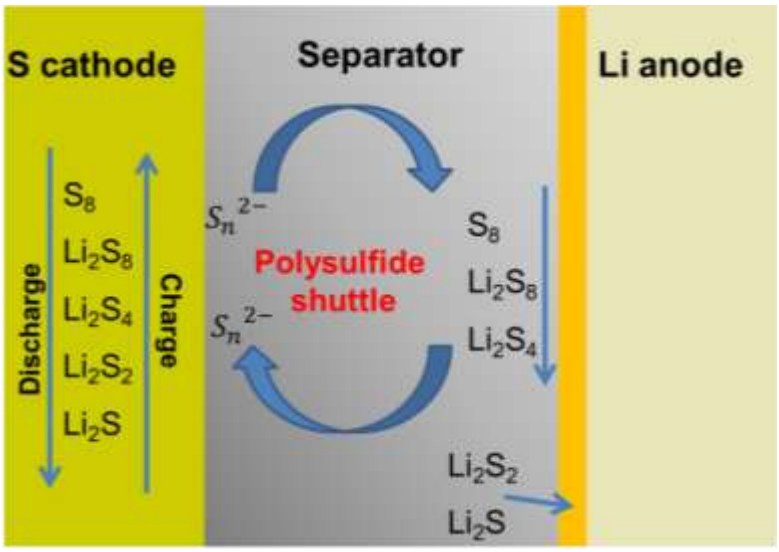

Figure 1.14 Polysulfide shuttle phenomenon in Li-S cell

Several different strategies have been studied to overcome these problems. To improve the conductivity, carbonaceous nanomaterials (CNTs[70], graphene[71], carbon fiber[72], conductive polymer[73], etc.) have been utilized in the electrode. As for the polyfulfides shuttle, many different approaches are under investigation:

(1) Porous structures with large surface area have been utilized as a reservoir for polysulfides so as to alleviate the polysulfides shuttle.[74] For example, Nazar et. al[75] found that sulfur impregnated in ordered mesoporous carbon (CMK3) can deliver discharge capacity more than 1000 mAh/g based on the weight of sulfur. Cui et. al designed york-lock core-shell structure of PANi-S [76] and TiO_2-S [77] structures, which can be cycled for up to 1000 cycles.

(2) Many surfactant have been found being able to fix the polysulfides on the electrode so as to suppress the polysulfides dissolution. Improvements by adding PVP [78], CTAB [79], PEG [80] in cathode have been reported.

(3) Different additives (P_2S_5,[81] $LiNO_3$,[82] etc.) in organic electrolyte have been studied to suppress the polysulfides shuttle. $LiNO_3$ has been found to be an effective additive to improve the cycling stability and columbic efficiency. Recently, highly concentrated electrolyte, like 5~7 M lithium salt in organic solvent, has been reported to be able to greatly improve the cycling performance and columbic efficiency, though the rate capability was deteriorated due to the decreased ion conductivity of the electrolyte.[83]

(4) Solid state electrolyte was investigated to avoid the polysulfids dissolution, so that polysulfides shuttle can be completely prevented. Several different types of solid state electrolyte have been tried, such as Li_2S-P_2S_5,[84] and LISICON.[85] Liang et al[86] reported a new electrolyte with relatively high ion conductivity up to 1.6×10^{-4} S/cm at room temperature, which shows both excellent capacity and cyclability when cycled at 60 ^{o}C.

(5) Sealing the sulfur surface to prevent the polysuflides dissolution. Many different materials have been tried to coat on the sulfur surface, such as oxides[77], conductive polymer[87], graphene[88], graphene oxide[89]. But, complete sealing is hard to achieve and polysulfides shuttle was only slightly allieviated by these reports. Thick and uniform graphene oxide coating was recently reported to be able to achieve an excellent cycling performance for 1000 cycles.[89] The

only research that is close to a complete sealing has been reported in recent.[90] Amorphous carbon-sulfur core-shell nanowires were synthesized by a post-impregnation treatment of melting sulfur into carbon nanotubes obtained from AAO template. The openings of the CNT were sealed with sputtered platinum. The potential plateau ~2.3 V did not appear during the cycling, which indicated the avoiding of dissolution of high-order polysulfides.

(6) Recently, several approaches trying to avoid the high-order polysulfides seem to be facile and promising to overcome the polysulfides shuttle.[91] Since the high-order polysufides (Li_2S_8, Li_2S_6, or Li_2S_4) have high solubility and low-order polysulfides (Li_2S_2 and Li_2S) are insoluble in organic electrolyte, different methods have been tried to avoid the high-order polysulfides. Wan et al[91] synthesized carbon fiber with sub-nanometer pores which can trap the small molecules of low-order polysulfides so that the formation of high-order polysulfides can be prohibited. Manthrium et.al[92] proposed a cycling method that does not completely covert the Li_2S into high order polysulfides during charge, utilizing only the potential plateau at ~2.1 V vs. Li/Li^+.

To sum up, great progresses have been made in Li-S batteries. For the state-of-art performances, capacity retention over 1000 cycles ranging from 40%~80% can be achieved.[76, 79, 88-89] However, further research is still required before it can be commercialized, especially for the following issues: (1) achieving better stability of cycling performances; (2) improving the S loading weight ratio in the electrode (currently ~50%); (3) rate capability improvement (currently less than 5 C); (4) safety concern of the Li metal dendrite formation; (5) scale-up feasibility and cost control.

1.3 Objectives

Motivated by the increasing demand in today's market for lithium batteries with high energy density and high power density, this dissertation will focus on the study of electrode materials that are promising to outrival the state-of-art commercial Li-ion batteries in perspective of energy density, cyclability, and safety.

In Chapter III, traditional Li intercalation mechanism-based electrode material $LiCoO_2$ will be first studied, since only half of its theoretical capacity is utilized in current Li-ion batteries. By overcoming the overcharge issue, the energy density is possible to be doubled. The approach adopted in this dissertation is applying a layer of Li-ion conductive surface coating on $LiCoO_2$ nanoparticles. Two aspects of this approach will be studied: (1) the understanding of the interaction between the Li ion-containing surface coating and the $LiCoO_2$ core; (2) the effect of the Li-ion conductive surface modification on the electrochemical performances, especially the overcharge performances, of the $LiCoO_2$.

The second focus of this dissertation is the Li-S battery, which is promising to store/deliver energy several times higher than that of current Li-ion batteries. Studies will be conducted to address the three major issues of the Li-S batteries: poor conductivity of sulfur, polysulfides shuttle, and safety hazard. In Chapter IV, a pre-lithiated mesoporous Si electrode will be used to couple the S cathode, so as to eliminate the safety hazard caused by the dendrite growth on Li metal anode. Meanwhile, ordered mesoporous carbon CMK-8 will be used as host for elemental S to improve the conductivity and to suppress the polysulfides shuttle. The electrochemical performances of the S electrode and Si electrode in both half cell and full cell will be investigated respectively. The safety advantage of the pre-lithiated Si/S full cell will be demonstrated and the mechanism of the dendrite formation in Li-S battery will be discussed.

In Chapter V, a novel liquid-type polysulfids catholyte will be investigated as the active material in Li-S batteries. Flexible carbon nanotubes (CNT) sponge and carbon nanofiber (CNF) sponge will be employed as the reservoir of the catholyte. Studies will be conducted to optimize the catholyte loading, catholyte concentration, and the sponge properties, so that excellent performances (capacity, cyclability, etc.) can be achieved. Meanwhile, the performances of this catholyte/sponge electrode in a pre-lithiated Si/S full cell will be further studied.

CHAPTER II

GENERAL EXPERIMENTAL

2.1 Materials Synthesis

Li foil (99.9%), sulfur (99.5%), $LiPF_6$ (99.5%), and $LiNO_3$ (anhydrous, 99.999%) were obtained from Alfa Aesar for all the study. LiTSFI (99.95%) was from Sigma Aldrich. Anhydrous electrolyte solvent DOL, DME, EC, DMC, DEC were all from Alfa Aesar.

For the Synthesis of $LiCoO_2$, a hydrothermal method was utilized with LiOH, H_2O_2 and $Co(OH)_2$ as starting materials. For the Synthesis of S composite, elemental sulfur was melted at high temperature in Ar atmosphere and impregnated into carbon structures. Detailed Synthesis processes will be described in Chapter III, IV and V.

2.2 Structure characterization

2.2.1 X-ray diffraction (XRD)

X-Ray diffraction (XRD) was used to determine the crystal structure of the synthesized materials. According to Bragg's law

$$2d\sin\theta = n\lambda \tag{2.1}$$

where d is the spacing of lattice planes, n is an integer, θ and λ is the incident angle and wavelength of the X-ray, respectively. In this dissertation, XRD measurements were performed with a Bruker instrument (Bruker-AXS D8 VARIO) with Cu Kα radiation. The patterns were measured from 2θ = 15 to 75 degree with a step size of 0.01 °and dwell time of 0.1 s.

2.2.2 Microscopy

The morphologies of the materials studied in this dissertation were characterized with scanning electron microscopy (SEM) and transmission electron microscopy (TEM). SEM was conducted by a JEOL JSM-7500F; TEM was conducted with either JEOL-2010 or FEI Tecnai

G2 F20 FE-TEM. Energy dispersive spectroscopy (EDS) was conducted by the spectrometer integrated in the above instruments to have elemental analysis of the electrode materials.

Scanning Transmission Electron Microscopy (STEM) was conducted with FEI Tecnai G2 F29 FE-TEM. In STEM, the narrowly focused electron beam will scan over the sample, allowing an observation of images with clear *z*-contrast; whereas traditional TEM can only obtain a planar view with phase contrast. Meanwhile, with STEM, EDS mapping can be easily performed to correlate the atomic-resolution distribution of elements with the image.

2.3 Electrochemistry

2.3.1 Electrode and cell preparation

In order to prepare working electrodes, active material, conductive additive (usually acetylene black), and polymer binder (usually PVDF polyvinylidene fluoride) were first mixed in N-methyl-2-pyrrolidinone (NMP). The mixture was coated on an Al foil by rolling method, which was then dried in vacuum to completely remove the solvent.

To assemble a coin cell, a Li foil was used as counter electrode other than specifically mentioned. For a three-electrode system, Li foil was used as both the reference and counter electrode. A Celgard 2400 membrane (Celgard, Inc) was used as separator. For the electrolyte, 1-M $LiPF_6$ dissolved in a mixture of ethylene carbonate (EC), diethyl carbonate (DEC), and dimethyl carbonate (DMC) (EC:DEC:DMC=1:1:1 by volume) was used for research on $LiCoO_2$; 1 M LiTFSI + 1 wt.% $LiNO_3$ in dioxolane and dimethoxyethane (DOL:DME= 1:1 by volume) was used for research on sulfur batteries. Cells were assembled in an Ar-filled glovebox with moisture and oxygen concentrations below 0.1 ppm.

2.3.2 Cyclic voltammetry

Cyclic voltammetry (CV) is a widely used technique for characterizing electrochemical performance of batteries. Three-electrode system was used with Li as both reference and counter electrode. The potential applied between the working electrode and reference electrode was scanned and cycled in a potential window linearly at a constant rate. By measuring the current between the working electrode and counter electrode, the electrochemical reactions according to the current peaks can be identified at specific potentials. Potentiostat CHI 604D will be used to conduct this measurement.

2.3.3 Galvanostatic charge/discharge

Galvanostatic charge/discharge refers to supplying/drawing constant current to/from a battery cell. A battery can be charged by either applying a current or a voltage. For the convenience of systematic study, charge/discharge with constant current is widely used in academic research. Since constant current is used, the total amount of charges delivered by a battery cell is given by

$$Q = It \tag{2.2}$$

where t is the time for which the current I flows. Q is called the capacity in battery research, and has a unit of Columb (C) or Ah. Specific capacity Q_s, including volumetric capacity (Ah/kg) or gravimetric capacity (Ah/L), is one of the most important properties to characterize a battery cell. They can be derived by

$$Q_s = Q/m \text{ or } Q_s = Q/V \tag{2.3}$$

where m and V is the weight and volume of the cell, respectively. The energy of a cell can be written as

$$E = \int UIdt \tag{2.4}$$

where U is the voltage of the battery. Since a battery cell operates around the operational voltage U_o during most of its operation time, the energy can be estimated by

$$E \approx U_o It = U_o Q \tag{2.5}$$

The power of a battery cell can be expressed as

$$P = E / t \approx U_o I \tag{2.6}$$

In order to describe the high-speed energy-delivering capability, or rate capability, of a battery cell, a parameter called C rate is adopted, which is given by

$$C = \frac{I}{Q} \tag{2.7}$$

This parameter describes how fast a battery can deliver/store the energy. For example, 1 C rate means a cell achieves capacity Q in one hour with a current of I. Columbic efficiency $q_{columbic}$ refers to the reversibility of the battery cell in terms of capacity. It can be given by dividing the discharge capacity with charge capacity. Battery cells can achieve very high Columbic efficiency up to 1, but, due to the hysteresis of the electrochemical potential, the energy efficiency q_{energy} will be smaller.

$$q_{energy} = \frac{E_d}{E_c} = \frac{U_d Q_d}{U_c Q_c} = \frac{U_d}{U_c} q_{columbic} \tag{2.8}$$

where subscript c and d refers to charge and discharge, respectively.

2.3.4 Electrochemical impedance spectroscopy (EIS)

The EIS refers to impedance spectroscopy with small potential perturbation at various frequencies at a given potential (AC signal with 5~10 mV amplitude). A potentiostat coupled with Frequency Response Analyzer is required to conduct the experiment. Either three-electrode or two-electrode system can be used for the measurement. For the former one, the single electrode impedance spectroscopy is obtained; for the latter, a full cell impedance spectroscopy

is produced. Nyquist plot, imaginary impedance vs. real impedance, is commonly used to characterize the battery cell, which usually consists of a low frequency semi-circle and a high-frequency tail. An equivalent electric circuit in battery electrode and corresponding impedance spectrum are shown in figure 2.1.[93] Ohmic resistance (R_Ω) refers to the resistance of the electrolyte and the separator, which can be obtained by the intercept resistance on real axis. Double layer capacitance (C_d) refers to the impedance arising from the double layer capacitor at the electrolyte/electrode interface, which is non faradaic. The semicircle diameter is the charge transfer resistance (R_{ct}), which indicates the kinetics of the charge transfer process from the ionic species in solution to the solid electrode at the electrode/solution interface.

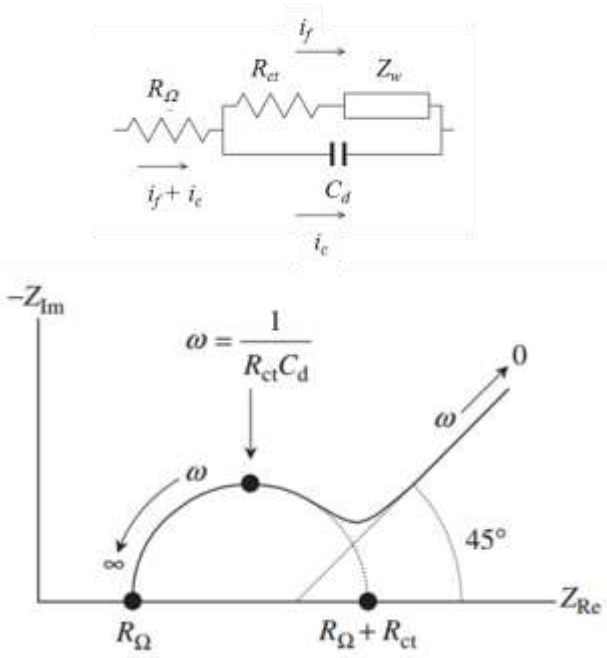

Figure 2.1 Typical equivalent electric circuit and Nyquist plot of EIS of an electrode in battery cell. w is the AC frequency, R_{ct} is the charge transfer resistance, R_Ω is the ohmic solution resistance, C_d is the double layer capacitance at the solution/electrode interface.[93] Reprinted from *Handbook of Electrochemistry*, 1st ed., Zoski, C., Classical experiments, p432, Copyright (2007), with permission from Elsevier.

CHAPTER III

FUNCTIONAL SURFACE MODIFICATION OF NANO-$LiCOO_2$ FOR THE IMPROVEMENT IN OVERCHARGE PERFORMANCES*

3.1 Introduction

The recent high demands for high-energy and high-power Li-ion batteries (LIB) have been driven by a variety of mobile systems such as portable electronics and electronic vehicles (EVs). $LiCoO_2$ has been most popular as a cathode (positive) material for commercial LIB because of its high capacity and good cycling stability. When the cathode is made of nanostructured $LiCoO_2$ rather than conventional micron-scale $LiCoO_2$, more energy can be stored and high-rate charge/discharge can be achieved. This is because the surface area becomes very large for higher reactions and shorter diffusion length of Li ions and electrons with nanostructured $LiCoO_2$. Jo et al. [94] and Kawamura et al. [95] reported that rate capability and cyclability have been improved with nano-scale $LiCoO_2$ with optimum particle sizes of ~300 and ~60 nm, respectively. Okubo et al. [96] controlled $LiCoO_2$ particle sizes from 9 to 32 nm with $Co(OH)_2$ and LiOH by using a hydrothermal method. Particles smaller than 17 nm have not only reduced the capacity but also deteriorated the rate capability. Therefore, it would be crucial to get particles with appropriate sizes in order to improve electrochemical performance.

Despite the high theoretical capacity of $LiCoO_2$ (274 mAh/g), only half (~140 mAh/g) of its theoretical capacity is utilized in practice due to its structural instability and capacity fading when charged over 4.2 V versus Li/Li^+ [97]. The liquid electrolyte may react with $LiCoO_2$ and thus dissolve Co^{4+}, resulting in a rapid fading in capacity [98]. Mechanical fracture or microcracks,

* Reprinted with permissions from (a) "Functional Surface Modifications on Nanostructured $LiCoO_2$ with Lithium Vanadates" by X. Pu, L. Yin, and C. Yu, *Journal of Nanoparticle Research* 2012, *14* (4), 1-7. Copyright (2012) by Springer Science and Business Media; (b) "Enhanced Overcharge Performance of Nano-$LiCoO_2$ by Novel Li_3VO_4 Surface Coatings" by X. Pu and C. Yu, *Nanoscale* 2012**,** *4* (21), 6743-6747. Copyright (2012) by The Royal Society of Chemistry.

which lead to a fast decrease of the cycling capacity, may occur when the battery is overcharged. In order to overcome these problems, research has been focused on achieving an appropriate coating on $LiCoO_2$. Metal oxides (Al_2O_3, ZrO_2, MgO, SnO_2, CeO_2, etc. [99]) and metal phosphates ($AlPO_4$, $FePO_4$, etc. [100]) are two kinds of mostly investigated coating materials. These coatings provide a physical barrier so as to prevent the detrimental reaction between $LiCoO_2$ and the electrolyte, which would alleviate the structural damage within $LiCoO_2$ particles and improve capacity retention during cycling [101]. However, such coatings also introduce inactive weights as well as suppress reactions associated with lithium extraction and insertion during charge/discharge. In particular, when $LiCoO_2$ nanoparticles are used, it is necessary to use a large amount of inactive materials due to the large surface-to-volume ratio of the nanoparticles. Hence, attempts were also tried to use active coating materials such as $LiFePO_4$ [102] and $Li_4Ti_5O_{12}$ [103] so that the capacity reduction can be minimized. Recently, surface modifications by Li_3PO_4 on $LiCoO_2$ [104], $LiFePO_4$ [105], $LiNi_{0.5}Mn_{1.5}O_4$ [106] and $Li(Ni_{0.4}Co_{0.3}Mn_{0.3})O_2$ [107] have improved both cyclability and rate capability. Li_3PO_4 is one of the fast Li-ion conductors and also provides a physical barrier layer to suppress the detrimental reaction.

Lithium vanadate (Li_3VO_4) has a similar crystal structure as Li_3PO_4 as well as has been identified as a Li ion conductor [108]. Its theoretical capacity (~400 mAh/g) is the highest among all cathode materials by far (transitional metal-containing cathode materials, not comparing with sulfur and O_2). It is electrochemically active between 2 to 3.8 V, which is lower but close to the potential window of $LiCoO_2$ (3.5 to 4.2 V). Hence, lithium vanadate can be an excellent functional surface modifier for nanosized $LiCoO_2$ to suppress the detrimental reaction between $LiCoO_2$ and electrolyte as well as achieve high charge/discharge rates.

In this chapter, we report lithium vanadate coatings on nanosized $LiCoO_2$ particles. The $LiCoO_2$ nanoparticles were synthesized by using a hydrothermal method, and then the particles

were wet-coated and subsequently sintered with different amounts of NH_4VO_3 and LiOH. Firstly, we conducted the investigation on how the structure and morphology of the coating layers and core active materials change when the surface of the active material is modified with different reaction conditions. In particular, the coating process may consume Li from $LiCoO_2$ when coatings such as $FePO_4$ [100c], V_2O_5 [109], TiO_2 [110] are used. Here, we systematically identified the change of the coating and active materials depending on the reaction conditions, when lithium vanadate was used for surface modification on nanostructured $LiCoO_2$.

Secondly, we studied the effect of the surface coating lithium vanadate (Li_3VO_4) on the electrochemical performances of the nanostructured $LiCoO_2$, especially the overcharge performances. Excellent cyclability was achieved even overcharged to 4.5 V and 4.7 V vs Li/Li^+, when the surface coating was optimized. Comparing with the bare nanostructured $LiCoO_2$, surface coating also significantly improved the high-rate capability. The mechanism for the overcharge capacity fading was also discussed. While the increased reaction with nanostructured $LiCoO_2$ is responsible for a higher power density, compared to micron-size commercial $LiCoO_2$, the detrimental reactions are also increased, prohibiting their use for commercial applications. Here, the novel lithium vanadate coatings on nanoscale $LiCoO_2$ particles improved both overcharge cyclability and high-rate capability by suppressing the side reactions.

3.2 Experimental

3.2.1 Synthesis of $LiCoO_2$ nanoparticles

A hydrothermal method was utilized to synthesize nanostructured $LiCoO_2$ nanoparticles. First, 0.18 g of $Co(OH)_2$ was mixed in 20 ml of a 5M-LiOH aqueous solution, and then the mixture was sonicated for 20 min at 50 ^oC with a dropwise addition of H_2O_2. The mixture was transferred to a Teflon-lined stainless steel autoclave and kept at 180 ^oC for 12 h. Subsequently,

the resulting precipitates were collected by centrifugation and washed with deionized water, and then dried at 100 ^{o}C in a vacuum oven for 12 h.

3.2.2 Surface coating of Li_3VO_4

NH_4VO_3 was used to obtain lithium vanadate coatings on the prepared $LiCoO_2$ nanoparticles. We first investigated the reaction between $LiCoO_2$ and NH_4VO_3. As described in table 3.1, six different molar ratios for the prepared $LiCoO_2$, NH_4VO_3 and LiOH were tested. They were mixed in 20 ml deionized water and kept at ~90 ^{o}C for 6 h with magnetic stirring. After the solution was completely dried, powders were collected and calcinated in air for 3 h at three different temperatures, 300, 400, and 700 ^{o}C. The calcination temperatures for different samples are described in table 3.1.

After we understood the reaction between $LiCoO_2$ and NH_4VO_3, we varied the $LiCoO_2$ concentration with a constant molar ratio of NH_4VO_3 to LiOH (= 1:3), as listed in table 3.2. Different ratios of $LiCoO_2$ and NH_4VO_3 are likely to alter the thickness and morphology of the coating. The molar ratio of NH_4VO_3 to LiOH is to ensure that enough Li ions are available to maintain $LiCoO_2$ structures during the sintering process, as described below. For these reactions, $LiCoO_2$, NH_4VO_3, and $LiOH{\bullet}H_2O$ were mixed in 20 ml deionized water and kept at ~90 ^{o}C for 6 h with stirring. Subsequently, the completely dried powder was calcinated at 400 ^{o}C for 3 h in air. Assuming all NH_4VO_3 and LiOH were transformed into Li_3VO_4, the weight percentages of Li_3VO_4 out of the total weight of Li_3VO_4-coated $LiCoO_2$ were calculated to be 3.4 wt.%, 5.5 wt.%, 22.2 wt.%, and 53.1 wt.%, as listed in table 3.2.

Table 3.1 Molar ratios between $LiCoO_2$, NH_4VO_3, and LiOH, and corresponding calcination temperatures for synthesizing the coating layers on the $LiCoO_2$ nanoparticles.

Synthesis condition	Molar ratio $LiCoO_2 : NH_4VO_3 : LiOH$	Calcination temperature (^oC)
A	1 : 1 : 0	300
B	1 : 1 : 0	400
C	1 : 1 : 0	700
D	1: 1/3 : 0	400
E	1 : 1 : 1	400
F	1 : 1 : 3	400

Table 3.2 The weights and molar ratios of the chemicals for the sintering process to obtain different weight percentages of the Li_3VO_4 coatings on the $LiCoO_2$ nanoparticles. The molar ratio of Li to V was 3:1. The weight percentages of Li_3VO_4 were calculated by dividing the weight of Li_3VO_4 with that of Li_3VO_4-coated $LiCoO_2$, assuming all NH_4VO_3 and LiOH were transformed into Li_3VO_4.

$LiCoO_2$ (g)	NH_4VO_3 (g)	$LiOH•H_2O$ (g)	Molar ratio $LiCoO_2 : NH_4VO_3 : LiOH$	Calculated weight percentages of Li_3VO_4 (wt.%)
0.2	0.195	0.2120	1.2 : 1 : 3	53.1
0.2	0.049	0.0530	4.9 : 1 : 3	22.2
0.2	0.010	0.0110	23.9 : 1 : 3	5.5
0.2	0.006	0.0065	39.8 : 1 : 3	3.4

Table 3.3 The weights of $LiCoO_2$, NH_4VO_3, $LiOH•H_2O$ and their molar ratios for synthesizing Li_3VO_4 coating layers on $LiCoO_2$ nanoparticles.

$LiCoO_2$ (g)	NH_4VO_3 (g)	$LiOH•H_2O$ (g)	Molar ratio $LiCoO_2 : NH_4VO_3 : LiOH$	Calculated weight percentages of Li_3VO_4 (wt.%)
0.20	0.049	0.0530	4.9 : 1 : 3	22
0.20	0.010	0.0110	24 : 1 : 3	5.5
0.20	0.006	0.0065	40 : 1 : 3	3.4

In order to study the electrochemical performances, slightly different conditions were used. Still a molar ratio of LiOH : NH_4VO_3 = 3:1 was used for the Li3VO4 coating. The calcinating temperature used was increased to 700 ^oC for 3 h in air for the coating of Li_3VO_4, so as to achieve better crystallinity. The calculated weight percentages of Li_3VO_4 coating were 3.4, 5.5, and 22 %, respectively. Additionally, as-synthesized $LiCoO_2$ nanoparticles were also calcinated at 700 ^oC for 3 h in air for comparison. Table 3.3 shows details of the materials used for the Synthesis.

3.2.3 Structure chracterization

X-ray diffraction (XRD) measurements were performed with a Bruker instrument (Bruker-AXS D8 VARIO) with Cu Kα radiation. The patterns were measured from 2θ = 15 to 75 degree with a step size of 0.01 ° and dwell time of 0.1 s. The samples were inspected with a field-emission scanning electron microscope (SEM: JEOL JSM-7500F) and a transmission electron microscope (TEM: JEOL JEM-2010). Energy-dispersive spectroscopy (EDS) mapping was conducted in a scanning TEM (FEI Tecnai G2 F20).

3.2.4 Electrochemical measurements

In order to prepare working electrodes, 70-wt.% active material, 20-wt.% acetylene black, and 10-wt.% polyvinylidene fluoride were mixed in N-methyl-2-pyrrolidinone. The mixture was coated on an Al foil, which was then dried in vacuum at 100 ^{o}C for 10-12 h to completely remove the solvent. A Li foil and a Celgard 2400 membrane were used as a counter electrode and a separator, respectively. For the electrolyte, 1-M $LiPF_6$ dissolved in a mixture of ethylene carbonate (EC), diethyl carbonate (DEC), and dimethyl carbonate (DMC) (EC:DEC:DMC=1:1:1 by volume) was used. CR2032 coin-type cells were assembled in an Ar-filled glovebox with moisture and oxygen concentrations below 0.1 ppm. Charge/discharge tests were performed with an Arbin BT-2000 battery tester between a voltage window of 3~4.5 V at 15~1200 mA/g current density. A three electrode setup was used to perform cyclic voltammetry and electrochemical impedance spectroscopy with a CHI 604D workstation using a Li foil as a counter/reference electrode. Cyclic voltammetry was conducted between 3~4.5 V with a scanning rate of 0.5 mV/s. Electrochemical impedance spectroscopy was carried out at a charged state (4.5 V) from 100 kHz to 0.01 Hz, with 5-mV amplitude.

3.3 Results and discussions

3.3.1 Synthesis of $LiCoO_2$ nanoparticles

The hydrothermal reaction can readily control the size of $LiCoO_2$ nanoparticles by changing reaction temperature, concentration, and reaction time. In order to synthesize the $LiCoO_2$ nanoparticles, first CoOOH was formed from the following reaction between $Co(OH)_2$ and H_2O_2 by ultrasonication.

$$2Co(OH)_2 + H_2O_2 \rightarrow 2CoOOH + 2H_2O \quad (3.1)$$

CoOOH was formed in only 20 min, as confirmed in the XRD pattern (Figure 3.1a, the lower plot). A subsequent hydrothermal reaction with LiOH yielded $LiCoO_2$ as a result of the following reaction, as shown in the XRD pattern (Figure 3.1a, the upper plot).

$$CoOOH + LiOH \rightarrow LiCoO_2 + H_2O \quad (3.2)$$

The $LiCoO_2$ nanoparticles were found to be in irregular shapes with ~50 nm in length (Figure 3.1b).

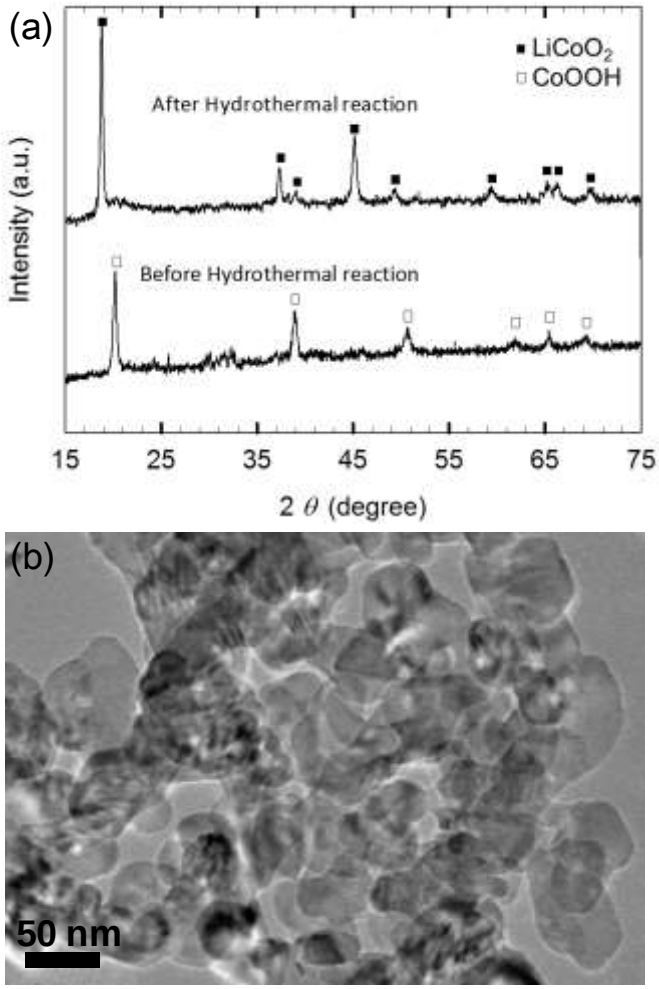

Figure 3.1 (a) XRD patterns that indicate the presence of CoOOH and $LiCoO_2$ before and after hydrothermal reaction, respectively. (b) A TEM image of the $LiCoO_2$ nanoparticles synthesized by the hydrothermal reaction.

3.3.2 Optimization of Li_3VO_4 surface modification

In order to have coatings on the prepared $LiCoO_2$ nanoparticles, a series of different reactions with $LiCoO_2$ nanoparticles and NH_4VO_3 (conditions in table 3.1) were designed to investigate the reactions between them during the Synthesis processes. Generally, NH_4VO_3 decomposes into V_2O_5 and NH_3 at temperatures above ~200 ^oC. In our experiments, when NH_4VO_3 was calcinated with $LiCoO_2$, we found that the vanadium oxide attracts lithium from $LiCoO_2$, resulting in $LiVO_3$, Li_3VO_4, and/or $LiCoVO_4$. When the molar ratio of $LiCoO_2$ to NH_4VO_3 was 1:1 and the calcination temperature was 300 ^oC (Condition A in table 3.1), Co_3O_4 and $LiVO_3$ were formed, as shown in figure 3.2a, as a result of the following suggested reaction.

$$12LiCoO_2 + 12NH_4VO_3 \rightarrow 12LiVO_3 + 4Co_3O_4 + 6H_2O + 12NH_3\uparrow + O_2\uparrow \quad (3.3)$$

With calcination at an elevated temperature at 400 ^oC (Condition B), $LiCoVO_4$ also appeared in addition to $LiVO_3$ and Co_3O_4 (Figure 3.2b). In case that the temperature was raised to 700 ^oC (Condition C), the product was only $LiCoVO_4$ with the same calcination time (3 hours), as shown in figure 3.2c. We believe this is due to increased diffusion between the elements at the higher temperature via the following suggested reaction:

$$4LiCoO_2 + 4NH_4VO_3 \rightarrow 4LiCoVO_4 + 2H_2O + 4NH_3\uparrow + O_2\uparrow \quad (3.4)$$

When molar ratio of $LiCoO_2$ to NH_4VO_3 was 1:1/3 (Condition D) for 400 ^oC calcination, $LiCoO_2$ was converted into Co_3O_4 and Li_3VO_4 (Figure 3.2d) and $LiVO_3$ was not observed. This implies that all Li in the $LiCoO_2$ nanoparticles was captured by NH_4VO_3 to form Li_3VO_4. The following reaction is suggested.

$$12LiCoO_2 + 4NH_4VO_3 \rightarrow 4Li_3VO_4 + 4Co_3O_4 + 2H_2O + 4NH_3\uparrow + O_2\uparrow \quad (3.5)$$

From the above experimental results, $LiCoO_2$ is likely to keep donating Li until Li_3VO_4 and/or $LiVO_3$ are formed. Hence, in order to maintain the structure of $LiCoO_2$, an extra Li source

(LiOH) was introduced for the calcination. According to the XRD pattern in figure 3.2e (Condition E), when the molar ratio of LiOH to NH_4VO_3 is 1:1 (the molar ratio of total Li to V is 2:1), $LiCoO_2$ was still converted into Co_3O_4 with both $LiVO_3$ and Li_3VO_4. With three times more LiOH (Condition F), only Li_3VO_4 was obtained without deteriorating the structure of $LiCoO_2$, as shown in figure 3.2f. This Synthesis condition supplied enough Li at a proper sintering temperature so as to produce only Li_3VO_4, as a result of the following suggested reaction.

$$3LiOH + NH_4VO_3 \rightarrow Li_3VO_4 + 4H_2O + NH_3\uparrow \quad (3.6)$$

With the gained understanding regarding the reaction between NH_4VO_3 and $LiCoO_2$, $LiCoO_2$ nanoparticles were further processed to have different weight percentages of Li_3VO_4 coatings. The molar ratio of extra Li (LiOH) to V was 3:1 so that a proper amount of Li can be provided to maintain the structure of $LiCoO_2$ nanoparticles as well as obtain only Li_3VO_4. According to the XRD pattern in figure 3.3, the structure of $LiCoO_2$ was not altered for all samples. For the samples with 53.1 wt.% and 22.2 wt.% Li_3VO_4 (see table 3.2), both Li_3VO_4 and $LiCoO_2$ peaks are clearly shown in figure 3.3a and figure 3.3b. The intensity of Li_3VO_4 peaks for the sample with 22.2 wt.% is smaller than those of the sample with 53.1 wt.% Li_3VO_4 due to the less quantity. When smaller amounts of NH_4VO_3 were used (5.5 and 3.4 wt.%, see table 3.2), clear diffraction peaks corresponding to Li_3VO_4 were not observed (Figure 3.3c and d), presumably due to the small amounts of Li_3VO_4. Nevertheless, it is very likely that the samples also contain Li_3VO_4 since Li_3VO_4 is the most favorable product with a sufficient supply of Li, as previously confirmed in this study.

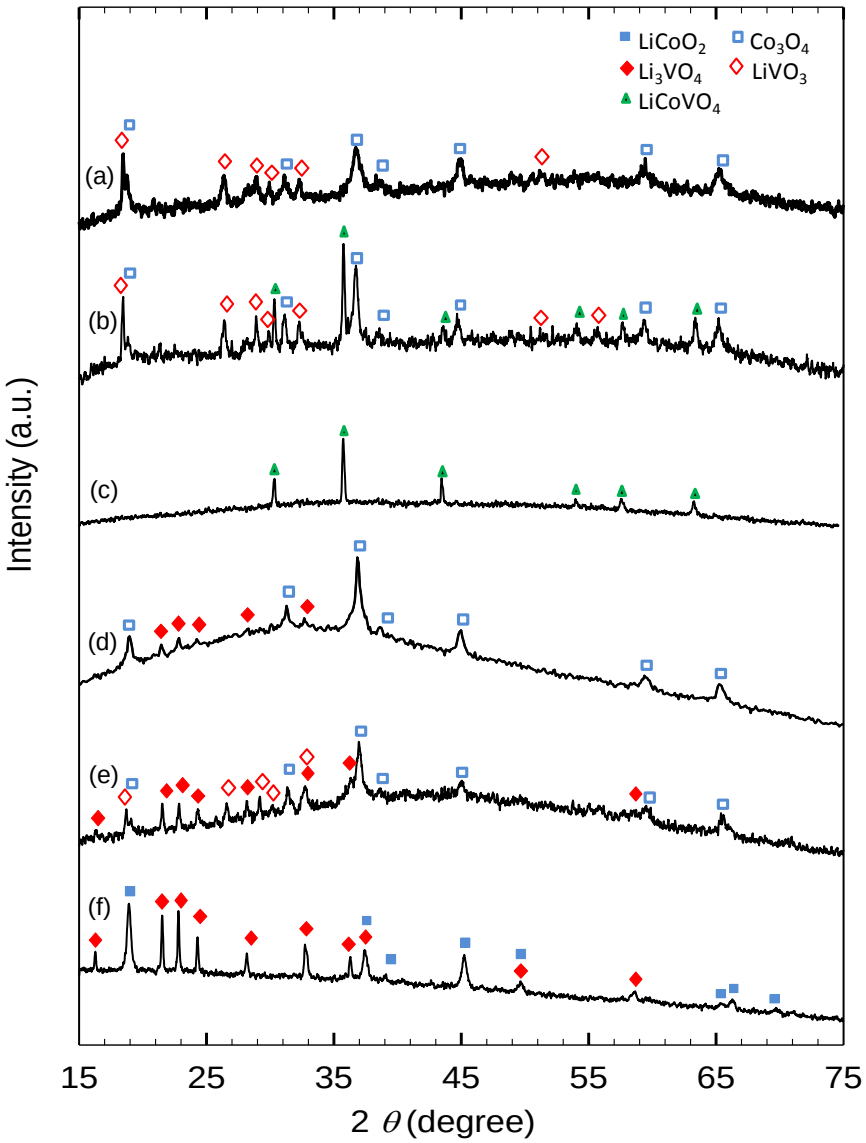

Figure 3.2 XRD patterns of the products after sintering the $LiCoO_2$ nanoparticles with NH_4VO_3 and LiOH. The molar ratios of NH_4VO_3 and LiOH as well as calcination temperatures are listed in table 3.1. (a) Synthesis condition A in table 3.1, (b) condition B, (c) condition C, (d) condition D, (e) condition E, and (f) condition F.

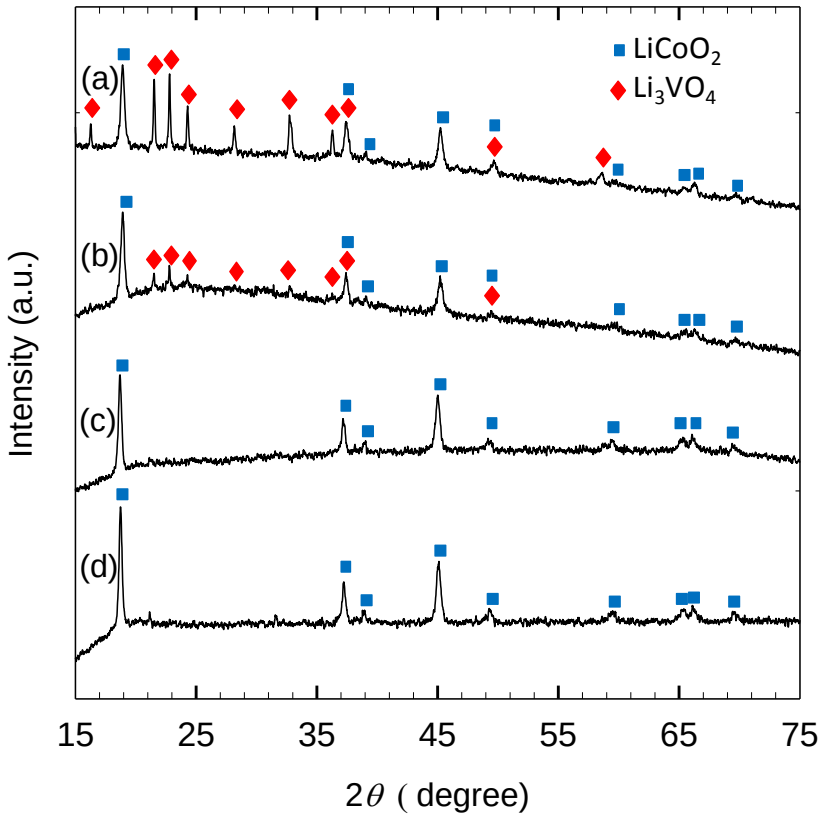

Figure 3.3 XRD patterns of pristine $LiCoO_2$ nanoparticles and $LiCoO_2$ coated with different weight percentages of Li_3VO_4: (a) 53.1 wt.%, (b) 22.2 wt.%, (c) 5.5 wt.%, and (d) 3.4 wt.%.

Figure 3.4a and b are TEM images of 22.2 wt.% of the Li_3VO_4-coated $LiCoO_2$ nanoparticles. According to the image in figure 3.4a, the size and morphology of the nanoparticles are similar after calcination at 400 ^oC for the Li_3VO_4 coatings. The high resolution image (Figure 3.4b) shows distinct lattice patterns between the inner $LiCoO_2$ particles and the outer surface Li_3VO_4 coatings. A part of the nanoparticles are aggregated with coating layers, as shown in figure 3.4c and d (aggregated particles after the sintering for the 5.5 wt.% coating). The enlarged image in figure 3.4d indicates the presence of the layer. The inset depicts energy dispersive spectra, confirming the presence of both Co and V elements in the sample. Note that the Cu peaks are from the TEM grid made of Cu.

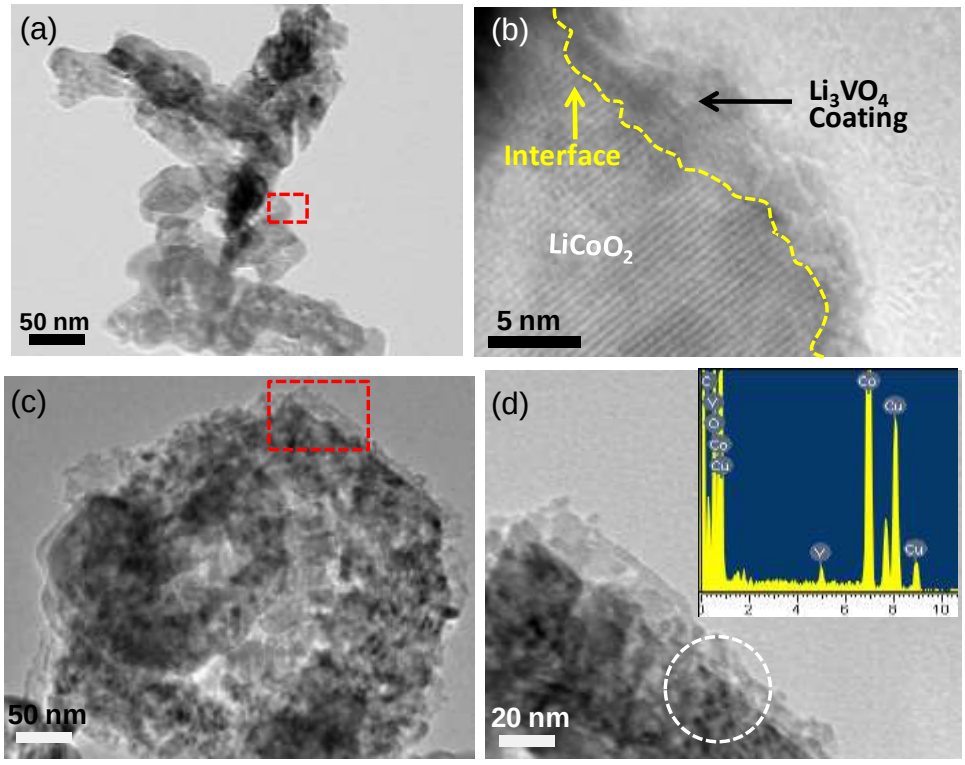

Figure 3.4 (a) A TEM image of $LiCoO_2$ nanoparticles coated with 22.2-wt.% Li_3VO_4. (b) A high resolution image for the rectangular portion in (a), indicating different lattice patterns for the core and the outer shell. (c) A TEM image of aggregated $LiCoO_2$ nanoparticles coated with 5.5-wt.% Li_3VO_4. (d) A higher magnification images for the rectangular portion in (c), showing the presence of the coating layer. The inset shows energy dispersive spectra for the circular portion in (d), indicating the present of both Co and V.

3.3.3 Effect of the surface modification on the overcharge performances

Figure 3.5 shows the XRD patterns of $LiCoO_2$ nanoparticles with and without coatings after calcination at 700 ^oC for 3 h. The diffraction patterns of bare $LiCoO_2$ nanoparticles clearly reveal the formation of a α-$NaFeO_2$-type layered structure with a $R\bar{3}m$ space group. According to our previous work,[111] the coating source (NH_4VO_3) captures Li ion from $LiCoO_2$ upon a high-temperature treatment. In order to maintain the structure of $LiCoO_2$, we added extra LiOH for the coating process. Li_3VO_4 peaks from the sample with 22-wt.% coating were identified. The inset

is an enlarged XRD pattern between 20° and 30° from the 22-wt.% coated sample, which clearly shows crystalline Li_3VO_4. On the other hand, we were not able to detect peaks corresponding to Li_3VO_4 in 3.4-wt.% and 5.5-wt.% samples. This is because Li_3VO_4 is amorphous or too small to be detected by XRD. We believe there are crystalline Li_3VO_4 coating layers for the 3.4-wt.% and 5.5-wt.% samples since the Synthesis condition except the quantity of the coating source was the same.

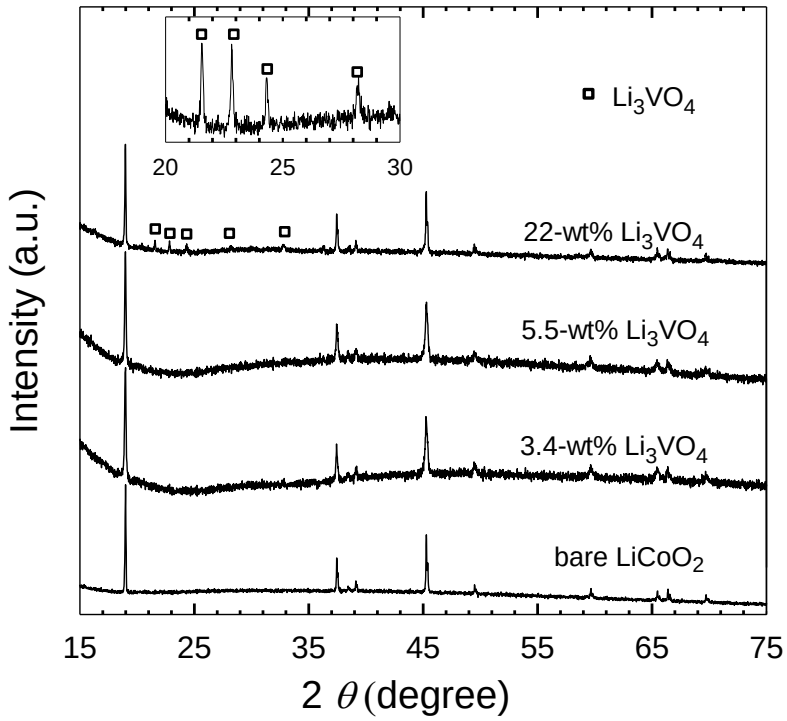

Figure 3.5 XRD patterns of 22-, 5.5-, 3.4-wt.% Li_3VO_4-coated and bare $LiCoO_2$ nanoparticles after calcination at 700 °C for 3 h in air. The inset is an enlarged plot for 22-wt.% Li_3VO_4-coated $LiCoO_2$ nanoparticles at $2\theta = 20\sim30^o$.

The morphologies of bare and Li_3VO_4-coated $LiCoO_2$ particles are shown in figure 3.6. The size of bare $LiCoO_2$ particles is ~200 nm after a 700-°C sintering process in air for 3 h. This particle size range and the high-temperature crystallization allows for a high rate capability and excellent capacity.[112] The size of the coated nanoparticles (3.4 and 5.5 wt.%) shown in figure

3.6b and c was not noticeably changed, compared to bare nanoparticles. Figure 3.6d is a TEM image of a $LiCoO_2$ nanoparticle coated with 5.5-wt.% Li_3VO_4. The corresponding EDS mapping images of cobalt and vanadium are shown in figure 3.6e and f, respectively. Vanadium was shown to be coated on the surface of the particle although the coating thickness is not uniform.

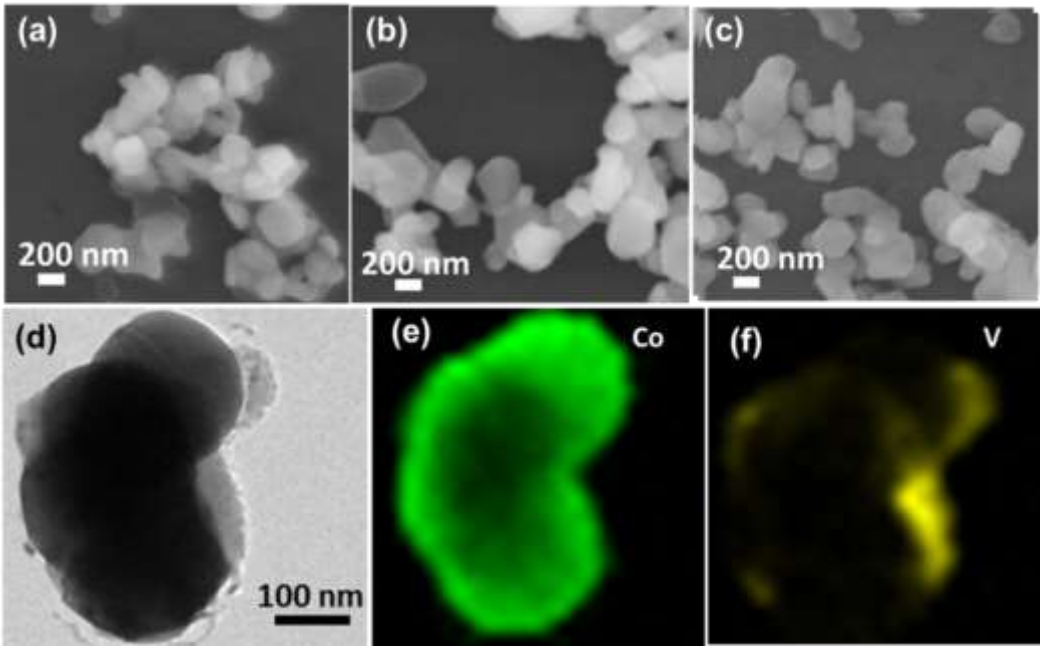

Figure 3.6 SEM images of bare $LiCoO_2$ (a), 3.4-wt.% (b), and 5.5-wt.% (c) Li_3VO_4-coated $LiCoO_2$ nanoparticles. A TEM image (d) of a 5.5-wt.% Li_3VO_4-coated $LiCoO_2$ nanoparticle with EDS mapping of Co (e) and V (f).

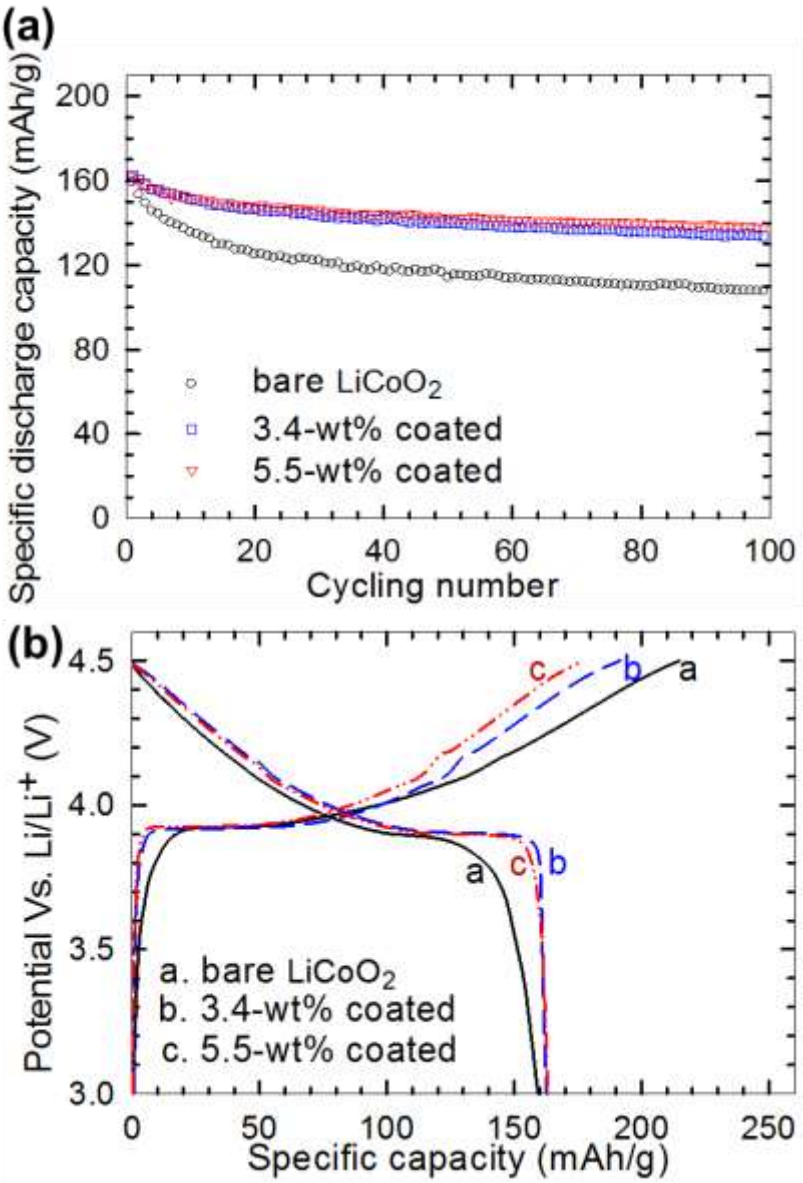

Figure 3.7 Gavalnostatic charge/discharge cycling performance (a) and the first charge/discharge potential profiles (b) of the electrodes containing the 3.4/5.5-wt.% Li3VO4–coated and bare $LiCoO_2$ nanoparticles with cycling voltages of 3 and 4.5 V at a current of 30 mA/g (~0.2 C). The test temperature was 20 ^{o}C.

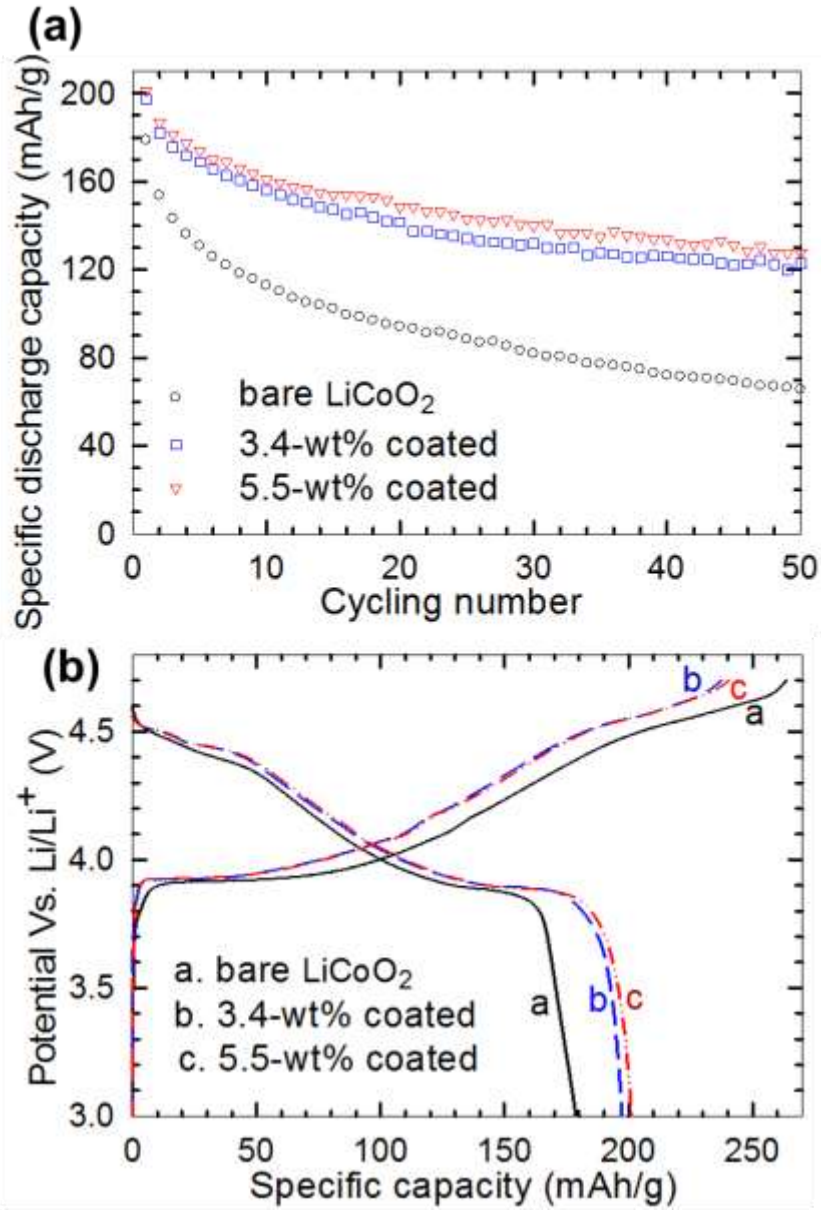

Figure 3.8 Gavalnostatic charge/discharge cycling performance (a) and the first charge/discharge potential profiles (b) of the electrodes containing the 3.4/5.5-wt.% Li_3VO_4–coated and bare $LiCoO_2$ nanoparticles with cycling voltages of 3 and 4.7 V at a current of 30 mA/g (~0.2 C). The test temperature was 20 ^oC.

When the coin cells were overcharged between 3~4.5 V at 30 mA/g current density (~0.2 C), the first specific discharge capacities of the cells with bare $LiCoO_2$ and 3.4/5.5-wt.% Li_3VO_4-coated $LiCoO_2$ were similar, ~160 mAh/g, as shown in figure 3.7a and b. After several cycles,

the bare $LiCoO_2$ had a large irreversible capacity whereas small irreversible capacity was observed from the coated samples. After 100 charge/discharge cycles at 30 mA/g, the capacity retentions of 3.4- and 5.5-wt.% Li_3VO_4 coated samples are ~83 and ~85 %, respectively, much larger than ~67 % of the bare $LiCoO_2$, as shown in figure 3.7a. This suggests that Li_3VO_4 is an effective and protective coating for $LiCoO_2$ nanoparticles.

With a higher overcharge cycling between 3~4.7 V at 30 mA/g, the initial capacity of 3.4-/5.5-wt.% coated samples were ~200 mAh/g, larger than 180 mAh/g of the bare $LiCoO_2$ sample, as shown in figure 3.8a and b. The capacity of the bare sample decreased significantly (~70 mAh/g) after 50 cycles whereas the coated samples maintained ~120 mAh/g, as shown in figure 3.8a. Without protective Li_3VO_4 coating layers, active materials are often consumed by the oxidation of electrolyte, being dissolved into the electrolyte or formed into inactive sites at solid-electrolyte interface layers. This effect is expected to be even larger when the cutoff charge voltage is higher. For instance, Yang et al.[113] reported that the capacity with bare $LiCoO_2$ nanoparticles rapidly dropped to 94 mAh/g after 20 cycles with cycling between 3~4.7 V. Our samples show high capacity retentions, 142 mAh/g and 152 mAh/g respectively with 3.4- and 5.5-wt.% Li_3VO_4 coating after 20 cycles (see Figure 3.8a).

The columbic efficiencies with the 4.5-V overcharge during the first cycle of the samples with 3.4- and 5.5-wt.% Li_3VO_4 coating were measured to be 85 % and 91 %, respectively, much higher than of 74% from the sample with bare $LiCoO_2$ (Figure 3.7b). With 4.7-V overcharge, the columbic efficiencies were 68%, 83%, and 84% for the samples with bare $LiCoO_2$, and 3.4- and 5.5-wt.% Li_3VO_4 coatings, respectively (Figure 3.8b). The higher columbic efficiency with the coatings indicates smaller irreversible capacity, presumably due to less loss of $LiCoO_2$ by the Li_3VO_4 coating.

Figure 3.9 shows the rate capability of the bare $LiCoO_2$ and 3.4-/5.5-wt.% Li_3VO_4-coated samples. The cycling was performed between 3 and 4.5 V at various current densities, ranging from 15 mA/g (~0.1 C) to 1200 mA/g (~8 C). The coated samples show better rate performance than that of bare nano-$LiCoO_2$. The 5.5-wt.% coated sample showed the best high-rate capability (Figure 3.9a), indicating fast transport of Li ions through the Li_3VO_4 coating layers, since the 5.5-wt.% coating is expected to be thicker than that of the 3.4-wt.% coating. Figure 3.9b summarizes the influence of different current density (or C rate) on discharge capacity. For the 5.5-wt.% sample, 115 mAh/g was maintained at a current of 1200 mA/g (~8 C), which is twice larger than that of the bare sample (64 mAh/g).

The Nyquist plots in figure 3.10 show the electrochemical impedance spectroscopy results of the electrodes with the bare and 5.5-wt.% Li_3VO_4-coated samples between 100 KHz~0.01 Hz at their charged state (4.5 V) after 1 and 30 cycles. The smallest Z' intercept of the first semicircle at high frequency range on the real axis is the resistance of electrolyte.[114] The high-frequency semicircle indicates the resistance of Li-ion migration through a solid-electrolyte interface (SEI) layer; the intermediate-frequency semicircle is attributed to the charge transfer resistance at the interface between a SEI layer and Li_xCoO_2; the low-frequency sloping line depicts the impedance of Li-ion diffusion inside Li_xCoO_2 solid particles.[115] After the 1st cycle, the impedance spectrum of the electrode bare $LiCoO_2$ sample is similar to that of the 5.5-wt.% Li_3VO_4-coated sample. After 30th cycle, a slight change occurred in the resistance of electrolyte for both electrodes. However, Z' of the high-frequency semicircle of the electrode with the bare $LiCoO_2$ nanoparticles was increased from 18 to 47 ohm, while Z' of the electrode with 5.5-wt.% Li_3VO_4-coated $LiCoO_2$ had an only slight change (from 14 to 20 ohm), indicating a stable and thinner SEI layer (see also TEM images in Figure 3.11b and d). Compared to the electrode with the bare $LiCoO_2$, the electrode with the coated $LiCoO_2$ also showed a smaller intermediate-

frequency semicircle. This small semicircle is likely to be from less structural damages in the coated $LiCoO_2$, compared to the bare nanoparticles after cycling.

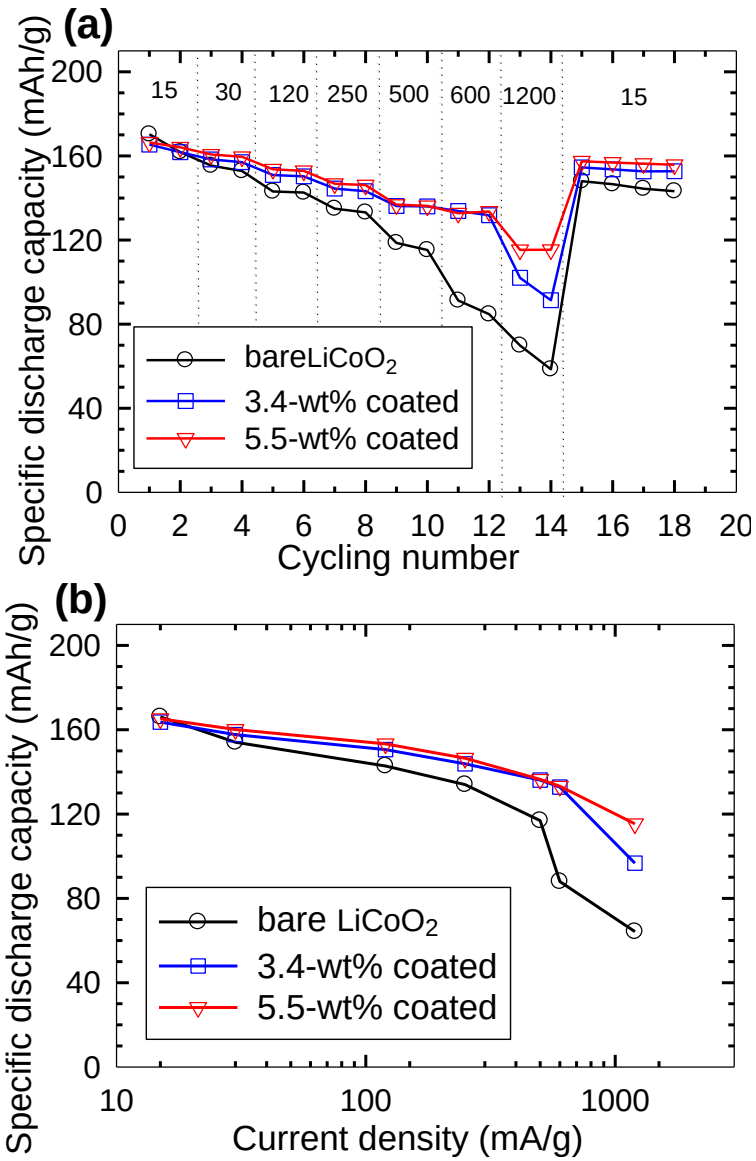

Figure 3.9 (a) The discharge capacity of the electrodes containing the 3.4/5.5-wt.% Li_3VO_4–coated and bare $LiCoO_2$ nanoparticles after cycling between 3.3 and 4.5 V at different rates (15~1200 mA/g: approximately 0.1~8 C). The current densities (mA/g) are indicated at the top. (b) The discharge capacity is plotted against the current density for the electrodes containing the coated and bare $LiCoO_2$. Two cycling measurements in (a) were averaged for this plot. The test temperature was 20 ^oC.

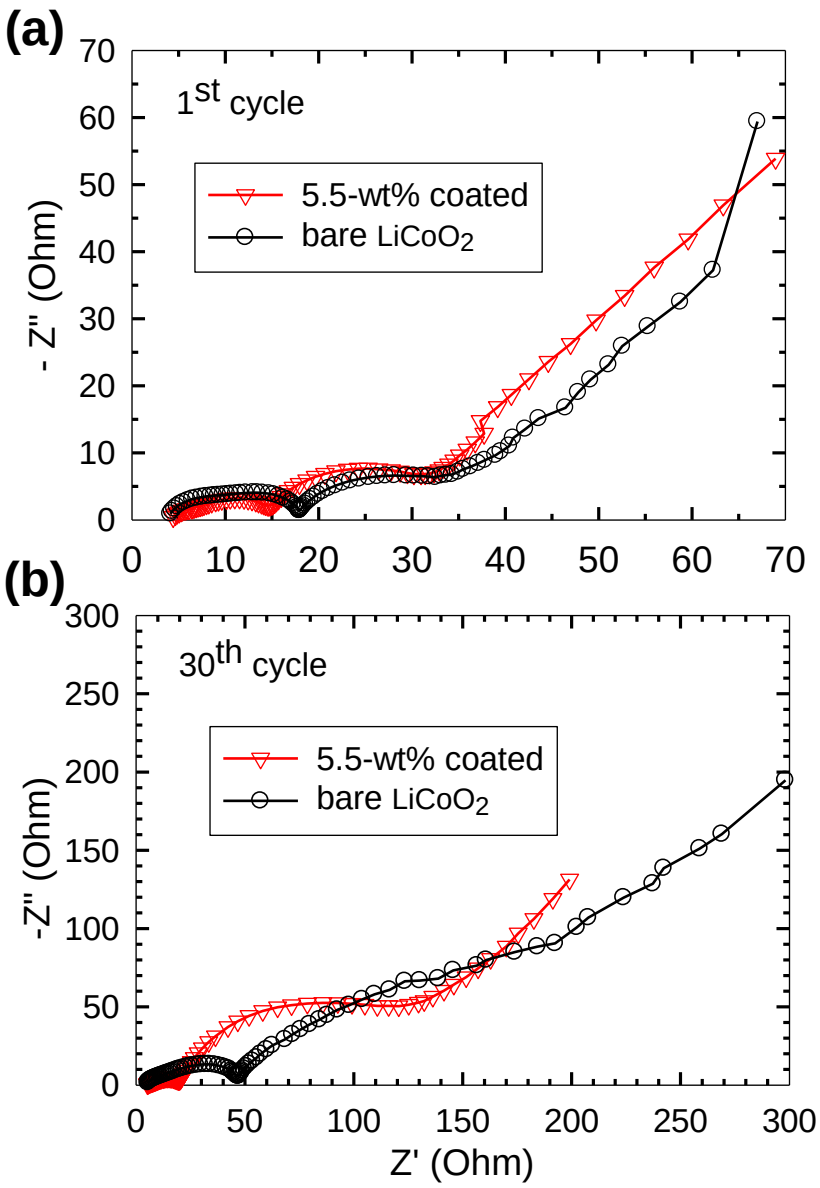

Figure 3.10 Electrochemical impedance spectra of the electrodes containing the 5.5-wt.% Li_3VO_4–coated and bare $LiCoO_2$ nanoparticles at a charged state (4.5 V) after the 1st cycle (a) and 30th cycle (b).

Figure 3.11 shows the TEM images of bare $LiCoO_2$ nanoparticles (a and b) and 5.5-wt.% Li_3VO_4-coated $LiCoO_2$ (c and d) after 50 cycles of charging/discharging to 4.7 V. A thick solid-electrolyte interface (SEI) layer (>20 nm) was formed on the bare $LiCoO_2$ nanoparticles, as

shown in figure 3.11b. On the contrary, the SEI layer of the coated $LiCoO_2$ (Figure 3.11d) is thinner than 10 nm. Cracks were found from both particles, but the bare $LiCoO_2$ nanoparticles have more and larger cracks. The formation of the crack is due to the side reactions between the $LiCoO_2$ and the electrolyte. When Co^{4+} dissolution by electrolyte oxidation forms a SEI layer, localized $LiCoO_2$ corrosion creates such cracks. The Co^{4+} dissolution consumes the active weight and therefore the capacity decreases. The SEI layer impedes electron and Li ion transfer so that the performance can be degraded. Therefore, we believe that the thinner SEI layer and smaller cracks with the Li_3VO_4-coating can be attributed to the improved performance due to suppressed side reactions.

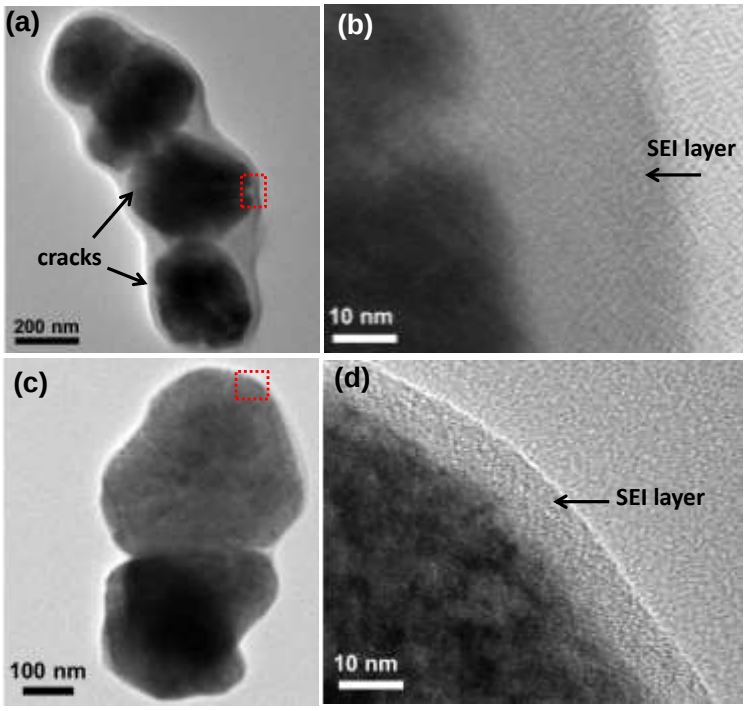

Figure 3.11 TEM images of bare $LiCoO_2$ nanoparticles (a) and an enlarged rectangular area in the image a (b); 5.5-wt.% Li_3VO_4-coated $LiCoO_2$ nanoparticles (c) and an enlarged rectangular area in the image c (d) after 50 cycles of 4.7 V charging/discharging. Cracks and SEI layers were indicated.

3.4 Conclusions

$LiCoO_2$ nanoparticles have been synthesized by a hydrothermal method. Facile wet coatings followed by sintering processes with NH_4VO_3 and LiOH were utilized to coat Li_3VO_4 on the surface of the $LiCoO_2$ nanoparticles. Our systematic studies revealed that the reaction between Li and vanadium oxides is favorable, resulting in Co_3O_4 due to the removal of Li from $LiCoO_2$ when the molar ratio of total Li to V is smaller than 3:1 (i.e., Li is deficient). With additional LiOH for the sintering process, only Li_3VO_4 without other byproducts was obtained while the structure and morphology of the $LiCoO_2$ nanoparticles were maintained. TEM images confirmed the presence of the Li_3VO_4 coating layer on $LiCoO_2$ nanoparticles as also indicated by the XRD results.

Electrodes containing 3.4, 5.5, and 22 wt.% Li_3VO_4-coated $LiCoO_2$ were prepared and their cycling performance and impedance characteristics were tested. When the electrodes were overcharged to 4.5 and 4.7 V, the performance was greatly improved due to the structurally protective but Li-ion conductive coating layer. For the electrodes with 5.5-wt.% Li_3VO_4-coated $LiCoO_2$, ~85 % of the first discharge capacity was retained after 100 galvanostatic cycles between 3 and 4.5 V at 30 mA/g (~0.2 C), compared with ~67 % of the electrode with the bare $LiCoO_2$ nanoparticles. At a current of 1200 mAh/g (~8 C) with cycling between 3 and 4.5 V, the electrode containing 5.5-wt.% coated $LiCoO_2$ still maintained 115 mAh/g discharge capacity, which is close to twice the capacity of the electrode with bare $LiCoO_2$ nanoparticles, indicating a greatly improved high-rate capability. TEM images showed that more cracks, which are the evidence for detrimental side reactions, from the bare $LiCoO_2$ compared to the coated $LiCoO_2$.

CHAPTER IV

LITHIUM METAL-FREE LITHIATED Si-S BATTERIES WITH IMPROVED CYCLABILITY AND SAFETY

4.1 Introduction

Reliable energy storage is the key for the development of electric vehicles (EV). Lithium intercalation-based lithium ion battery in today's market still cannot meet the requirements of EV, since a single charge is not able to power long distance driving (at least 500 km). [63] Lithium-sulfur (Li-S) battery, as one of the most promising solutions, has been attracting intensive investigations worldwide, due to its high energy density and low price. Sulfur has an overall redox reaction $S_8 + 16\ Li^+ + 16\ e^- \leftrightarrow 8\ Li_2S$, which yields a theoretical capacity of 1672 mAh/g [63, 116] and an average redox potential about 2.2 V (vs. Li/Li^+). When Li metal is used as anode (theoretical capacity of Li metal is 3860 mAh/g), the theoretical energy density of a Li-S full cell can be as high as 2567 Wh/kg, which is several times higher than that of transition metal based cathode materials. [63, 116] For example, the theoretical value of popular $LiCoO_2$-graphite based batteries is only 376 Wh/kg when $LiCoO_2$ capacity is considered as 140 mAh/g.[117]

However, two major problems hinder the commercialization of Li-S battery, i.e. the low electronic conductivity and polysulfides shuttle. Though various carbon nanostructures have been utilized to greatly improve the capacity by overcoming its low conductivity, [71, 118] the poor cyclability due to the polysulfide shuttle still remains unsolved. During the lithiation of sulfur, a series of polysulfides (Li_2S_x, x = 3~8) will be produced as intermediates, which can easily dissolve into organic solvent and diffuse to the lithium metal at the anode side, where they are reduced to solid precipitate. [116, 119] This shuttle process repeats with the cycling of the cell, reducing the active mass in the cathode, deteriorating the kinetics of the cell, and therefore leading to low columbic efficiency and fast capacity fading. Various strategies have been

proposed to suppress the capacity fading, including porous conductive sulfur reservoir in cathode, [76, 80, 120] porous carbon materials as polysulfides filter, [121] additives to the organic electrolyte, [81-82] and solid state electrolyte. [86a]

Despite the progress of Li-S battery, the safety hazard of Li metal makes the commercialization of Li/S battery difficult, due to the possible thermal runaway resulted from the formation of lithium dendrite and internal short-circuit. Even after decades of efforts, this challenge of Li metal anode has not been well solved, and no Li metal anode has been commercialized in rechargeable batteries.[122] An alternate option is to use Li metal-free anode materials. Silicon, possessing the highest theoretical capacity (4200 mAh/g) in anode materials[123], is the best choice to couple the high-capacity sulfur cathode, since there is no sacrifice of the high energy density compared with the Li metal-containing counterpart. Whereas, the large volume expansion (up to ~300%) of the lithiation of silicon makes the capacity fade rapidly.[123] Nanostructuring [45, 46b] and rigid binder [124] have been found being able to greatly improve the cyclability of Si anode. Several tentative studies have been reported to couple the Si and S, by either using lithiated Si-S (LSS) [122, 125] or Li_2S-Si [126]. However, all the reported performances of the full cell were much worse than that of the Li-S half cell, due to the coupled degrading of both the Si anode and S cathode.

In this Chapter, we present a LSS battery with stable cycling performances comparable with that of Li-S half cell. The LSS battery was designed with mesoporous structures in both the S cathode and Si anode. To accommodate the volume expansion, mesoporous Si was synthesized by magnesiothermic reduction of mesoporous silica (SBA15) and was further lithiated for the use of anode in full cell. Sulfur was infused into mesoporous carbon CMK-8, which provides both fast electronic transfer paths and reservoir for soluble polysulfides. A CNT paper was embedded between the sulfur cathode and separator in the LSS full cell to further block the

polysulfides shuttle. Stable cyclability of the LSS battery was achieved, which is much better than previous reported performances. More importantly, the LSS cells were found to be safe and reliable even under two common failure modes, internal and external short-circuit. On the contrary, for Li-S cells, excessive Li formed dendrites during charge, making the cell internally short-circuited and external short-circuit made cathode powdery. This chapter provides not only crucial information regarding the failure mechanisms, but also safer and more reliable operation of high-capacity and low-cost sulfur batteries, which are crucial for use in practice.

4.2 Experimental

4.2.1 Synthesis of S/CMK-8 cathode

CMK-8 replicating the template silica KIT6 was synthesized according to the method reported by Lang et.al.[127] For the Synthesis of KIT6, 4 g of Pluronic P123 and 7.9 g of 37 wt.% HCl were mixed in 144 ml H_2O under stirring at 35 ^oC for 4 h. 4 g of normal-butanol was added to the mixture. After 1 h, 8.6 g of TEOS was added and the mixture was kept in stirring for another 24 h at 35 ^oC. Subsepuently, the mixture was hydrothermally treated at 100 ^oC for 24 h. Then, the obtained powder was washed with H_2O and vacuum dried at 100 ◦C overnight. Finally the powder was annealed at 550 ^oC for 6 h in air.

To replicate KIT6, 2.5 g of sucrose was dissolved in 10 g of H_2O and 0.28 g of 97 wt.% H_2SO_4. Then 2 g of KIT6 was added and sonicated for 2 h. The mixture was heated in an oven at 100 ◦C and 160 ◦C for 6 h, respectively. The obtained powder was mixed again with 1.6 g sucrose, 0.18 g of 97 wt.% H_2SO_4 and 10 g of H_2O. After another 100 ^oC for 6 h and 160 ^oC for 6 h annealing, the collected powder was carbonized at 900 ^oC for 3 h in Ar atomsphere. CMK8 was finally obtained by removing the silica with 5 wt. % HF and washing with plenty H_2O.

Sulfur powder was mixed with CMK-8 with a weight ratio of S:CMK-8 = 6:4. The mixture was then annealed in Ar atmosphere at 155 ^oC for 12 h to infuse the molten sulfur into pores of

CMK-8. For the fabrication of sulfur cathode, S/CMK-8, carbon black, and poly(vinylidene fluoride) (PVDF) binder were mixed at a weight ratio of 80:10:10 in N-Methyl-2-pyrrolidone (NMP) to form a slurry (the sulfur weight percentage in the whole electrode is 48%.). Subsequently, the slurry was coated onto a 25 μm thick Al foil, and then vacuum dried at 50 oC for 12 h.

4.2.2 Synthesis of carbon-coated mesoporous Si (C-mSi)

SBA15 was first prepared according to a previous reported method.[128] 2 g of Pluronic P123 (poly(ethylene oxide)-b-poly (propylene oxide)-b-poly (ethylene oxide), Mw = 5800 g/mol) and 60 ml of 2 M HCl were mixed under stirring at 38 ◦C for 2 h. Then, 4.2 g of tetraethyl orthosilicate (TEOS) was added and the mixture was kept at 24 h at 35◦C without stirring. Subsepuently, the mixture was hydrothermally treated at 100 ◦C for 24 h. Then, the obtained powder was washed with H_2O and vacuum dried at 100 ◦C overnight. Finally the powder was annealed at 550 ◦C for 6 h in air.

Mesoporous Si was synthesized by a magnesiothermic method. Mesoporous SiO_2 SBA-15 was first prepared according to a previous reported method [129], and detailed description is in supplement. SBA-15 and magnesium powder (molar ratio of Mg:Si=2:1) was then mixed and grinded with a mortar. The mixture was then sealed in a 1/4" Swagelok coupling and transferred to a tube furnace with the flowing of 100 sccm of Ar. The temperature was ramped to 650 ^oC at a speed of 5 ^oC/min, and 2 h of annealing was conducted. The obtained powder was washed with 2 M HCl overnight and then 5 wt.% HF for 10 min. After wash with a lot of DI water, the obtained bright-brown Si powder was vacuum dried at 60 ^oC for 6 h. To obtain a carbon coating, the Si powder-filled crucible was transferred into a tube furnace, which was ramped to 800 ^oC in 30 min. with a flow of 100 sccm Ar, and then annealed for 15 min. with the flow of 100 sccm Ar +

20 sccm C_2H_2. By measuring the weight of the powder before and after the carbon coating, carbon contents in the power was estimated to be 31.7 wt.%.

4.2.3 Prelithiation of C-mSi

The Si electrode was fabricated by coating the slurry of C-mSi, carbon black, poly(acrylic acid) (PAA (Mw=100,000), Aldrich), and sodium carboxymethyl cellulose (CMC (viscosity 50–200 cP, 4 wt.% in H2O)), Aldrich) (weight ratio of 6:2:1:1 in DI water) onto Cu foil, which was then vacuum dried at 150 ^{o}C for 2 h. The lithiation of the Si electrode was conducted by pressing the Si electrode in direct contact with the Li metal foil between two glass slides with a clipper for 12 h in Ar-filled glove box. Several drops of electrolyte (1 M lithium bis(trifluoromethane) sulfonamide (LiTFSI)+1 wt.% $LiNO_3$ in dioxolane and dimethoxyethane (DOL:DME= 1:1 ratio by volume)) were added to wet the Si electrode and Li metal foil.

4.2.4 Synthesis of CNT interlayer

Single-walled carbon nanotubes (Cheap Tubes, Inc.) were dispersed in NMP for 1 h with a pen-type sonicator and another 1 h with bath-type sonicator. The obtained solution was filtrated and then vacuum dried at 120 ^{o}C for 20 h. The obtained CNT paper was punched into the electrode size for the use of battery cell.

4.2.5 Electrochemistry

The electrode was assembled into a 2023-type coin cell. For the assembly of half cell, Li metal foil was used as the counter electrode. For the LSS full cell, the S/CMK-8 cathode and lithiated C-mSi anode were used, and C-mSi:S weight ratio was about 1:1 (other than mentioned). For all coin cells, Celgard 2400 was assembled as the separator, and 1 M LiTFSI+1 wt.% $LiNO_3$ in DOL:DME (1:1 vol.) as electrolyte. When CNT interlayer was used, it was embedded between the S/CMK-8 cathode and the separator. Arbin BT2000 was used for the galvanostatic charge/discharge of the coin cells. The C-mSi half cell was cycled between 1.2 V ~

0.01 V, or between 1.2 V ~ 1000 mAh/g and 0.01 V. The Li/S half cell was cycled between 1.5 V ~3 V, and the LSS full cell was cycled between 1.4 V~3 V (other than mentioned). The C rate (1 C=1600 mA/g) and capacity of Li/S half cell and LSS full cell were calculated based on the weight of S.

External short-circuit was conducted by directly connecting the positive and negative electrode of the assebmbled Li-S half cell and LSS full cell with a Cu wire (~100 mOhm) for 3 h. The cell was subsequently charged at 0.5 C rate. For the internal short-circuit test, Celgard separator with 9 holes penetrated by a needle was used for the assembly of coin cell. Both the Li-S half cell and LSS full cell were then cycled at 0.5 C rate.

4.2.6 Structure characterization

X-ray diffraction (XRD) measurements were performed with a Bruker instrument (Bruker-AXS D8 VARIO) with Cu Kα radiation. The patterns were measured from 2θ = 15 to 75 degree with a step size of 0.01 ° and dwell time of 0.1s. Field-emission scanning electron microscope (SEM) and transmission electron microscope (TEM) were inspected with a JEOL JSM-7500F, and JEOL JEM-2010, respectively. For the SEM of Li metal foil and CNT interlayer after the test, they were first washed with plenty of DOL and sealed in a glass vessel in Ar-filled glove box, and then quickly transferred into SEM chamber with minimum exposure of atmosphere.

4.3 Results and discussions

4.3.1 Half-cell performances of S/CMK-8 cathode

Figure 4.1a and b show the SEM images of the CMK-8 before and after the impregnation of elemental sulfur. The size of S/CMK-8 particles was not significantly changed, confirming that most of the sulfur diffused into the inner pores. The major peak in the energy dispersive spectroscopy (EDS) spectra (inset of Figure 4.1b) of the S/CMK-8 was found to be sulfur. The TEM image of CMK-8 (Figure 4.1c) shows its ordered porous structure. After infusing melted S

into CMK-8 with 6:4 weight ratio of S:CMK-8, pores were completely filled as indicated by TEM image of S/CMK-8 (Figure 4.1d). The ordered mesoporous carbon CMK-8 was expected to function as an electrically conducting reservoir for polysulfides to improve both the rate capability and cyclability. CMK-8, replicated from KIT-6 silica template (cubic $Ia\bar{3}d$), has a 3-dimensional (3D) cubic structure with interpenetrating bicontinuous networks of channels.[127]

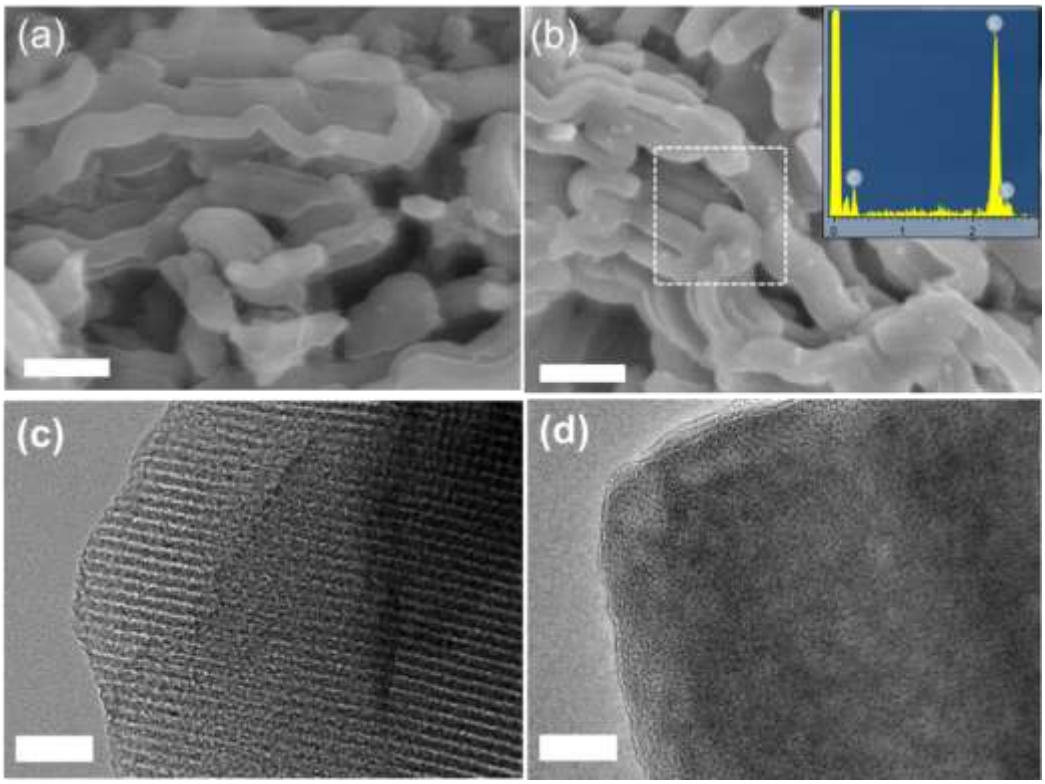

Figure 4.1 SEM image of CMK8 (a) and CMK8/S (b). The inset of (b) is the energy dispersive spectroscopy (EDS) of selected rectangular area. (c) TEM image of CMK-8 with ordered mesoporous structure. (d) TEM image of S/CMK-8 with completely filled pores by sulfur infusion. Scale bar is 2 μm for (a) and (b), 50 nm for (c) and (d).

Figure 4.2a compares the cycling performance of S/CMK-8 with different weight percentages of S in a half cell at 0.5 C (1 C = 1600 mA/g) with Li foil as the counter electrode. When the weight ratio of S:CMK-8 is 6:4 (i.e. 60 wt.% S), the first discharge capacity is 1055

mAh/g (calculated with the weight of S). The capacity quickly decreases to 770 mAh/g in the first 50 cycles with an average decreasing rate of 5.7 mAh/g per cycle, and then stabilizes at an average decreasing rate of as low as 0.3 mAh/g per cycle for another 100 cycles. The discharge capacity at the 150^{th} cycle is 740 mAh/g, resulting a capacity retention about 70% over 150 cycles. When the S weight percentage is increase to 70 wt.%, slightly quicker capacity fading is observed. The discharge capacity for the first cycle and 150^{th} cycle is 1060 mAh/g and 640 mAh/g, respectively, yielding a capacity retention of 60%. The high loading weight of S is attributed to the large pore volume and small pore size of the CMK-8, as indicated in the TEM image in figure 4.1c. As mentioned above, Porous CMK-8 can function as reservoir for the dissolved polysulfides, so that the polysulfides shuttle is suppressed and the capacity fading is stabilized. Particularly, the polysulfides inside the inner pores of CMK-8 are hard to dissolve and diffuse into the electrolyte. Therefore, for the last 100 cycles, nearly no capacity loss is found in both 60 wt.% and 70 wt.% cells. The slightly smaller capacity retention in the latter one is probably due to more sulfur is stay at the surface of the CMK-8 rather than inner pores.

The discharge potential profiles (Figure 4.2b) of the 60 wt.% cell shows two typical potential plateau around 2.3 V and 2.1 V (vs. Li/Li^+), respectively. Excellent kinetics of the cell can also be indicated from the small difference between the charge/discharge potential (~150 mV), which shows no significant increase over 150 cycles, indicating that the cell is not kinetically degraded. The columbic efficiency is over 90% for most of the cycles.

Figure 4.3 shows the excellent rate capability of the S/CMK-8 cathode (60 wt.% of S) in half cell. At 0.25 C rate, the initial discharge capacity is 1120 mAh/g, which decreases to 972 mAh/g in 8 cycles. The average discharge capacity at 0.5 C, 1 C, 3 C, 5C is 902 mAh/g, 812 mAh/g, 620 mAh/g, 416 mAh/g, respectively. After 50 cycles, a capacity of 846 mAh/g can be recovered at 0.25 C rate, corresponding to a capacity retention of 75%. According to the

potential profiles in figure 4.3b, the potential hysteresis (i.e. the difference between the charge and discharge potentials) increases slightly from 0.25 C to 1 C, but dramatically from 1 C to 5 C due to the greatly enlarged Ohmic overpotentials during the operation of the cell.

In order to further improve the cycling performances of the S/CMK-8 cathode, an interlayer of CNTs paper was embedded between the cathode and the separator, so as to block the polysulfides shuttle. Since the CNT interlayer is porous and conductive, it provides extra sites for the redox reactions of the arriving polysulfides. As a result, capacity retention can be further improved. Figure 4.4a shows the cycling performances of the Li-S half cell with and without the CNT interlayer at 0.5 C rate. Without CNT interlayer, the discharge capacity of the Li-S half cell decreases from the initial 1055 mAh/g to 760 mAh/g in 100 cycles, yielding a capacity retention of 72 %; with CNT interlayer, the capacity retention is improved to ~80% and the discharge capacity at the 100^{th} cycle rises to 906 mAh/g. The potential difference between charge and discharge is also a small as ~150 mV, as shown in the charge/discharge profile of Li-S half cell with CNT interlayer in figure 4.4b. Two plateaus at ~2.3 V and 2.1 V can also be observed.

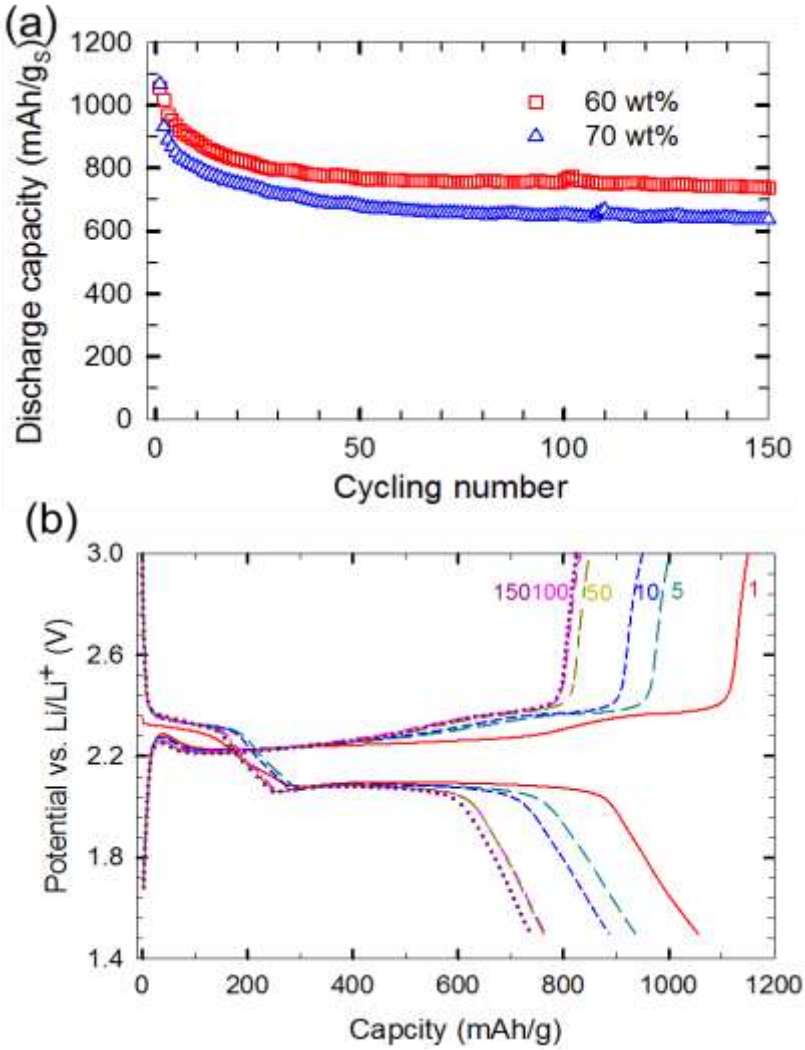

Figure 4.2 (a) Cycling performances of S/CMK-8 cathode with different weight percentages of S (i.e. 60 wt.% and 70 wt.%). (b) Charge/discharge potential profiles of S/CMK-8 cathode with 60 wt.% of S.

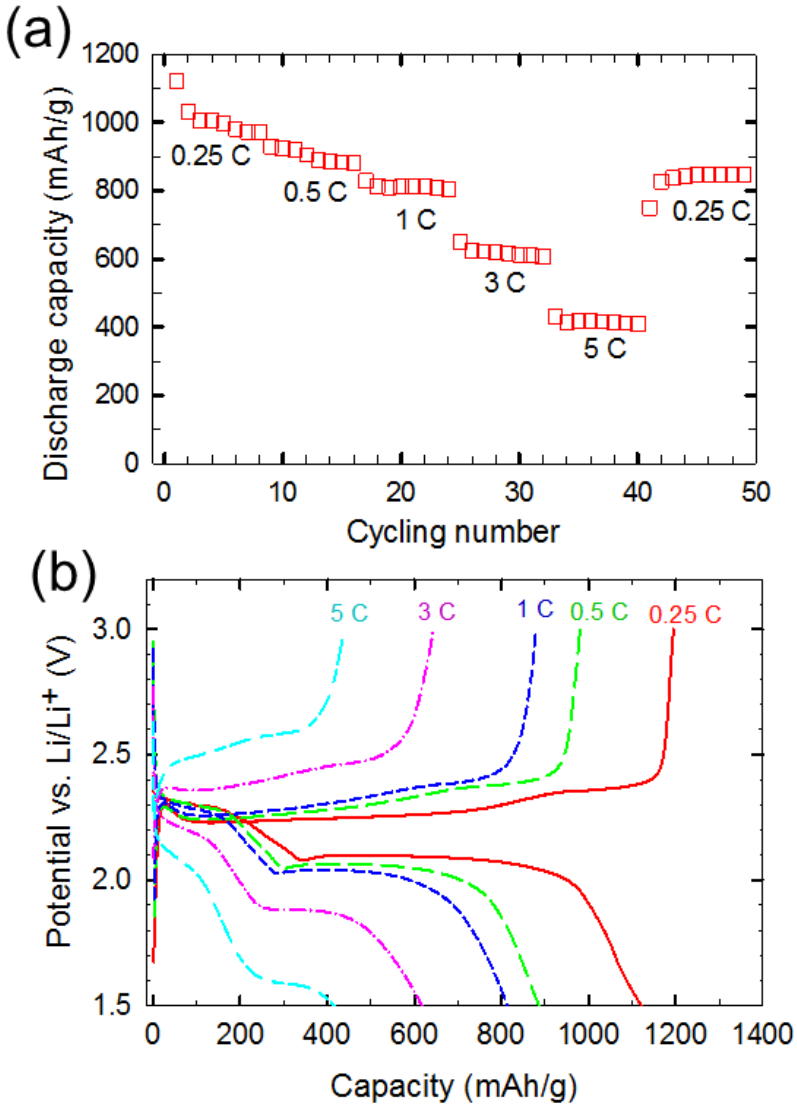

Figure 4.3 (a) Rate capability of Li/S half cell without CNT interlayer, and (b) the corresponding potential profiles at different C rates.

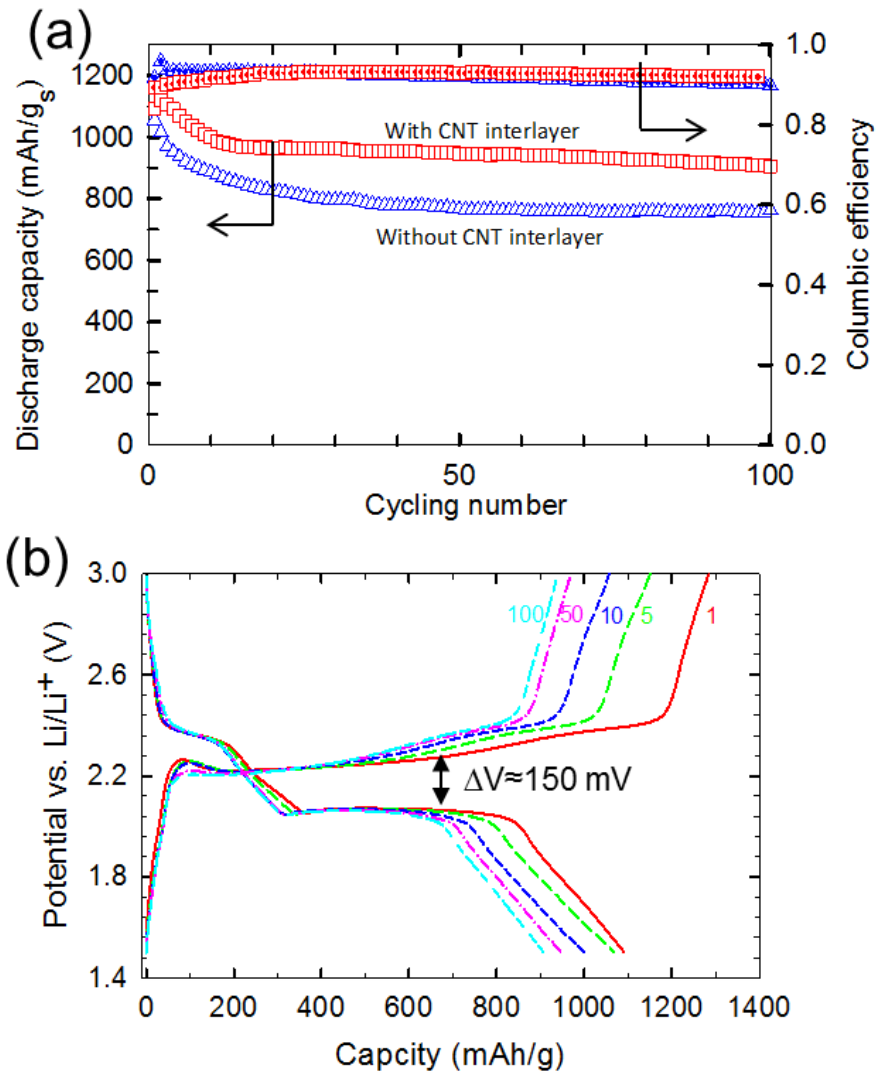

Figure 4.4 (a) The cycling performances of Li/S battery with and without CNT interlayer at 0.5 C (1C=1600 mA/g). (b) The charge/discharge potential profiles of the Li/S battery with CNT interlayer.

4.3.2 Half-cell performances of C-mSi electrode

SiO_2 has abundant source on the earth, which makes it a cheap starting material to produce nanosized Si for battery application. Because of the large volume expansion of Si when being operated in lithium batteries, the ideal design for Si is a highly porous structure with nanosized pores and "walls". On the one hand, the nanoscale features facilitate the charge transfer; on the

other hand, volume expansion can be accommodated by the pores. Meanwhile, a size-effect of the mechanical behavior of Si suggests that mechanical failure associated with delithiation/lithiation during battery operation can be greatly suppressed when the particle size drops to nanosacle. With these consideration, porous silica SBA15 was used as the starting material to synthesize nanosized Si with porous structure.

Magenoisothermic reduction was adopted, as it can reduce silica to Si by a reaction: $2Mg + SiO_2 \rightarrow Si + 2MgO$. Figure 4.5a shows the SEM image of the porous silica SBA15. SBA15 has a columnar shape with a length of ~1μm. After the reduction and subsequent removal of the residual products, the mesoporous structure of Si can be observed with SEM in figure 4.5b. The TEM images of the Si obtained from the reduction reaction of silica further confirms its highly porous structure, as indicated by figure 4.5c. The inset indicates the pore size is ~10 nm. The obtained mesoporous Si has a cubic (diamond) crystal structure, as indicated by X-ray diffraction (XRD) patterns (Figure 4.5e). Only a trace amount of residual MgO was observed due to a washing process with 2-M HCl and 5-wt.% HF. In order to further facilitate the charge transfer and to suppress the volume expansion, a subsequent carbon coating process by chemical vapor deposition (CVD) was conducted to introduce an outer layer of amorphous carbon with a thickness of 5~10 nm, as shown in figure 4.5d.

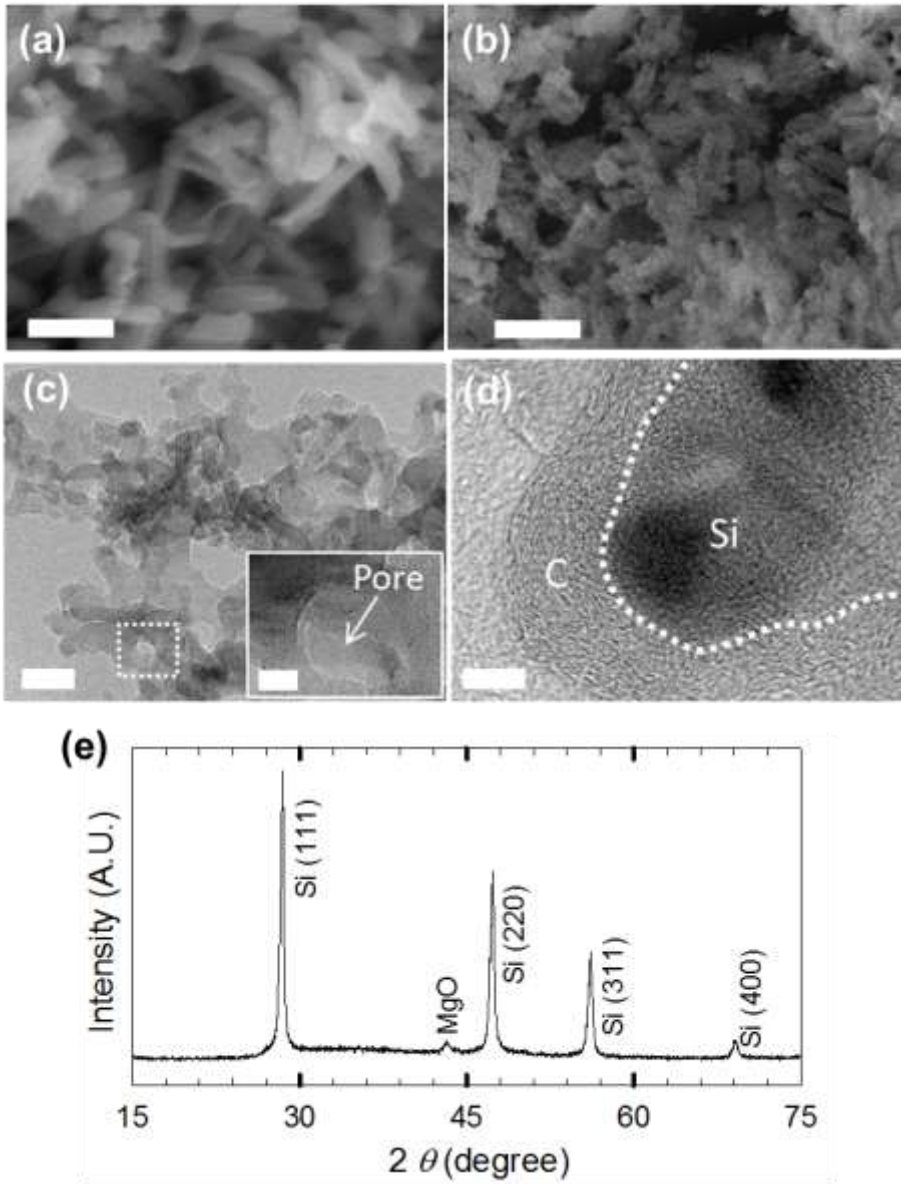

Figure 4.5 Mesoporous Si (mSi) Synthesis by magenoisothermic reduction of silica SBA15. SEM images of (a) pristine silica SBA15 and (b) mesoporous Si obtained by the mgneoisothermic reduction. (c) XRD of the mesoporous Si after washing away the MgO and SiO_2 residual. (d) TEM image of mesoporous Si showing highly porous morphology. The inset of (c) shows one pore of the mesoporous Si. (e) TEM image of the carbon-coated mesoporous Si (C-mSi) with several nanometer-thick coating layer of carbon. The scale bar is 1 μm for (a) and (b), 20 nm for (c), 5 nm for the inset and (d).

The cycling performances of the carbon-coated mesoporous Si (C-mSi) in a half cell configuration (with Li counter electrode) at 1 A/g is shown in figure 4.6a. When cycled with complete lithiation/delithiation between 0.01 V~ 1.2 V, it shows a capacity of 2550 mAh/g at 0.1 A/g for the first cycle (calculated with the total weight of C-mSi), which is more than 6 times higher than that of today's commercial graphite electrode. Since the weight percentage of the amorphous carbon coating is about 31 wt.%, this initial lithiation capacity at low current rate is close to the theoretical value. For the following cycles, current density of 1 A/g is used. The first discharge capacity at 1 A/g is 2120 mAh/g, only slightly smaller than the capacity at 10 times slower rate (i.e. initial 0.1 A/g). This indicates excellent high-rate capability of the C-mSi, due to the use of carbon coating and nanosized porous features. After cycled for the 100 cycles, a capacity of 1240 mAh/g at 100^{th} cycle and corresponding capacity retention of 58% were obtained.

Figure 4.6b shows the charge/discharge profile of the C-mSi electrode. The initial cycle at 0.1 A/g rate shows a relatively large irreversible capacity ~400 mAh/g. This is mainly because of the formation of SEI layer on C-mSi electrode, which consumes a portion of the active materials in the electrode. For the following cycling, nearly no irreversible capacity was found, leading to a columbic efficiency close to 1, as shown in figure 4.6a. The initial cycle shows a delithiation potential ~0.1 V and a lithiation potential ~0.4 5V.

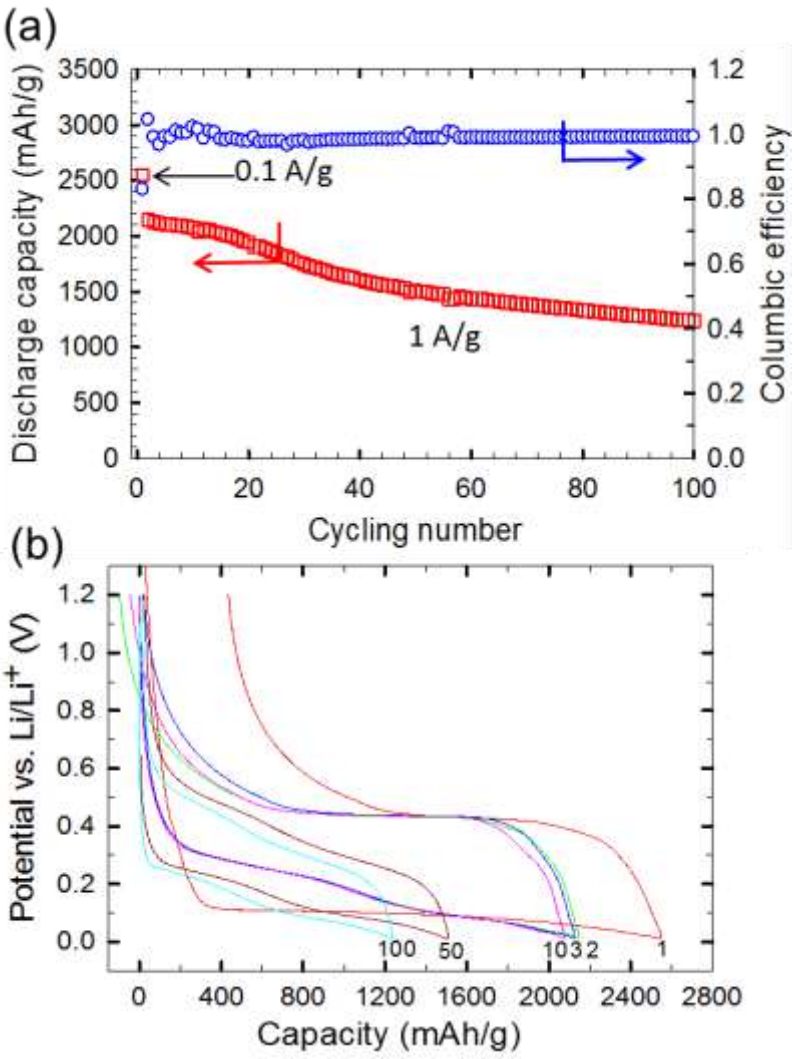

Figure 4.6 (a) Cycling performance of the C-mSi in half cell cycled between 0.01 V~1.2 V. The first cycle is at 100 mA/g, and the following cycles are at 1 A/g. (b) Corresponding potential profiles of the C-mSi.

4.3.3 Pre-lithiation of the C-mSi anode

In order to assemble the C-mSi and S electrodes into a full cell, it is necessary to lithiate one of the electrodes. Lithiation of silicon electrode was chosen in this study because of the difficulty in handling Li_2S due to its high reactivity to moisture in atmosphere. Facile lithiation of Si by making direct contact of the Si electrode with a Li metal was performed by taking

advantage of the difference between electrochemical potentials of Si and Li.[125b] The C-mSi can be reduced and lithiated by Li metal when a direct electrical contact is made. A Li metal foil was clamped with the C-mSi electrode soaked by an electrolyte (1 M LiTFSI + 1 wt.% $LiNO_3$ in DOL:DME) between two glass slides with a clipper for 12 h, so as to have a uniform and complete lithiation. The complete lithiation of Si was confirmed by the charge profile of the pre-lithiated C-mSi electrode at 100 mA/g in a half cell, as indicated in figure 4.7a, which shows a delithiation capacity up to 2997 mAh/g. As mentioned above, weight perentage of carbon is about 31 wt.%, so this delithiation capacity is close to the theoretical value.

The complete lithiation can also be confirmed by the XRD of the lithiated C-mSi electrode (see Figure 4.8), which indicates Si peaks vanished and Li_xSi peaks appeared after lithiation. Figure 4.7b shows the cycling of the lithiated C-mSi electrode with charge limit set to 1.2 V, and the discharge limit set to 1000 mAh/g or 10 mV. We intentionally kept the discharge limit to 1000 mAh/g (i.e. partial lithiation of Si) so as not to have a large volume expansion that causes quick capacity fading. The capacity was maintained to be 1000 mAh/g up to 290 cycles, and then decreased to 880 mAh/g at the 300^{th} cycle. The cut-off discharge voltage (as shown in the inset of Figure 4.7b) keeps diminishing but the capacity remained unchanged for the first 290 cycles. During the first 290 cycles, the C-mSi was not completely lithiated/delithiated for each cycle, and thereby the volume expansion did not reach the maximum, allowing for long stable cycling performance. If smaller discharge capacity limit (*e.g.*, <1000 mAh/g) is used, even longer stable cycling is expected because of less volume change. [125a]

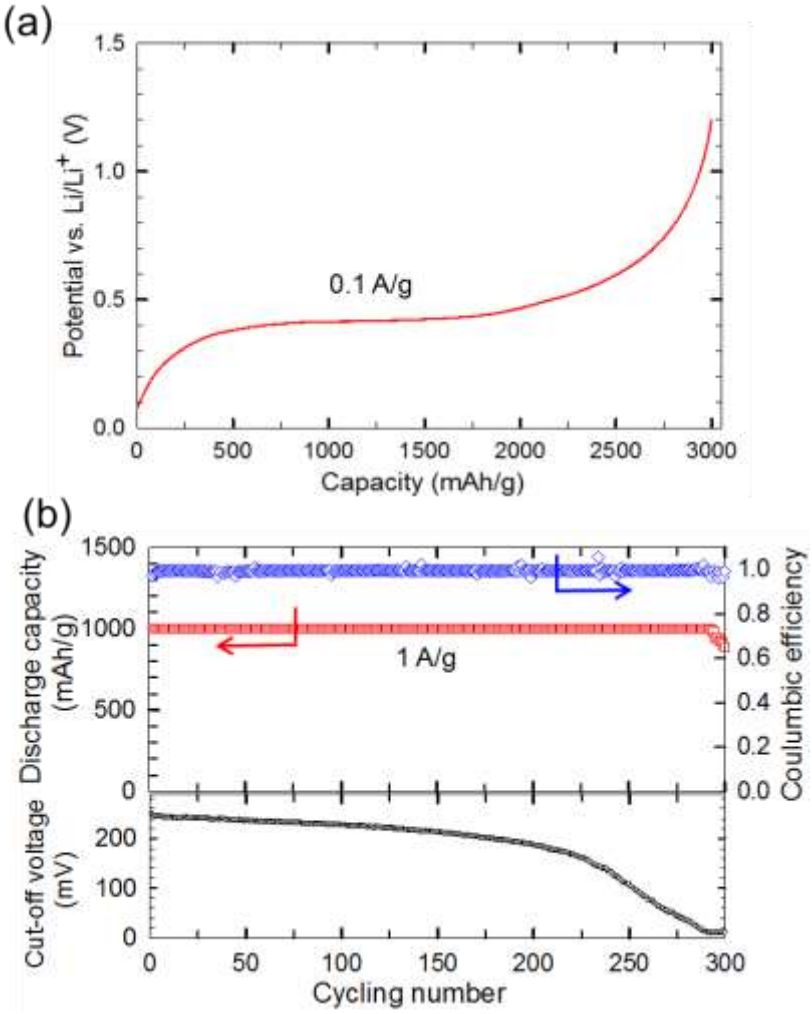

Figure 4.7 (a) Charge profile of a lithiated C-mSi electrode at 0.1 A/g. (b) Cycling performances the lithiated C-mSi electrode at 1 A/g with a charge limit of 1.2 V and discharge limit of either 1000 mAh/g or 10 mV (upper plot), and corresponding cut-off voltage (lower plot).

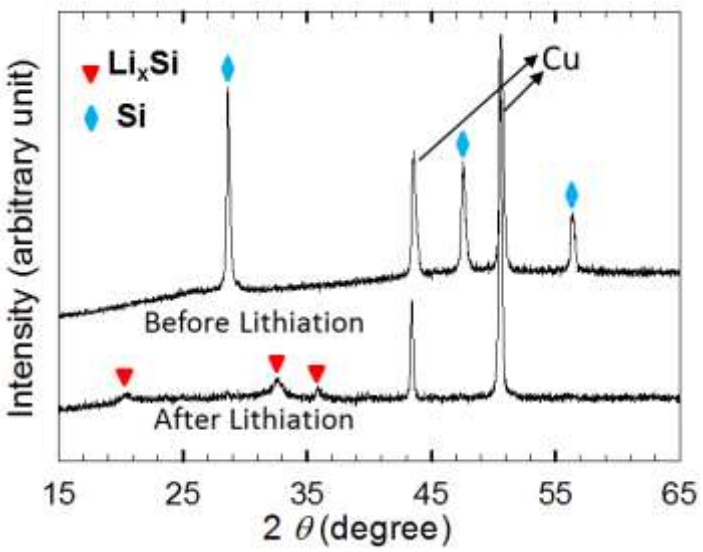

Figure 4.8 XRD of C-mSi electrode before and after the lithiation by pressing the electrode with Li metal.

4.3.4 Performances of lithiated Si-S (LSS) full cell

The LSS full cells with and without the CNT interlayer were tested and their cycling performances are shown in figure 4.9. The LSS full cell "without" CNT interlayer has an initial discharge capacity of 875 mAh/g, which is smaller than that of its counterpart in half cell (see Figure 4.4a). After 100 cycles, the capacity decreased to 550 mAh/g, yielding a capacity retention of 63%. When CNT interlayer was inserted, the discharge capacities of the 1st and 100th cycle increased to 970 mAh/g and 780 mAh/g, respectively, resulting in a capacity retention of 80% at 100th cycle. Although the capacities of the LSS full cells are slightly smaller than that of their half cell counterparts, the capacity retentions are comparable. To our best knowledge, this is the highest cycling performance reported by far for LSS full cells with liquid organic electrolyte. The discharge potential profiles (see Figure 4.9b) of the LSS full cell at 0.5 C rate show two typical potential plateaus, ~2.2 V and ~1.6 V, slightly lower than those of the Li-S cell due to the 0~0.45 V (vs Li/Li$^+$) delithiation potential of the Si electrode, as shown in figure 4.6b.

The voltage difference (0.4 V~0.7 V) between charge and discharge of the LSS full cell was observed to be slightly larger than those of the Li-S cell (see Figure 4.4b). The improvement in the cyclability can be attributed to the bi-functional CNT interlayer, which functions as a reservoir to capture the soluble polysulfides and a current collector by providing electron transfer paths.[121, 130] A layer of sulfur was observed on the CNT layer at the charged state in the SEM image (Figure 4.10a) and confirmed by the EDS (the inset of Figure 4.10a), in comparison to the visible CNT bundles before cycling (Figure 4.10b).

The rate capability of the LSS full cell with CNT interlayer and the corresponding voltage profile are shown in figure 4.11. The cut-off discharge voltage was 1.4 V for 0.25 C and 0.5 C; 1.3 V for 1 C and 2 C; and 1.2 V for 3 C. At 0.25 C rate, the discharge capacity was measured to be 1070 mAh/g and 960 mAh/g for 1^{st} and 8^{th} cycle, respectively. The average discharge capacity at 0.5 C, 1 C, 2 C, and 3 C was 823 mAh/g, 748 mAh/g, 540 mAh/g, and 465 mAh/g, respectively. After 48 cycles, a capacity of 939 mAh/g can be recovered at 0.25 C rate, corresponding to a capacity retention of 87%. The rate capability of the LSS full cell is comparable with that of Li-S cell (see Figure 4.4).

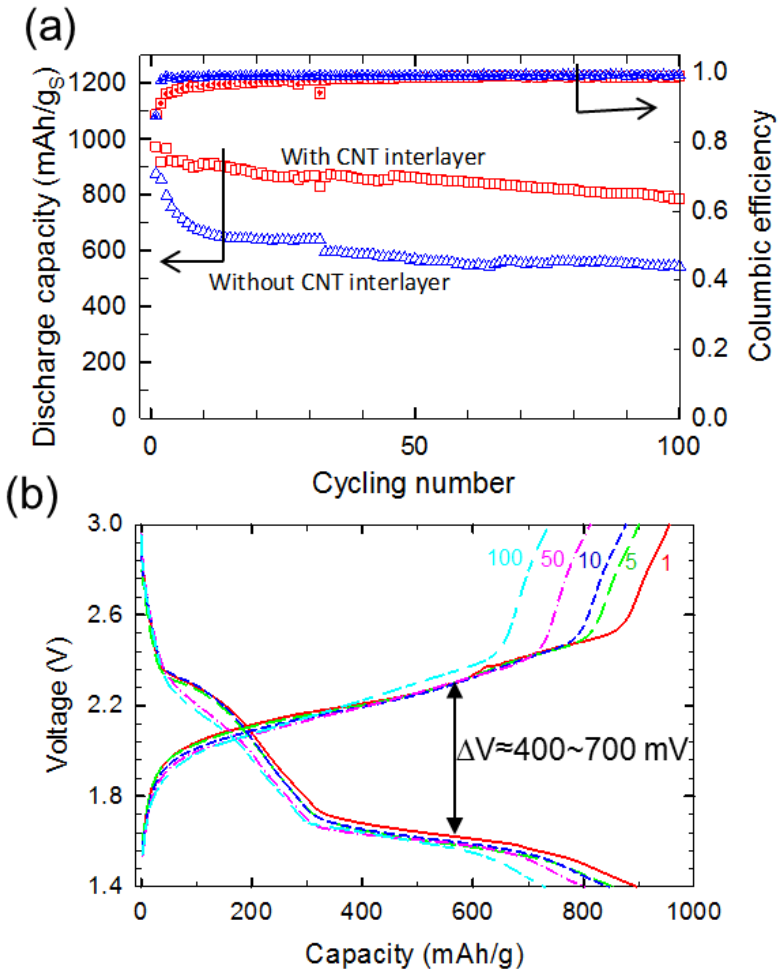

Figure 4.9 (a) The cycling performances of LSS battery with and without CNT interlayer at 0.5 C. (b) The charge/discharge voltage profiles of the LSS battery with CNT interlayer.

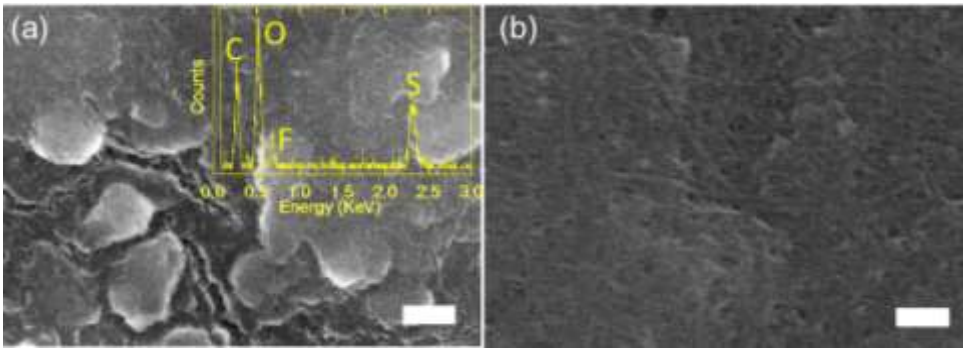

Figure 4.10 The SEM images of the CNT interlayer before (b) and after (a) 100 cycles of charge/discharge. The inset of (a) is the EDS of the CNT interlayer at charged state after 100 cycles, showing the presence of sulfur covering the CNT networks. The scale bar is 200 nm.

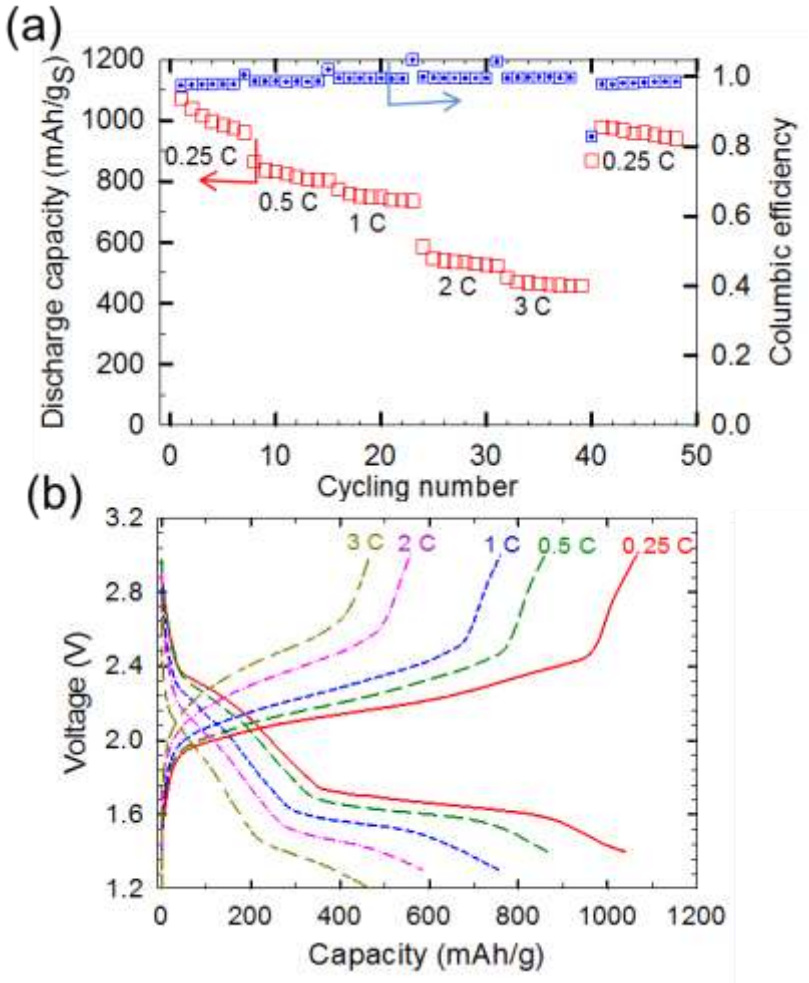

Figure 4.11 (a) Rate capability of the LSS battery, and (b) corresponding voltage profiles.

Different from the abundant Li source in Li/S half cell, Li source in the LSS full cell is limited by the delithiation capacity of the lithiated Si, which however decreases rapidly because of the consumption of Li by solid electrolyte interface (SEI) layer on both electrodes, the reduction of accessible lithiated Si due to its mechanical failure, and the loss of Li due to polysulfides shuttle. As shown in figure 4.12, when the Si:S weight ratio is reduced to 0.75, a transition from stable cycling to rapid degrading appears at the 80^{th} cycle, indicating that the dominant capacity fading changes from sulfur cathode to silicon anode. When electrochemically accessible lithiated Si is excessive, only partial lithiation/delithiation of the Si is need for each cycle, so that the observed decrease of the capacity is mainly due to the sulfur cathode. After 80 cycles, the remaining reversible Si is completely delithiated/lithiated for each cycle and the degrading is thus accelerated, similar as what observed in the last 10 cycles in Li/Si half cell (Figure 4.7b). Therefore, slightly excessive lithiated Si is favorable for better cyclablitiy when designing Si-S battery. On the other hand, by optimization of Si anode with better binder or nanostructure, excellent cycling over 1000 cycles with complete lithiation/delithiation has been reported in Li/Si half cell, which, if used in LSS full cell, is expected to achieve much better cyclability. [46b, 124a]

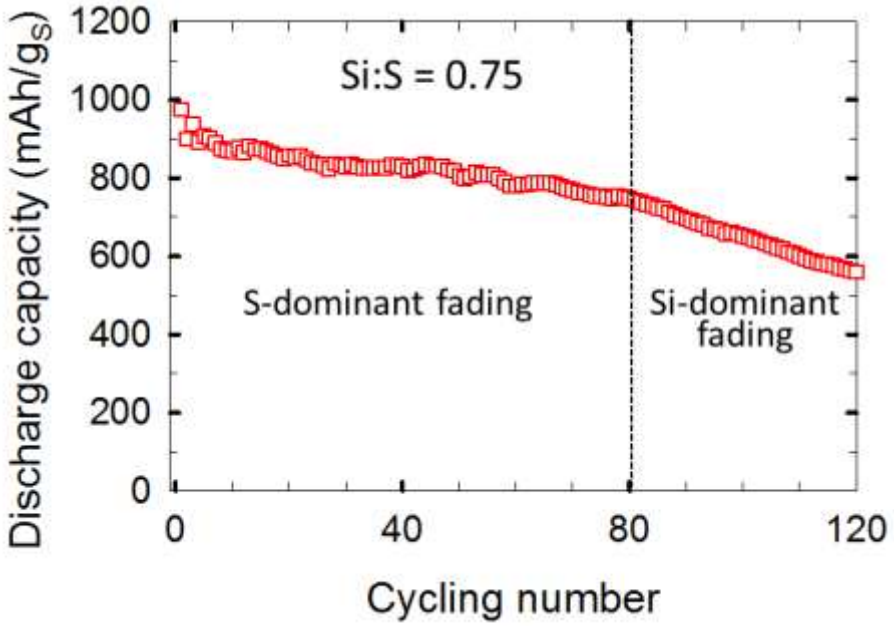

Figure 4.12 Cycling performances of a LSS full cell with C-mSi:S weight ratio of 0.75.

4.3.5 Short-circuit

Both LSS cell and Li-S cell were further studied under common failure conditions – an internal short-circuit upon repeated charge/discharge and an external short-circuit due to improper wiring. These often make Li-S battery unsafe and unreliable, which are very important aspects to be resolved for practical use. In this study, the internal short-circuit was simulated by creating holes on a separator membrane, as can be seen in the inset of figure 4.13a. The Li-S half cell cannot be recharged after delivering a capacity of ~800 mAh/g for the initial discharge at 0.5 C rate, as shown in figure 4.13a. During the charge, voltage suddenly dropped, indicating internal short circuits. On the contrary, the LSS cell was discharged/charged over 40 cycles with a discharge capacity of 925 mAh/g and 720 mAh/g for the 1^{st} and 40^{th} cycle, respectively, at 0.5 C rate, as shown in figure 4.13b. This indicates that the LSS cell is relatively immune to dendrite formation, which is one of the major factors that make Li-S batteries unsafe.

The failure of the Li-S cell occurs because of a Li dendrite formation accelerated on the Li metal at the pre-made holes of the separator membrane. As illustrated in figure 4.14b, Li metal dissolution creates a large number of pits during the discharge process. The SEM images after the first discharge clearly indicate a few 100 μm pits, suggesting excessive Li has been lost from the Li metal. It should be noted that the pristine Li metal has smooth surface as confirmed by the SEM image shown in figure 4.14a. Upon the charge process, Li deposition is favorable through the holes due to less resistance, leading to a rapid growth of Li dendrites (Figure 4.14c). The SEM image shows a selective Li deposition showing a circular-shape edge. Several extra dendrites formed at other holes can be seen in figure 4.15. The similarity in the size and shape of the formed dendrite to the premade holes on separator membrane confirms the favorable growth of dendrite at the pre-made holes. When the dendrite reaches the surface of cathode, the cell becomes internally shorted. Once a short-circuit occurs, Li metal reacts vigorously with cathode, lowering the cell voltage (as shown in Figure 4.13a), which may trigger a thermal runaway for large-scale cells. In a Li-S cell without intentionally created holes on a membrane, heterogeneous nucleation for creating Li dendrites could start from grain boundaries or surface scratches on Li metal anode, and the dendrites may be formed at a high rate with a condition of a high operating current. As for the LSS cell, Li is alloyed with Si during the charge, alleviating the dendrite formation. Excessive Li dissolution can be avoided and thereby a Li deposition on anode becomes unfavorable.

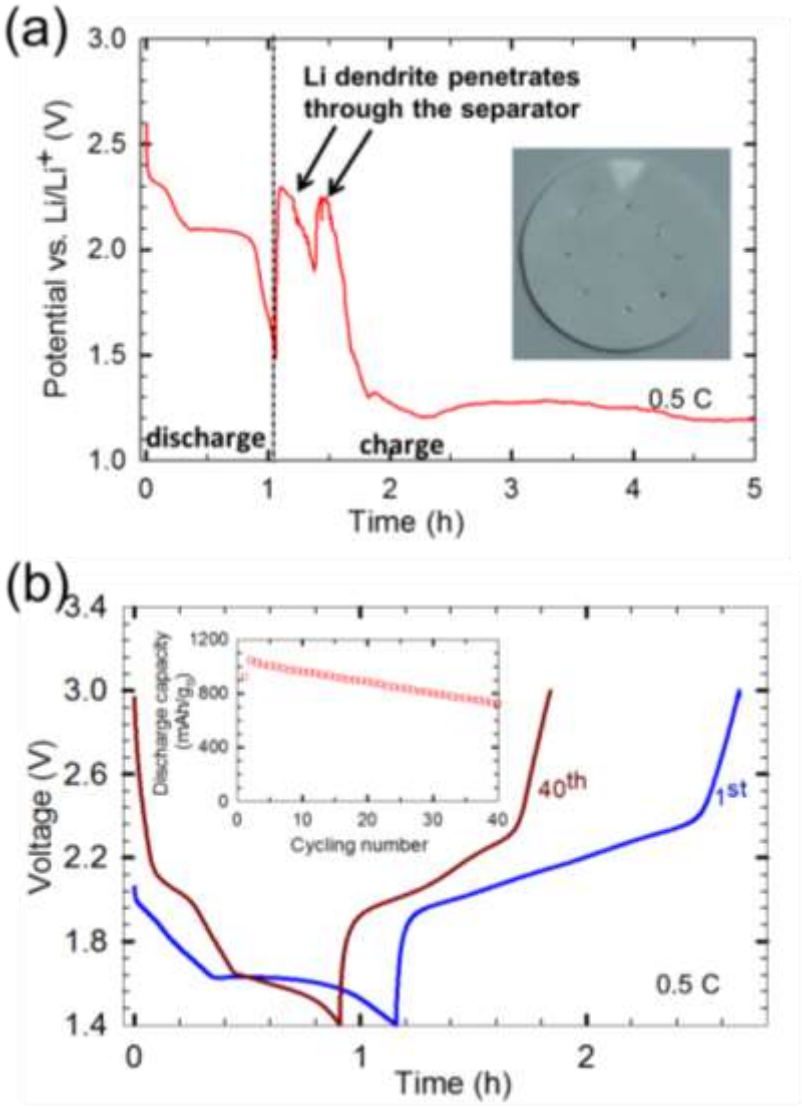

Figure 4.13 The discharge/charge profiles of batteries assembled with separator with premade holes: (a) Li-S battery and (b) LSS battery. The inset of (a) is the photograph of the separator showing the premade holes. The inset of (b) is the cycling performance of the LSS battery.

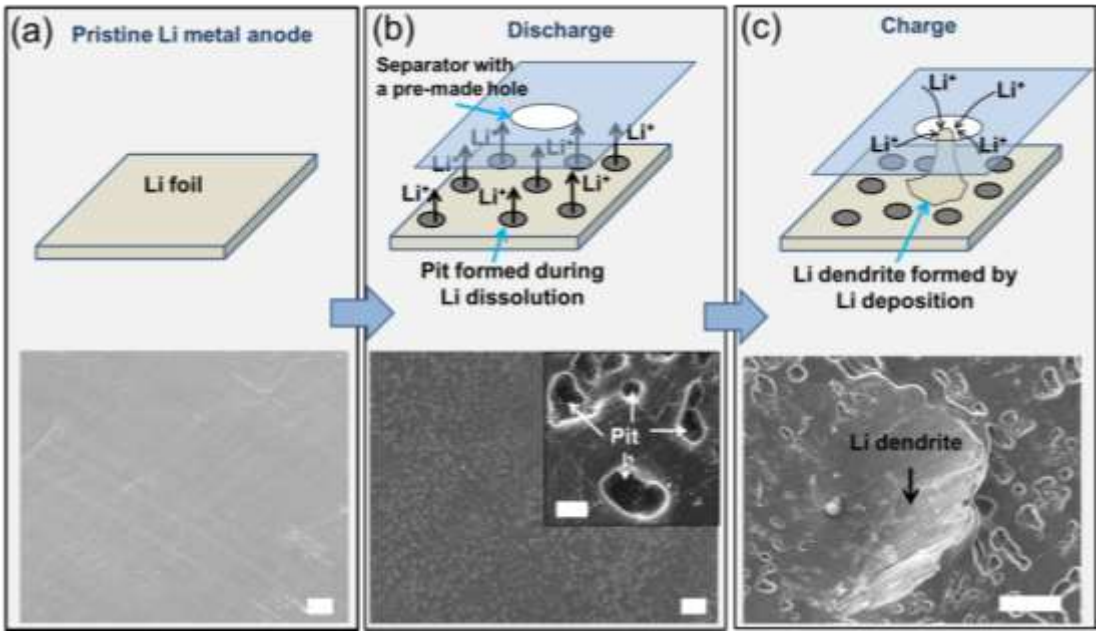

Figure 4.14 The schematics and SEM images of the morphology evolution of the surface of Li metal in Li-S battery: (a) prestine Li metal foil, (b) after the first discharge and (c) after the internal short-circuit during charge. The scale bar is 200 μm for (a) and (b), 20 μm for the inset of (b), and 100 μm for (c). All the charge/discharge was conducted at 0.5 C.

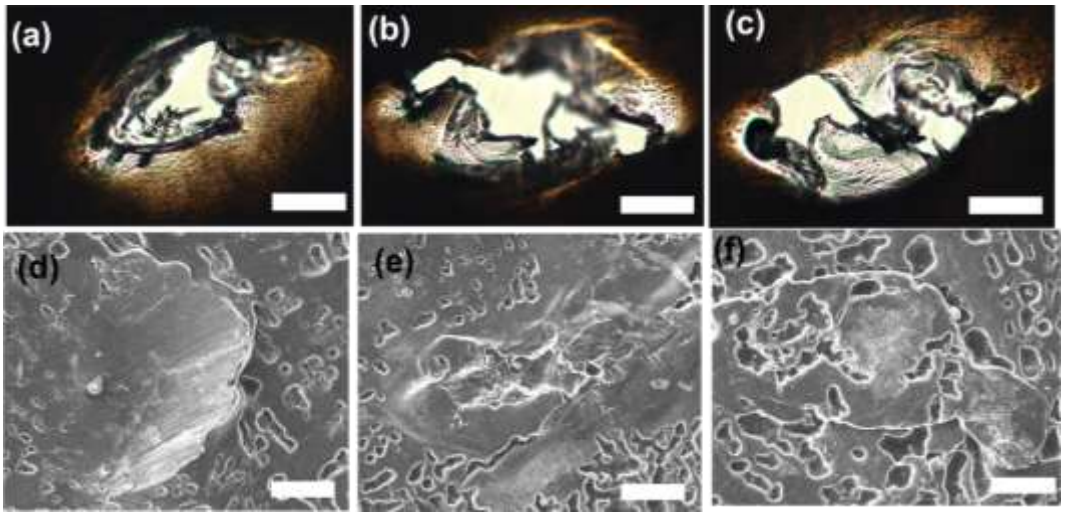

Figure 4.15 Comparison of the pre-made holes on separator (a~c) and the Li protrusions (d~f) formed on Li metal surface. The optical image of the holes was taken with the light passing through from the bottom. The bright white region is the hole. Scale bar is 100 μm.

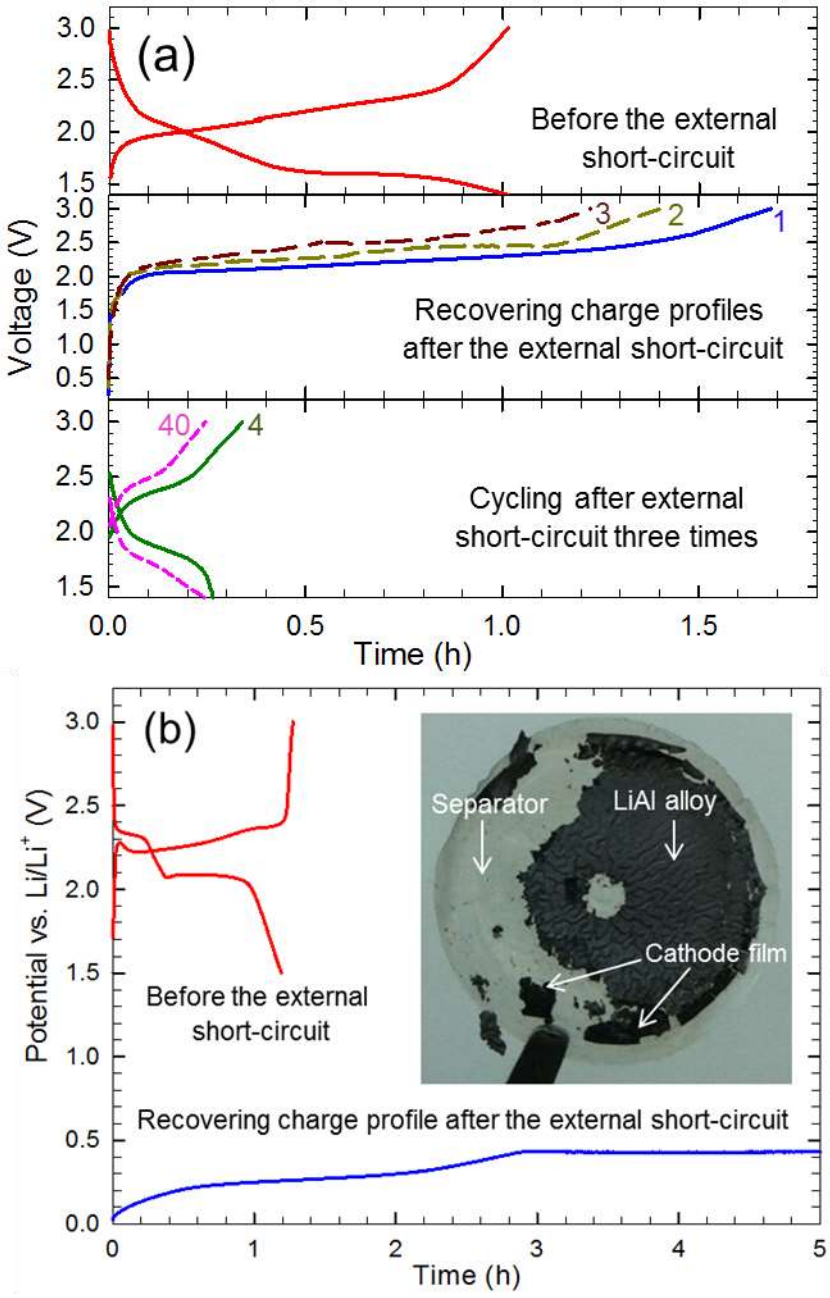

Figure 4.16 (a) The charge/discharge profile of a LSS battery before external short-circuit (first row), the recovering charge profile after three times of 3 h's external short-circuit with Cu wire (second row), and the voltage profiles of 4th and 40th cycle of the LSS battery after external short-circuit (third row). (b) The charge/discharge profile of a Li/S battery before external short-circuit, and the recovering charge profile after the first external shor-circuit. The inset of (b) shows the completely corroded Al current collector after the recovering charge. All the charge/discharge was conducted at 0.5 C rate.

Another common failure mode, an external short-circuit was also tested for both LSS and Li-S cells. After 6 cycles of normal charge/discharge at 0.5 C rate, the charged LSS cell was externally short-circuited with a 100 mOhm copper wire for 3 hours, and then was charged back to 3 V at 0.5 C rate. Even after repeating the external short-circuit 3 times for 3 hours each, the LSS cell was recovered and charged back to 3 V, as shown in figure 4.16a. The following cycling (1.4 ~ 3V) of this LSS cell still showed a reversible discharge capacity of 200~250 mAh/g for about 40 cycles at 0.5 C rate even after the severe conditions for degradation. In the contrast, the Li-S cell cannot be recovered after the first external shortcircuit. As shown in figure 4.16b, the Li-S cell, delivering a capacity of 940 mAh/g before shortcircuit, cannot be charged back to 3 V and shows a voltage constant at ~0.43 V. This is because the Al current collector was alloyed with Li and formed the Li-Al alloy during the external short-circuit[131], which becomes white color powder after the extraction of Li ion during the following Li extraction charge, as shown by photograph (the inset of Figure 4.16b) of the cathode detached from the Li-S cell. As the Li-S cell is cathode-limiting in this study (Li metal anode is excessive), anode-limiting Li-S cell should be adopted.

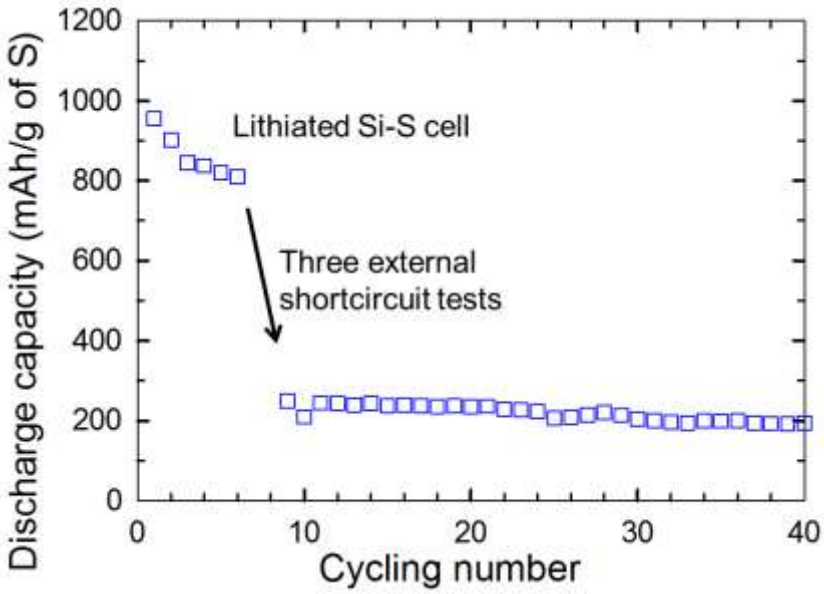

Figure 4.17 Cycling performances of a LSS battery before and after external short-circuit experiment at 0.5 C rate.

4.4 Conclusions

In summary, a lithium metal-free LSS full cell was designed with mesoporous active materials in both lithiated Si anode and S cathode. Stable cycling with capacity retention of 80% over 100 cycles was achieved, which is by far the best cycling performances for LSS full cell with the organic electrolyte. The LSS full cell also showed excellent high-rate capability, delivering a discharge capacity of 465 mAh/g even at 3 C rate. The excellent electrochemical performances were attributed to the alleviation of the volume variation with a mesoporous lithiated Si and the suppression of polysulfides shuttle with porous carbon CMK-8 and bi-functional CNT interlayer. We also demonstrated the better reliability and safety of the LSS battery over Li-S battery with the internal and external short-circuit experiments. LSS battery has no issue of Li dendrite formation; whereas, Li-S battery suffers from the rapid Li dendrite nucleation and growth at heterogeneous spot, which could result in the internal short-circuit and thermal runaway. This failure mechanism in Li-S battery was discussed based on the ex-situ

observation of the Li surface by SEM images. The external short-circuit experiment also showed that Li-S battery, comparing with LSS battery, is more prone to fail due to the corrosion of Al current collector. Anode-limiting design should be adopted for a battery countered with Li metal anode. We believe the demo of the LSS battery designed in this study makes valuable contributions for the commercialization of LSS battery in the near future.

CHAPTER V

SEMI-LIQUID Li-S BATTERY WITH CARBON NANOTUBES SPONGE AS CONDUCTIVE RESEVIOR OF CATHOLYTE

5.1 Introduction

As described in last chapter, Li-S batteries are promising energy storage devices to power electric vehicles for long-distance driving per charge (>500 km). [63] Sulfur has an overall redox reaction $S + 2\ Li^+ + 2\ e^- \leftrightarrow Li_2S$, which yields an average redox potential about 2.2 V (vs. Li/Li^+) and a theoretical capacity of 1672 mAh/g [63, 116], which is an order of magnitude higher that of lithium transitional metal-based Li-ion batteries ($LiCoO_2$, $LiFePO_4$, etc.). When Li metal is used as anode, the theoretical energy density of a Li-S cell can be as high as 2567 Wh/kg, which is also several times higher than that of todays' Li-ion batteries. [63, 116] For example, the theoretical value of popular $LiCoO_2$-graphite based batteries is only 376 Wh/kg when $LiCoO_2$ capacity is considered as 140 mAh/g.[117]

However, two major problems hinder the commercialization of Li-S battery, i.e. the low electronic conductivity and polysulfides shuttle. Both S and the discharge products (Li_2S_2 or Li_2S) are insulating materials, which leads to the sluggish kinetics of the cell. Thick layers of S formed at charged state or Li_2S formed at discharged state will impede the charges (electrons and Li ions) diffusion in the solid phase, resulting in the incomplete utilization of the S and low specific capacity. The polysulfides shuttle results from the dissolution of intermediates polysulfids (Li_2S_x, x = 3~8) in the organic electrolyte. During the operation of the cell, polysulfids shuttle to the Li metal anode, and are reduced into solid precipitates on the Li metal surface, leading to low columbic efficiency and rapid capacity fading.

The most common approach to address these issues by far is to impregnate elemental sulfur into conductive porous materials, such as porous carbon[74, 80] and conductive polymers[73, 76]. On

the contrary to start from solid sulfur, a less-taken approach is to use the liquid catholyte as the active materials by taking advantage of the high solubility of the polysulfides in organic electrolyte. Comparing to the sluggish reaction within the insulating solid sulfur, liquid catholyte (i.e. polysulfides dissolved in organic electrolyte) can alleviate the passivation of irreversible S and Li_2S in the electrode and achieve a higher utilization of active materials. Rauh et al.[132] first reported a semi-liquid Li-polysulfides catholyte battery and achieved high utilization of active materials (1.6 electron per sulfur atom). One challenge for this approach is to design a reservoir which not only confines the liquid catholyte but also provides paths for electrons' transfer. If the design of a flow battery is adopted, the complex configuration and using of accessory parts (like pump, tubing, valve, etc.) reduce the cell energy density and make it unsuitable for mobile applications.[133] Recently, several studies have been reported to employ different porous structures as the reservoir for the polysulfides catholyte, such as Ni foam[134], Ketjen black[135], and CNT paper[136]. But, the electrochemical performances are generally still not satisfactory, especially the small loading of sulfur, low capacity, and short cycling life.

In this chapter, we designed a novel semi-liquid Li-S battery with highly porous carbon nanotubes (CNT) sponge as the "super-reservoir" for the catholyte. The highly hydrophobic CNT sponge is synthesized by a chemical-vapor deposition method, which has been reported to be able to absorb organic solvents hundreds of times higher than its own weight due to its high porosity and large surface area.[137] Meanwhile, this CNT sponge has shown excellent mechanical flexibility and can be used as a current collector without binder.[137-138] The catholyte is prepared by dissolving chemically-derived polysulfides in the electrolyte. CNT sponges with different diameter and density are assembled in the semi-liquid Li-S batteries. The effect of the density and diameter on the electrochemical performances has been studied. Effect of the cahtolyte loading volume, the sulfur loading weight, and the concentration of the cahtolyte on the battery

performances have aslo been systematically investigated. Our semi-liquid Li-S battery with high sulfur loading has achieved high capacity, high energy density, high rate capability and stable cycling performaces.

5.2 Experimental

5.2.1 Synthesis of catholyte

Polysulfides cathoolyte (Li_2S_6) was synthesized by directly react elemental sulfur with stoichiometric Li_2S in electrolyte. First, 1 M LiTSFI + 0.5 M $LiNO_3$ was dissolved in the solvent DOL:DME = 1:1 (by volume). Then, S and Li_2S at a molar ratio of 5:1 were added into the electrolyte to form 2 M and 4 M Li_2S_6 (molar concentration calculated with S atom). The mixture was sealed in a glass vessel in an Ar-filled glove box and brought out for heat treatment in an oil bath at 90 ^oC for 3 days with continuous stirring. The yellowish solution (see Figure 5.1) will be used as catholyte in semi-liquid Li-S batteries.

Figure 5.1 Photograph of polysulfides catholyte (Li_2S_6 dissolved in electrolyte)

5.2.2 Synthesis of carbon nanotubes sponge

CNT sponge was synthesized by a CVD methods similar to that reported by Gui et al [137]. Ferrocene and 1,2-dicholorbenzene will be used as the sources of Fe catalysts and carbon, respectively. 60 mg/ml of ferrocene dissolved in 1,2-dichlorobenzene was continusouly delivered into a 1-inch quartz tube by a syringe pump at a feeding rate of 6 ml/h or 12 ml/h. The quartz tube was heated with a 3-zone furnace, with the temperatures of the first two zone set at 250 ^{o}C, and the third zone set at 860 ^{o}C. A gas mixture of Ar and H_2 was flowed at a rate of 1000 sccm and 300 sccm , respectively. A quartz plate was placed in the third zone for the growth of the sponges. After a growth of about 3 hours, the CNT sponge was detached from the quartz plate. Low-density sponge was obtained from the feeding rate of 6 ml/h.

For the Synthesis of large-diameter CNT sponge (or carbon nanofiber sponge), ferrocene powder was used as catalyst source and C_2H_4 gas was used as carbon source. The first two zone temperatures were set at 100 oC, and the third at 800 oC. 100 sccm Ar was passed through a water bubbler to add to a gas flow of 100 sccm C2H4, 200 sccm H2. 30 min. of growth was conducted and the carbon nanofibe sponge was collected from the wall of the 1" tube.

5.2.3 Electrochemistry

The semi-liquid Li-S batteries were assembled into a 2023-type coin cell. First, Li metal foil was wetted with the electrolyte, i.e. 1 M LiTFSI + 0.5 M $LiNO_3$ in DOL:DME (1:1 vol.). Then, Celgard 2400 was placed on the top as the separator. Subsequently, the CNT sponge with a thickness ~1 mm was stacked on top of separator and certain amount of catholyte was dropped to the CNT sponge. Catholyte with 2 M Li_2S_6 and 4 M Li_2S_6 was used, and loading volume of the catholyte with respect to the weight of CNT sponge (i.e. loading weight of the sulfur) was controlled to be 5 ul/mg, 7.5 ul/mg, 10 ul/mg and 15 ul/mg, respectively.

Arbin BT2000 was used for the galvanostatic charge/discharge of the coin cells. The Li-S batteries were cycled between 1.7 ~ 3 V at different rates (1 C=1600 mA/g) and the capacity were calculated based on the weight of S.

5.2.4 Structure characterization

X-ray diffraction (XRD) measurements were performed with a Bruker instrument (Bruker-AXS D8 VARIO) with Cu Kα radiation. The patterns were measured from 2θ = 15 to 75 degree with a step size of 0.01 ° and dwell time of 0.1s. Field-emission scanning electron microscope (SEM) and transmission electron microscope (TEM) were inspected with a JEOL JSM-7500F, and JEOL JEM-2010, respectively. For the CNT sponge at charged state, the sponge taken from the disassembled Li-S cell was washed with DOL and then dried for the SEM and TEM.

5.3 Results and discussions

5.3.1 Sponge Synthesis

Aligned carbon nanotubes (CNT) arrays or forests was the most commonly products when growth of CNT was conducted on the Si/SiO_2 wafer with a thin film of Al/Fe catalyst. A thickness up to 2 mm has been reported with the aid of moisture for a super growth.[139] But, this kind of CNT film is mechanically fragile and is not flexible. CNT sponge was first synthesized by Wu et al.[137] The randomly intertwined CNT surprisingly shows extremely high elasticity and flexibility.[138] The CNT sponge is highly porous and hydrophobic, making it ideal for oil absorption.

In this study, we found that the CNT sponge is also an ideal cathode substrate for the Li-S batteries, due to its high electronic conductivity and high porosity. Figure 5.2a shows a schematic illustration of the CNT sponge, showing the physically intertwined morphology. Figure 5.2b is the photo image of a CNT sponge cut into a square shape. With a gentle press by finger, the CNT sponge is elastic and can be recovered to its original shape after the removal of

the press. Figure 5.2c and d show the morphology of the large-diameter CNT sponge (or carbon nanofiber sponge). Because the Fe catalyst was delivered by the evaporation of the ferrocene powder, the Fe catalyst has large size, yielding a sponge with large-diameter carbon nanofibers. As shown in figure 5.2d, the diameter of the carbon nanofiber is about 150 nm (also see Figure 5.3a and b). Figure 5.2e and f show the morphology of the small-diamter CNT sponge. Comparing with the large-diamter carbon nanofiber, the diameter of the CNT is an order of magnitude smaller. Because the delivering of the Fe catalyst was controlled by a springe pump, the Fe particles decomposed from the ferocene is small, which produces the CNTs with small diameter. The correlation of the CNT diameter with the catalyst size has been demonstrated by previous work.[140] The diameter difference can be clearly seen from the TEM images of the sponges in figure 5.3. As can be seen from figure 5.3c and d, the diameter of small-diameter sponge is only about ~20 nm. Thereafter, the large-diameter sponge will be all referred as carbon nanofiber sponge (CNF sponge), and the small-diameter sponge will be described as carbon nanotubes sponge (CNT sponge).

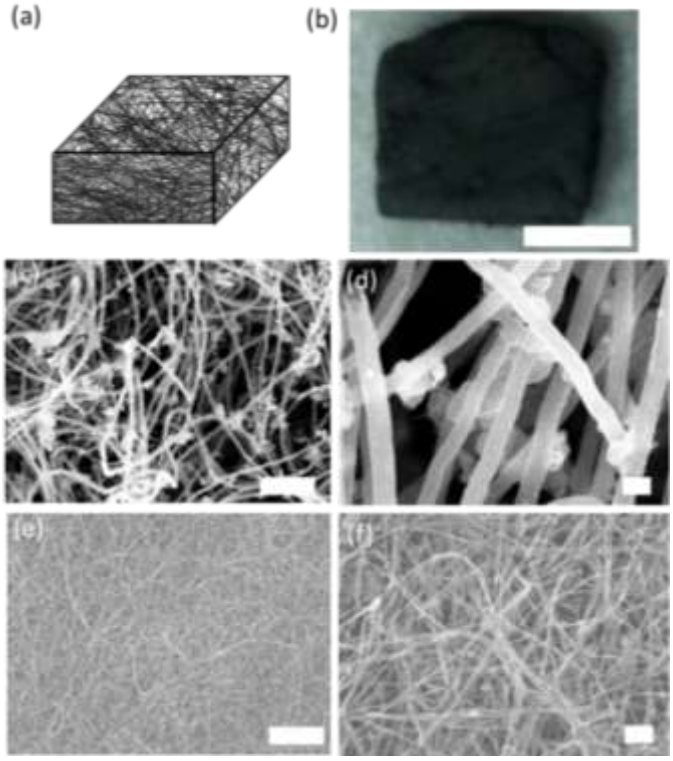

Figure 5.2 Synthesis of carbon nanofiber (CNF) sponge and carbon nanotube (CNT) sponge. (a) Schematic illustration of a CNT sponge. (b) Photo image of a CNT sponge. (c) and (d) SEM images of CNF sponge. (e) and (f) SEM images of CNT sponge. The scale bar is 0.5 inch for (a), 2 μm for (c) and (e), 200 nm for (d) and (f).

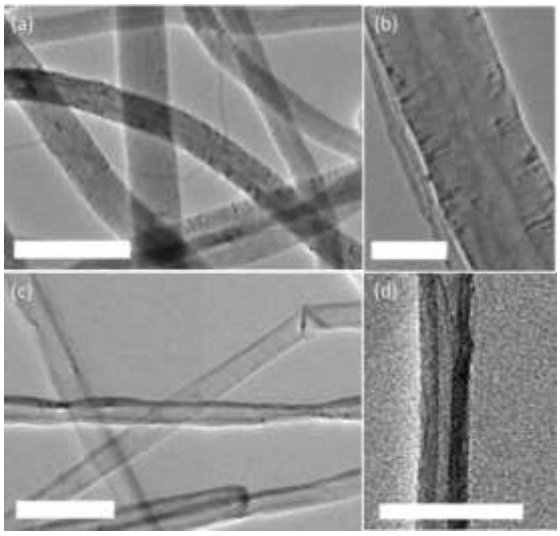

Figure 5.3 TEM images of CNF (a and b) and CNT (c and d) sponges. The scale bar is 500 nm for (a), 100 nm for (b) and (c), 50 nm for (d).

5.3.2 Li-S battery with CNF sponge as liquid catholyte reservoir

Figure 5.4 shows the cycling performances of Li-S batteries at 0.5 C rate between 3~1.7 V (vs. Li/Li^+) with CNF sponge as the reservoir of liquid catholyte. For 2 M Li_2S_6 in electrolyte (1 M LiTFSI + 0.5 M $LiNO_3$ in DOL:DME), the catholyte loading volume of 5 μL/mg and 10 μL/mg with respect to the weight of CNF sponge yield the S:CNF weight ratio of 1:3 and 2:3, respectively. If considering S/CNF sponge as a composite, the S weight percentage is 24 wt.% and 40 wt.%, respectively. In order to have the same S loading with 4 M Li_2S_6 in electrolyte, only 2.5 μL/mg and 5 μL/mg loading of the catholyte are required. Since CNF sponge was used as a binder-free substrate in this study, this S loading percentage is comparable with most of today's porous thin film electrode with solid sulfur mixed with porous carbon and polymer binder. Meanwhile, Al current collector was not used in this design, further raising the energy density of the total cell.

As shown in figure 5.4a and 5.5a, the first discharge capacity of 24 wt.% and 40 wt.% S loading with 2 M Li_2S_6 is 612 mAh/g and 320 mAh/g, respectively. Then, the discharge capacity increases to the maximum of 970 mAh/g at the 70^{th} cycle and 680 mAh/g at the 100^{th} cycle for 24 wt.% and 40 wt.% S, respectively. After 300 cycles, capacity of 852 mAh/g and 598 mAh/g can still be maintained for 24 wt.% and 40 wt.% S, respectively. When 4 M Li_2S_6 was used, even better performances can be achieved, as shown in figure 5.4b. The maximum capacity that can be achieved for 24 wt.% and 40 wt.% S loading is 1150 mAh/g at 130^{th} cycle and 1050 mAh/g at 110^{th} cycle, respectively. After 300 cycles, capacity can still be maintained at 982 mAh/g and 915 mAh/g for 24 wt.% and 40 wt.% S, respectively.

The variation trends of the discharge capacity for all the four tested cells are the same (see Figure 5.4). The first discharge is low, because the starting polysulfides is Li_2S_6 and the 2.3 V (vs. Li/Li^+) plateau will not show up, as shown in figure 5.5. Since the cells are cycled between

3~1.7 V, at the end of each following discharge and charge, the products are solid S and Li_2S, respectively. The capacity will increase and the 2.3 V (vs. Li/Li^+) plateau will show up in discharge after the first charge to 3 V, as can be seen by the second discharge profiles in figure 5.5. Because of the concentration polarization of the catholyte, the dissolved polysulfides are not fully utilized in the first several cycles and the capacity keeps increasing until the maximum discharge capacity is achieved when the dissolved polysulfides in catholyte are depleted during the charge.

Comparing with 2 M Li_2S_6, the 4M cells show better performances because of less volume of catholyte is required to have the same S loading. Larger volume of catholyte will increase diffusion length of dissolved polysulfides and raise the concentration polarization, therefore leading to smaller capacity and longer cycles to achieve the maximum. For 2 M Li_2S_6, discharge capacity drops dramatically when the loading volume is doubled from 5 μL/mg to 10 μL/mg; whereas, for 4 M Li_2S_6, only a slight decrease of the capacity is observed when the S loading is increased from 24 wt.% to 40 wt.% (volume loading increased from 2.5 μL/mg to 5 μL/mg). Another benefit of the high concentration polysulfides is its higher energy density due to the less weight of liquid electrolyte. To achieve same S loading, the inactive weight of the catholyte in 4 M Li_2S_6 cell is only about half of that in 2 M Li_2S_6 cell. Meanwhile, the kinetics of the concentrated 4 M catholyte did not decrease dramatically comparing with 2 M catholyte. As shown in figure 5.5, the second discharge plateau for 4 M catholyte is 2.07 V and 2.05 V (vs. Li/Li^+), slightly smaller than 2.09 V and 2.06 V (vs. Li/Li^+) of 2 M catholyte with 24 wt.% and 40 wt.% S, respectively. The only unfavorable characteristic is the larger viscosity of concentrated 4 M Li_2S_6 than 2 M Li_2S_6 catholyte, which lowers the diffusivity of the polysulfides and elongates the cycles before reaching the maximum capacity.

Excellent cyclability has been achieved for both 4 M and 2 M Li_2S_6 catholyte with CNF sponge as the catholyte reservoir. The microporous structure of the sponge allows easy accessibility of the each individual CNF for the catholyte. Even for relative viscous 4 M concentrated catholyte, easy absorption of the catholyte by the sponge was observed when assembling the cell. During the cycling, uniform Li_2S and elemental S solid coatings, rather than big particles, were electrochemically deposited on the surface of CNF at the end of discharge and charge, respectively. As shown in figure 5.6, the mircroporous structure of the CNF sponge was maintained and a layer of S was uniformly coated on the CNF after 300 cycles at charged state. The diameter of CNF is increased from ~150 nm to ~250 nm, and the EDS shows the major content of S, as shown in the inset of figure 5.6d. As described in other literature, the accumulation of irreversible aggregates in the electrode during the cycling contributes to the rapid degradation of the cyclability of the cell.[135] In this study, this problem was greatly alleviated and much better cyclability was achieved. The high reversibility of the cell is also indicated by the high columbic efficiencies of the cells. All the four tested cells shows columbic efficiency ~99% at the very beginning, and then slow decreases to ~95% after 300 cycles.

Meanwhile, the polysulfides shuttle was also significantly suppressed as indicated by the stable cycling performances. After reaching the maximum capacity, the capacity decreasing rate is about 0.05~0.08 %. This stable cyclability demonstrated that the CNF sponge is an excellent polysuflids reservoir, which reserves most of the polysulfides in electrolyte and prohibits the rapid shuttle of them from the cathode side to the Li metal anode side.

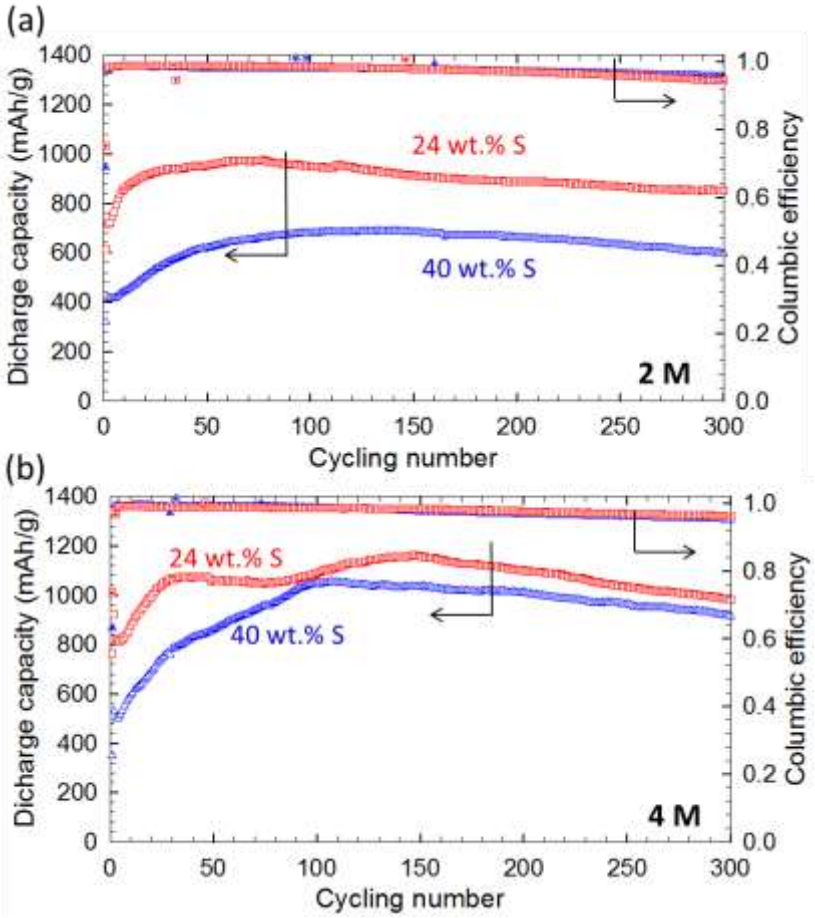

Figure 5.4 Cycling performances of Li-S batteries with CNF sponge as catholyte reservoir. (a) Cycling performances of CNF sponge loaded with 2 M Li_2S_6 in electrolyte (1 M LiTFSI + 0.5 M $LiNO_3$ in DOL:DME). The loading volume of catholyte with respect to the weight of CNF sponge is 5 μL/mg and 10 μL/mg, corresponding to S weight percentage of 24 wt.% and 40 wt.%, respectively. (b) Cycling performances of CNF sponge loaded with 4 M Li_2S_6 in electrolyte. Loading volume is 2.5 μL/mg and 5 μL/mg, corresponding to S weight percentage of 24 wt.% and 40 wt.%, respectively. All tests are conducted at 0.5 C rate.

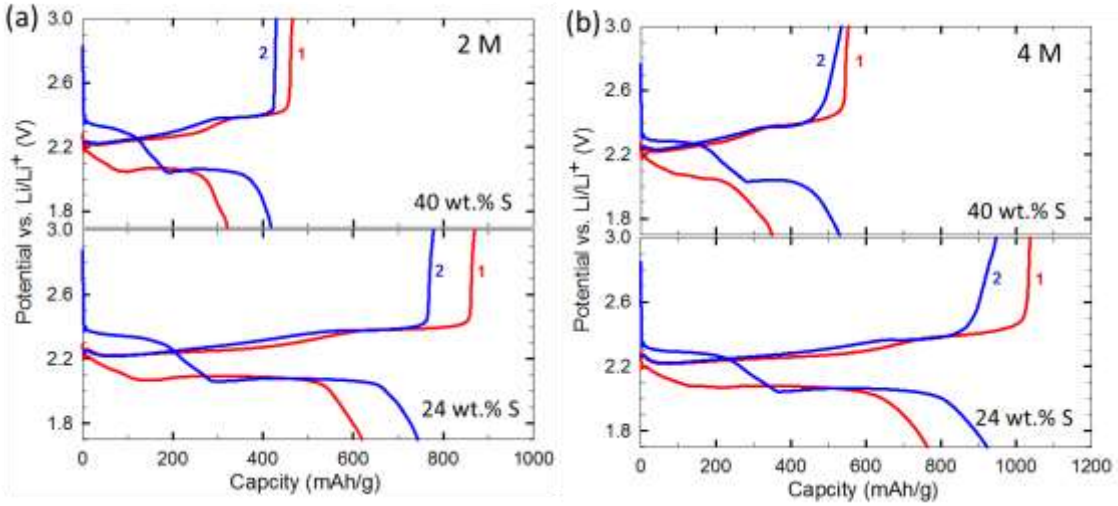

Figure 5.5 Charge/discharge profiles of the first two cycles of CNF sponge loaded with (a) 2 M Li_2S_6 and (b) 4 M Li_2S_6 in electrolyte. All tests are conducted at 0.5 C rate.

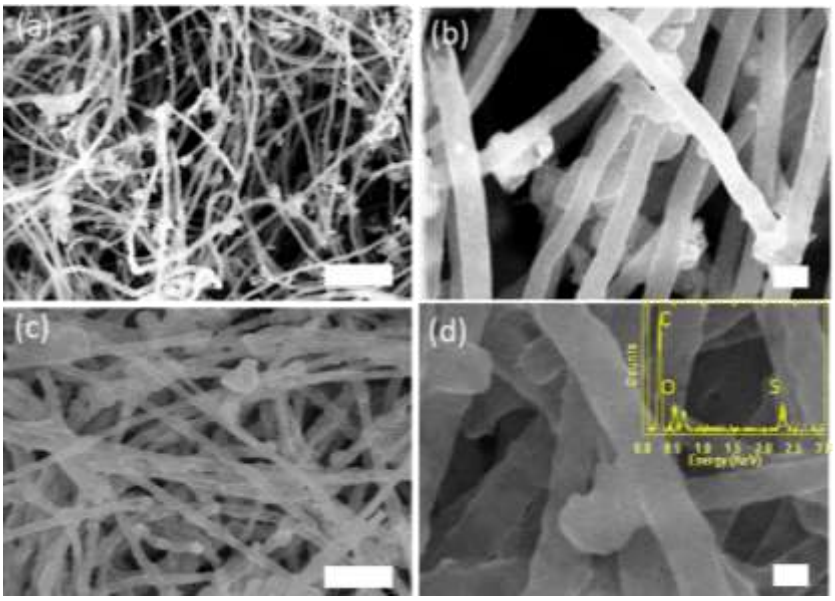

Figure 5.6 Comparison of SEM images of CNF before (a and b) and after 300 cycles at charged state (c and d). The scale bar is 2 μm for a and c, 200 nm for c and d.

5.3.3 Li-S battery with CNT sponge as liquid catholyte reservoir

Because of the smaller diameter and larger surface area, CNT sponge is expected to be better reservoir for catholyte in Li-S batteries. Four batteries were tested with CNT sponge as the cathode reservoir. Similar to the CNF sponge, both 2 M and 4 M Li_2S_6 in electrolyte (1 M LiTFSI + 0.5 M $LiNO_3$ in DOL:DME) were used as the catholyte. Two loading volumes of 7.5 and 10 μL/mg were adopted for both 2 M and 4 M Li_2S_6 catholyte. For 2 M catholyte, the S weight percentage would be 40 wt.% and 33 wt. % for 10 and 7.5 μL/mg loading volume, respectively; while for 4 M catholyte, the S weight percentage would be 56 wt.% and 50 wt.% for 10 and 7.5 μL/mg loading volume, respectively. Figure 5.7 shows the cycling performances of Li-S batteries with CNT sponge as the reservoir for liquid catholyte.

For the battery with 7.5 μL/mg loading of 2 M catholyte, the first and second discharge capacity at 0.5 C is 1052 and 1248 mAh/g, respectively. For 10 μL/mg loading of 2 M catholyte, the first and second discharge capacity decrease to 745 and 873 mAh/g, respectively. After 200 cycles, the capacity retained for the 7.5 and 10 μL/mg loading battery is 1044 and 771 mAh/g, respectively, corresponding to capacity retention of 83% and 88%, respectively. For 7.5 μL/mg loading of 4 M catholyte, the first and second discharge capacity at 0.5 C is 1028 mAh/g and 1224 mAh/g, respectively. For 10 μL/mg loading of 4 M catholyte, the first and second discharge capacity decrease to 657 and 767 mAh/g, respectively. After 200 cycles, the capacity retained for the 7.5 and 10 μL/mg loading battery is 1013 and 638 mAh/g, respectively, corresponding to capacity retention of 83% and 83%, respectively. It should be noted that S weight in 4 M batteries is doubled comparing to the 2 M batteries with same loading volume of catholyte. Unlike the large polarization shown in battery with CNF sponge, battery with CNT sponge does not show polarization. The columbic efficiencies of all the four batteries are ~1 throughout the cycling except the first cycle.

Comparing with CNF sponge, much larger volume of catholyte and higher amount of S can be loaded with CNT sponge, due to the larger surface area. Excellent capacity and cyclability can be achieved even when the sponge is loaded with 50 wt.% and 56 wt.% of S, leading to a much higher energy density of the total cell. Similar to the CNF sponge, larger loading can be achieved by 4 M catholyte. The reduced polarization in battery with CNT sponge during the cycling is attributed to the larger surface area and the better electric conductivity of the CNT.

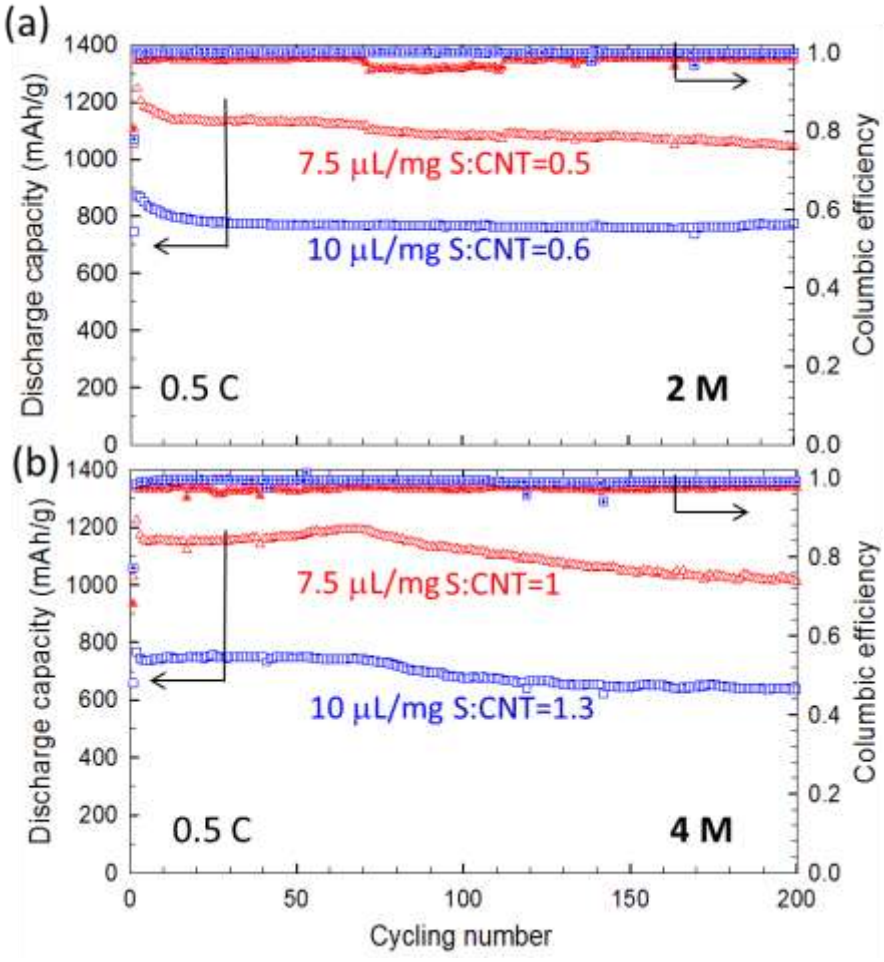

Figure 5.7 Cycling performances of Li-S batteries with CNT sponge as catholyte reservoir. 10 μL/mg and 7.5 μL/mg of 2 M and 4 M Li_2S_6 catholyte were loaded to the CNT sponge, respectively. All tests are conducted at 0.5 C.

5.3.4 Charge control

As suggested by Manthriam et al[92], a charge capacity-limited cycling strategy can significantly improve the cyclability of the Li-S battery. The strategy is to avoid the highly soluble high-order polysulfides (Li_2S_6 ~ Li_2S_8) during the charge/discharge by cutting off the charge at certain capacity so that the 2.3 V (vs. Li/Li^+) discharge plateau will not appear during the discharge. As the low-order polysulfides (Li_2S_4 ~ Li_2S_2) has low solubility in electrolyte, the polysulfides shuttle problem in Li-S battery can be dramatically suppressed.

In this study, a Li-S battery was assembled with 2 M Li_2S_6 in electrolyte (1 M LiTFSI + 1 wt.% $LiNO_3$ in DOL:DME) as the catholyte, CNF sponge as the polysulfides reservoir, and Li metal as the counter electrode. The loading volume of catholyte is 5 μL/mg, corresponding to a S weight percentage of 24 wt.%. As shown in figure 5.8, the first discharge capacity is 620 mAh/g. For the following cycles, the charge limit is set as the capacity of 640 mAh/g. For about 600 cycles, stable cycling performance was obtained without obvious decrease of the discharge capacity. The columbic efficiency also maintains at ~1 for 600 cycles. But, after 600 cycles, slow decrease of both capacity and columbic efficiency can be observed. As can be seen from the cut-off voltage of the cycling, the cut-off voltage keeps increasing slowly after about 100 cycles, which indicates that the polysulfides were oxidized to higher order cycle by cycle. In the last cycles, the increase of the cut-off voltage was accelerated. If the cycling is elongated, the cut-off voltage will reach 2.5 V or above, as all the polysulfides in the electrolyte are converted to elemental S. After that, rapid capacity fading will be expected. In summary, this strategy is efficient in improving the cyclability at the sacrifice of a portion of capacity, though the polysulfides problem is only delayed not eliminated.

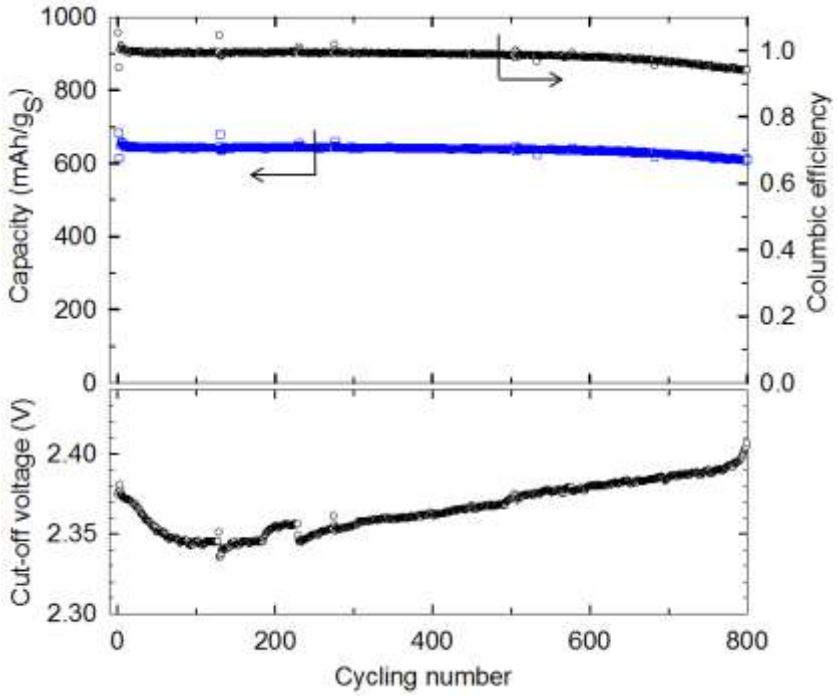

Figure 5.8 Cycling performances and corresponding cut-off voltage of a Li-S battery with charge limit of 640 mAh/g and discharge limit of 1.7 V (vs. Li/Li$^+$). CNF sponge loaded 5 μL/mg 2 M Li_2S_6 catholyte was used as cathode. The charge/discharge is conducted at 0.5 C rate.

5.3.5 Li_xSi-Li_2S_6 semi-liquid full cell

As discussed in Chapter IV, Li-S battery with Li metal anode has potential safety hazard, and the Li_xSi is the best candidate to replace the Li metal so as to eliminate this problem. Li_xSi-Li_2S_6 semi-liquid battery was studied in this Chapter. The same pre-lithiated C-mSi electrode as last Chapter was used as anode. The cathode was CNF sponge loaded with 2 M Li_2S_6 in electrolyte (1 M LiTFSI + 1 wt.% $LiNO_3$ in DOL:DME). Two batteries were assembled: (B-1) Si to S weight ratio is Si:S = 0.8, and 2 M Li_2S_6 catholyte loading in CNF sponge is 5 μL/mg; (B-2) Si:S weight ratio is 1.8, and 2 M Li_2S_6 catholyte loading in CNF sponge is 3 μL/mg. Both the two batteries are cathode-limited, and the capacity is calculated based on the weight of S.

As shown in figure 5.9, B-1 maintains a stable discharge capacity of ~700 mAh/g for about 60 cycles. After that, the cut-off voltage increases rapidly to 3 V, and the discharge capacity

drops quickly to 406 mAh/g at the 100th cycle. As for B-2, the discharge capacity maintains at ~800 mAh/g for 160 cycles. Subsequently, the cut-off voltage rises to 3 V, and the discharge capacity drops to 502 mAh/g at the 250th cycle. The columbic efficiencies of the two batteries are close to ~1 because of the adding of $LiNO_3$ in the electrolyte, but also show slight decrease when the cut-off voltage reaches 3 V. This cycling behavior of the full cell is similar to that of the half cell in figure 5.8, confirming that the charge control strategy can suppress but not eliminate the polysulfides shuttle problem.

Comparing with battery B-1, the higher capacity of B-2 is attributed to the smaller loading volume of 2 M Li_2S_6 catholyte. The longer stable cycling is due to both the lower S loading and the larger amount of Si in anode. As discussed in Chapter IV, the mechanical failure of Si anode and polysulfides shuttle of S cathode will be combined to continuously consuming the reversible Li sources in the cell, leading to a rapid capacity fading in the full cell. This is also the reason for the worse cycling performances of the Li_xSi-Li_2S_6 full cell than that of Li-Li_2S_6 half cell in figure. 5.8. Meanwhile, the porous thin film of pre-lithiated Li_xSi anode has larger surface area than Li metal, which can reduce more polysulfides shuttled to the anode side, and thus accelerate the polysulfides shuttle.

Figure 5.10 shows the charge/discharge voltage profiles of the battery B-1 and B-2. As for B-1, the charge of the first 50 cycles ends with similar cut-off voltage ~2.37 V; whereas, the charge cut-off voltage increases to 2.88 V at the 70th cycle, and 3 V at the 100th cycle. Before the voltage reaches 3 V, discharge capacity shows no obvious drop, as can be seen from the discharge capacities of the first 70th cycles. Similar behavior can be observed from the voltage profiles of battery B-2, which shows a transition from stable cycling to quick fading around 165th cycle. The first discharge for these two batteries shows no voltage plateau corresponding to the redox potential 2.3 V (vs. Li/Li^+) of S, as the starting materials used is Li_2S_6. But, with the

continuation of the cycling and increase of the cut-off charge voltage, a short slope between 2.2 V~2 V can be observed, which corresponds to the redox potential 2.3 V (vs. Li/Li^+) of S in half cell. This indicates that lithium polysulfides (Li_2S_x, x>6) were formed at the end of each charge, and during each cycle a portion of lithium polysulfides was lost due to the shuttle effect.

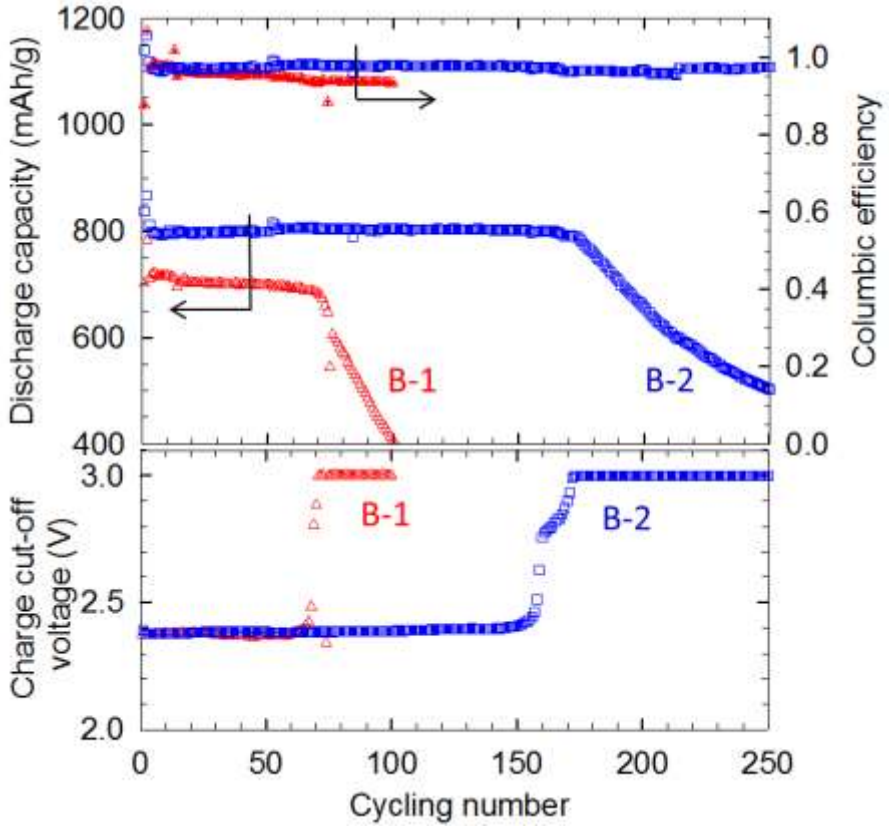

Figure 5.9 Cycling performances and corresponding cut-off voltages of two Li_xSi-Li_2S_6 batteries. The charge is limited by the first discharge capacity and 3 V; discharge limit is 1.3 V. (B-1) Si:S=0.8, 2 M Li_2S_6 loading is 5 μL/mg; (B-2) Si:S=1.8, 2 M Li_2S_6 loading is 3 μL/mg. The charge/discharge is at 0.5 C rate.

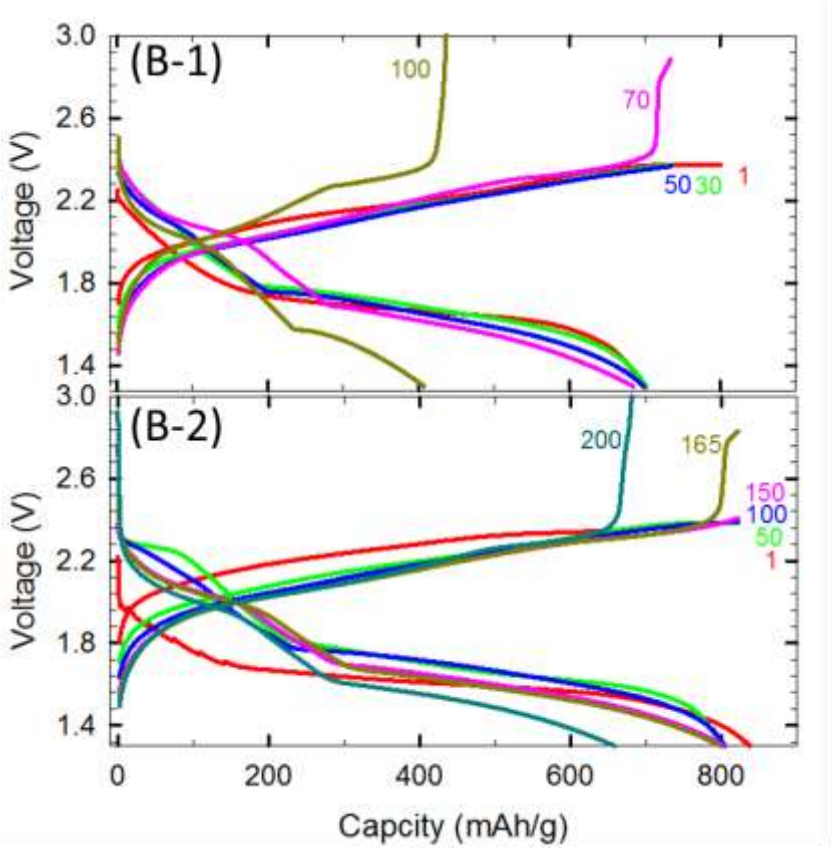

Figure 5.10 Voltage profiles of the two Li_xSi-Li_2S_6 batteries. The charge is limited by the first discharge capacity and 3 V; discharge limit is 1.3 V. (B-1) Si:S=0.8, 2 M Li_2S_6 loading is 5 μL/mg; (B-2) Si:S=1.8, 2 M Li_2S_6 loading is 3 μL/mg. The charge/discharge is at 0.5 C rate.

5.4 Conclusions

In summary, Carbon nanotubes (CNT) sponge and carbon nanofiber (CNF) sponge were synthesized with a CVD method. Highly porous structure with mechanical elasticity and flexibility was obtained. The diameter of CNT and CNF is ~20 nm and ~150 nm, respectively. Novel semi-liquid Li-S batteries were designed with polysufldies catholyte as the active materials in cathode. Catholyte of 2 M Li_2S_6 and 4 M Li_2S_6 dissolved in electrolyte was prepared by direct chemical reaction of S with Li_2S stoichiometrically. When the CNF sponge was used as the catholyte reservoir, excellent capacity and cyclabity can be achieved with S loading up to 40 wt.%. Stable cycling was achieved for 300 cycles at 0.5 C rate, with capacity fading ratio per

cycle as low as 0.05%~0.08%. When CNT sponge was used, excellent performances can be achieved with S loading up to 50 wt.% and 56 wt.%, due to the larger surface area and better conductivity of CNT. For both CNT and CNF sponges, 4 M Li_2S_6 catholyte showed higher capacity than that of 2 M catholoyte, since half of the volume of the catholyte was required to have same S loading weight.

Capacity-limiting charge strategy was adopted to suppress the polysulfids shuttle, and thus to improve the cyclability. The charge/discharge of the semi-liquid Li-S battery was tried be limited in the range of low-order polysufides (between Li_2S_6 ~ Li_2S). Stable cycling performances were achieved for 800 cycles, though for the last 200 cycles serious degrading of the cell can be observed by the increasing cut-off voltage.

Li_xS-Li_2S_6 semi-liquid full cell was studied for the purpose of elimination of safety hazard of the Li metal-containing battery. Prelithiated C-mSi electrode same as Chapter IV was used. Two batteries were tested with different Si:S weight ratio and different S loading weight in CNF sponge. Longer stable cycling was achieved at lower S loading and higher Si:S ratio, due to the less serious polysulfides shuttle problem and larger amount of Li source.

CHAPTER VI

SUMMARY

With the aim of developing batteries with higher energy density, lower price and better safety, this dissertation proposed several strategies to overcome the challenging problems in $LiCoO_2$-based Li-ion batteries and Li-S batteries. Even though $LiCoO_2$ has been commercialized for about two decades, there is still potential to further improve its energy density, because only half of its theoretical capacity is used in practice, due to the structure instability and side reactions upon complete delithiation. Meanwhile, the investigation on the overcharge issue in $LiCoO_2$ also can provide useful information to the recent study on high-capacity layered solid-solution cathode ($LiNi_xMn_yCo_{1-x-y}O_2$) and high-voltage spinel cathode ($LiMn_{1.5}Ni_{0.5}O_4$), since similar problems needed to be overcome, such as the side reactions, decomposition of electrolyte, and structure instability. Li-S batteries have much larger potential than Li-ion intercalation based Li-ion batteries in terms of high energy density and low prices. They are the most promising batteries that may power the electric vehicles with long-distance driving per charge. In this dissertation, both the performances of $LiCoO_2$ and Li-S batteries have been improved.

Surface modification with Li_3VO_4 is the strategy proposed in this dissertation to overcome the overcharge problem of $LiCoO_2$. Li_3VO_4 is believed to be an excellent Li-ion conductor, which will provide structure protection to prevent detrimental surface side reactions and will not slow down the diffusion of the Li ions. $LiCoO_2$ nanoparticles were synthesized by a hydrothermal method. A facile wet coating method followed by sintering was utilized with NH_4VO_3 and LiOH as starting materials. Our systematic studies revealed that the reaction between Li and vanadium oxides is favorable during the Synthesis, resulting in Co_3O_4 due to the removal of Li from $LiCoO_2$ when the molar ratio of total Li to V is smaller than 3:1 (i.e., Li is deficient). With additional LiOH for the sintering process, only Li_3VO_4 was obtained without

other byproducts while the structure and morphology of the $LiCoO_2$ nanoparticles were maintained. Great improvement in overcharge performances (overcharged to 4.5 and 4.7 V) was obtained by 3.4 and 5.5 wt.% Li_3VO_4 coating. For the electrodes with 5.5-wt.% Li_3VO_4-coated $LiCoO_2$, ~85 % of the first discharge capacity was retained after 100 galvanostatic cycles between 3 and 4.5 V at 30 mA/g (~0.2 C), compared with ~67 % of the electrode with the bare $LiCoO_2$ nanoparticles. At a current of 1200 mAh/g (~8 C) with cycling between 3 and 4.5 V, the electrode containing 5.5-wt.% coated $LiCoO_2$ still maintained 115 mAh/g discharge capacity, which is close to twice the capacity of the electrode with bare $LiCoO_2$ nanoparticles, indicating a greatly improved high-rate capability. TEM images showed more cracks and thicker SEI layer, which are the evidence for detrimental side reactions, from the bare $LiCoO_2$ compared to the coated $LiCoO_2$.

As for Li-S batteries, this dissertation first tried to address the issue of safety hazard due to the use of Li metal as anode. To avoid the sacrifice of energy density, Si was used as the anode to replace the Li metal, since it has a theoretical capacity (~4000 mAh/g) even larger than Li metal (3860 mAh/g). Both S and Si are very challenging due to their poor cyclability arising from the polysulfides shuttle problem of S and extremely large volume variation of Si, respectively. To overcome these issues, we utilized a mesoporous carbon as a conductive reservoir in cathode to suppress the polysulfides shuttle, and designed a prelithiated carbon-coated mesoporous Si in anode to accommodate the volume expansions. The lithium metal-free Li_xSi-S (LSS) full cell tested in this dissertation showed stable cycling with capacity retention of 80% over 100 cycles, which is by far the best cycling performances for LSS full cell with the organic electrolyte. The LSS full cell also showed excellent high-rate capability, delivering a discharge capacity of 465 mAh/g even at 3 C.

We demonstrated the better reliability and safety of the LSS battery than Li-S battery with the internal and external short-circuit experiments. LSS battery has no issue of Li dendrite formation; whereas, Li-S battery suffers from the rapid Li dendrite nucleation and growth at heterogeneous spot, which could result in the internal short-circuit and thermal runaway. The failure mechanism in Li-S battery was discussed based on the ex-situ observation of the Li surface by SEM images. The external short-circuit experiment also showed that Li-S battery, comparing with LSS battery, is more prone to fail. Anode-limiting design should be adopted for a battery countered with Li metal anode. We believe the demo of the LSS battery designed in this dissertation makes valuable contributions for the commercialization of sulfur battery in the near future.

This dissertation also found an effective way to improve the energy density and cycling life of the Li-S battery by using carbon nanotubes (CNT) sponge and carbon nanofiber (CNF) sponge as conductive reservoir of liquid-type cahtolyte. Catholyte containing dissolved polysulfides (2 M Li_2S_6 and 4 M Li_2S_6 dissolved in electrolyte) was used as active materials. The high weight percentage of S loading and the elimination of the use of Al current collector improved the energy density. Meanwhile, excellent cyclability was obtained due to the greatly suppressed polysulfides shuttle. Highly porous sponge with mechanical elasticity and flexibility was synthesized by CVD method. The diameter of CNT and CNF is ~20 nm and ~150 nm, respectively. When the CNF sponge was used as the catholyte reservoir, excellent capacity and cyclabity can be achieved with S loading up to 40 wt.%. Stable cycling was achieved for 300 cycles at 0.5 C rate, with capacity fading ratio per cycle as low as 0.05%~0.08%. When CNT sponge was used, excellent performances can be achieved with S loading up to 50 wt.%, due to the larger surface area and better conductivity of CNT. For both CNT and CNF sponges, 4 M Li_2S_6 catholyte showed higher capacity than that of 2 M catholoyte at the same loading weight of

S, since only half of the volume of the catholyte was required. Capacity-limiting charge strategy was adopted to suppress the polysulfids shuttle, and thus to improve the cyclability. The charge/discharge of the semi-liquid Li-S battery was tried be limited in the range of low-order polysufides (between Li_2S_6 ~ Li_2S). Stable cycling performances were achieved for 800 cycles, though for the last 200 cycles degrading of the cell can be observed by the increasing cut-off voltage. Li_xSi-S full cell with the semi-liquid configuration, using CNF sponge in cathode and prelithiated mesoporus Si in anode, also achieved stable cycing for about 200 cycles when charge control strategy is employed for the cycling.

REFERENCES

1. Winter, M.; Brodd, R. J., What are batteries, fuel cells, and supercapacitors? *Chem. Rev.* **2004,** *104* (10), 4245-4270.

2. Whittingham, M. S., Lithium batteries and cathode materials. *Chem. Rev.* **2004,** *104* (10), 4271-4302.

3. Besenhard, J. O., The electrochemical preparation and properties of ionic alkali metal- and NR4-graphite intercalation compounds in organic electrolytes. *Carbon* **1976,** *14* (2), 111-115.

4. Mizushima, K.; Jones, P. C.; Wiseman, P. J.; Goodenough, J. B., Li_xCoO_2 ($0<x<1$): a new cathode material for batteries of high energy density. *Mater. Res. Bull.* **1980,** *15* (6), 783-789.

5. Goodenough, J. B.; Kim, Y., Challenges for rechargeable Li batteries. *Chem. Mat.* **2009,** *22* (3), 587-603.

6. Ellis, B. L.; Lee, K. T.; Nazar, L. F., Positive electrode materials for Li-ion and Li-batteries. *Chem. Mat.* **2010,** *22* (3), 691-714.

7. Park, C. M.; Kim, J. H.; Kim, H.; Sohn, H. J., Li-alloy based anode materials for Li secondary batteries. *Chem. Soc. Rev.* **2010,** *39* (8), 3115-3141.

8. Cabana, J.; Monconduit, L.; Larcher, D.; Palacin, M. R., Beyond intercalation-based Li-ion batteries: the state of the art and challenges of electrode materials reacting through conversion reactions. *Adv. Mater.* **2010,** *22* (35), E170-E192.

9. Scott, I. D.; Jung, Y. S.; Cavanagh, A. S.; An, Y. F.; Dillon, A. C.; George, S. M.; Lee, S. H., Ultrathin coatings on nano-$LiCoO_2$ for Li-ion vehicular applications. *Nano Letters* **2011,** *11* (2), 414-418.

10. Ji, X. L.; Nazar, L. F., Advances in Li-S batteries. *J. Mater. Chem.* **2010,** *20* (44), 9821-9826.

11. Nagaura, T., *JEC Battery Newslett. No 2 (March-April 1991)*, 17-25.

12. Yoshio, M.; Brodd, R. J.; Kozawa, A., Lithium-ion batteries: science and technologies. **2009**, Springer Science NY.

13. Ohzuku, T.; Ueda, A., Solid-state redox reactions of $LiCoO_2$ ($R\bar{3}m$) for 4 volt secondary lithium cells. *J. Electrochem. Soc.* **1994,** *141* (11), 2972-2977.

14. Wang, H.; Jang, Y. I.; Huang, B.; Sadoway, D. R.; Chiang, Y. M., TEM study of electrochemical cycling-induced damage and disorder in $LiCoO_2$ cathodes for rechargeable lithium batteries. *J. Electrochem. Soc.* **1999,** *146* (2), 473-480.

15. Endo, E.; Yasuda, T.; Kita, A.; Yamaura, K.; Sekai, K., A $LiCoO_2$ cathode modified by plasma chemical vapor deposition for higher voltage performance. *J. Electrochem. Soc.* **2000,** *147* (4), 1291-1294.

16. (a) Kweon, H. J.; Park, D. G., Surface modification of $LiSr_{0.002}Ni_{0.9}Co_{0.1}O_2$ by overcoating with a magnesium oxide. *Electrochem Solid St* **2000,** *3* (3), 128-130; (b) Sun, Y. K.; Han, J. M.; Myung, S. T.; Lee, S. W.; Amine, K., Significant improvement of high voltage cycling behavior AlF_3-coated $LiCoO_2$ cathode. *Electrochem Commun* **2006,** *8* (5), 821-826.

17. Gao, Y. A.; Yakovleva, M. V.; Ebner, W. B., Novel $LiNi_{1-x}Ti_{x/2}Mg_{x/2}O_2$ compounds as cathode materials for safer lithium-ion batteries. *Electrochem Solid St* **1998,** *1* (3), 117-119.

18. (a) Rougier, A.; Gravereau, P.; Delmas, C., Optimization of the composition of the $Li_{1-z}Ni_{1+z}O_2$ electrode materials: structural, magnetic, and electrochemical studies. *J. Electrochem. Soc.* **1996,** *143* (4), 1168-1175; (b) Pouillerie, C.; Croguennec, L.; Biensan, P.; Willmann, P.; Delmas, C., Synthesis and characterization of new $LiNi_{1-y}Mg_yO_2$ positive electrode materials for lithium-ion batteries. *J. Electrochem. Soc.* **2000,** *147* (6), 2061-2069.

19. Mishra, S. K.; Ceder, G., Structural stability of lithium manganese oxides. *Phy. Rev. B* **1999,** *59* (9), 6120-6130.

20. Vitins, G.; West, K., Lithium intercalation into layered $LiMnO_2$. *J. Electrochem. Soc.* **1997,** *144* (8), 2587-2592.

21. (a) Park, B.-C.; Kim, H.-B.; Bang, H. J.; Prakash, J.; Sun, Y.-K., Improvement of electrochemical performance of $Li[Ni_{0.8}Co_{0.15}Al_{0.05}]O_2$ cathode materials by AlF_3 coating at various temperatures. *Industrial & Engineering Chemistry Research* **2008,** *47* (11), 3876-3882; (b) Rougier, A.; Saadoune, I.; Gravereau, P.; Willmann, P.; Delmasa, C., Effect of cobalt substitution on cationic distribution in $LiNi_{1-y}Co_yO_2$ electrode materials. *Solid State Ionics* **1996,** *90* (1–4), 83-90; (c) Belharouak, I.; Vissers, D.; Amine, K., Thermal Stability of the $Li(Ni_{0.8}Co_{0.15}Al_{0.05})O_2$ Cathode in the Presence of Cell Components. *J. Electrochem. Soc.* **2006,** *153* (11), A2030-A2035.

22. Naghash, A. R.; Lee, J. Y., Lithium nickel oxyfluoride ($Li_{1-z}Ni_{1+z}F_yO_{2-y}$) and lithium magnesium nickel oxide ($L_{1-z}(Mg_xNi_{1-x})_{1+z}O_2$) cathodes for lithium rechargeable batteries - II. Electrochemical investigations. *Electrochim. Acta* **2001,** *46* (15), 2293-2304.

23. (a) Rossen, E.; Jones, C. D. W.; Dahn, J. R., Structure and electrochemistry of $Li_xMn_yNi_{1-y}O_2$. *Solid State Ionics* **1992,** *57* (3–4), 311-318; (b) Lu, Z.; MacNeil, D. D.; Dahn, J. R., Layered cathode materials $Li[Ni_xLi_{1/3-2x/3}Mn_{2/3-x/3}]O_2$ for lithium-ion batteries. *Electrochemchemical and Solid-State Letters* **2001,** *4* (11), A191-A194.

24. (a) Lu, Z. H.; Beaulieu, L. Y.; Donaberger, R. A.; Thomas, C. L.; Dahn, J. R., Synthesis, structure, and electrochemical behavior of $LiNi_xLi_{1/3-2x/3}Mn_{2/3-x/3}O_2$. *J. Electrochem. Soc.* **2002,** *149* (6), A778-A791; (b) Lu, Z. H.; Dahn, J. R., Understanding the anomalous capacity of Li/Li $Ni_xLi_{1/3-2x/3}Mn_{2/3-x/3}O_2$ cells using in situ X-ray diffraction and electrochemical studies. *J. Electrochem. Soc.* **2002,** *149* (7), A815-A822.

25. Liu, J.; Manthiram, A., Functional surface modifications of a high capacity layered Li $Li_{0.2}Mn_{0.54}Ni_{0.13}Co_{0.13}O_2$ cathode. *J. Mater. Chem.* **2010,** *20* (19), 3961-3967.

26. (a) Thackeray, M. M.; David, W. I. F.; Bruce, P. G.; Goodenough, J. B., Lithium insertion into manganese spinels. *Mater. Res. Bull.* **1983,** *18* (4), 461-472; (b) Thackeray, M. M.; Johnson, P. J.; Depicciotto, L. A.; Bruce, P. G.; Goodenough, J. B., Electrochemical extraction of lithium from $LiMn_2O_4$. *Mater. Res. Bull.* **1984,** *19* (2), 179-187.

27. Wang, H.; Dai, H., Strongly coupled inorganic-nano-carbon hybrid materials for energy storage. *Chem. Soc. Rev.* **2013,** *42* (7), 3088-3113.

28. (a) Tarascon, J. M.; Coowar, F.; Amatuci, G.; Shokoohi, F. K.; Guyomard, D. G., The $Li_{1+x}Mn_2O_4$/C system materials and electrochemical aspects. *J Power Sources* **1995,** *54* (1), 103-108; (b) Blyr, A.; Sigala, C.; Amatucci, G.; Guyomard, D.; Chabre, Y.; Tarascon, J. M., Self-discharge of $LiMn_2O_4$/C Li-ion cells in their discharged state - Understanding by means of three-electrode measurements. *J Electrochem Soc* **1998,** *145* (1), 194-209.

29. Shin, Y. J.; Manthiram, A., Factors influencing the capacity fade of spinel lithium manganese oxides. *J Electrochem Soc* **2004,** *151* (2), A204-A208.

30. (a) Sigala, C.; Guyomard, D.; Verbaere, A.; Piffard, Y.; Tournoux, M., Positive Electrode materials with high operating voltage for lithium batteries: $LiCr_yMn_{2-y}O_4$ (0<=y<=1). *Solid State Ionics* **1995,** *81* (3-4), 167-170; (b) Amine, K.; Tukamoto, H.; Yasuda, H.; Fujita, Y., Preparation and electrochemical investigation of $LiMn_{2-x}Me_xO_4$ (Me: Ni, Fe, and x=0.5, 1) cathode materials for secondary lithium batteries. *J Power Sources* **1997,** *68* (2), 604-608; (c) Shigemura, H.; Sakaebe, H.; Kageyama, H.; Kobayashi, H.; West, A. R.; Kanno, R.; Morimoto, S.; Nasu, S.; Tabuchi, M., Structure and electrochemical properties of $LiFe_xMn_{2-x}O_4$ (0 <= x <= 0.5) spinel as 5 V electrode material for lithium batteries. *J Electrochem Soc* **2001,** *148* (7), A730-A736; (d) Shin, Y.; Manthiram, A., Origin of the high voltage (> 4.5 V) capacity of spinel lithium manganese oxides. *Electrochim Acta* **2003,** *48* (24), 3583-3592.

31. Padhi, A. K.; Nanjundaswamy, K. S.; Goodenough, J. B., Phospho-olivines as positive electrode materials for rechargeable lithium batteries. *J. Electrochem. Soc.* **1997,** *144* (4), 1188-1194.

32. (a) Chung, S. Y.; Bloking, J. T.; Chiang, Y. M., Electronically conductive phospho-olivines as lithium storage electrodes. *Nat. Mater.* **2002,** *1* (2), 123-128; (b) Ellis, B.; Kan, W. H.; Makahnouk, W. R. M.; Nazar, L. F., Synthesis of nanocrystals and morphology control of hydrothermally prepared $LiFePO_4$. *J Mater Chem* **2007,** *17* (30), 3248-3254.

33. Hu, Y. S.; Guo, Y. G.; Dominko, R.; Gaberscek, M.; Jamnik, J.; Maier, J., Improved electrode performance of porous $LiFePO_4$ using RuO_2 as an oxidic nanoscale interconnect. *Adv. Mater.* **2007,** *19* (15), 1963.

34. Delacourt, C.; Poizot, P.; Levasseur, S.; Masquelier, C., Size effects on carbon-free $LiFePO_4$ powders: the key to superior energy density. *Electrochemical and Solid-State Letters* **2006,** *9* (7), A352-A355.

35. Saravanan, K.; Reddy, M. V.; Balaya, P.; Gong, H.; Chowdari, B. V. R.; Vittal, J. J., Storage performance of $LiFePO_4$ nanoplates. *J Mater Chem* **2009,** *19* (5), 605-610.

36. (a) Padhi, A. K.; Nanjundaswamy, K. S.; Goodenough, J. B., Phospho-olivines as positive-electrode materials for rechargeable lithium batteries. *J Electrochem Soc* **1997,** *144* (4), 1188-1194; (b) Yang, J. S.; Xu, J. J., Synthesis and characterization of carbon-coated lithium transition metal phosphates $LiMPO_4$ (M = Fe, Mn, Co, Ni) prepared via a nonaqueous sol-gel route. *J Electrochem Soc* **2006,** *153* (4), A716-A723.

37. Aurbach, D.; Ein‐Eli, Y.; Chusid , O.; Carmeli, Y.; Babai, M.; Yamin, H., The correlation between the surface chemistry and the performance of Li-carbon intercalation anodes for rechargeable "rocking-chair" type batteries. *J. Electrochem. Soc.* **1994,** *141* (3), 603-611.

38. Besenhard, J. O.; Wagner, M. W.; Winter, N.; Jannakoudakis, A. D.; Jannakoudakis, P. D.; Theodoridou, E., Inorganic film-forming electrolyte additives improving the cycling behavior of metallic lithium electrodes and the self-discharge of carbon-lithium electrodes. *J. Power Sources* **1993,** *44* (1 -3 pt 2), 413-420.

39. Aurbach, D.; Gnanaraj, J. S.; Geissler, W.; Schmidt, M., Vinylene carbonate and Li salicylatoborate as additives in $LiPF_3(CF_2CF_3)_3$ solutions for rechargeable Li-ion batteries. *J. Electrochem. Soc.* **2004,** *151* (1), A23-A30.

40. Maurin, G. a. H., F., *Encylopedia of Nanoscience and Nanotehnology* **2003**, P. X/1.

41. Leroux, F.; Metenier, K.; Gautier, S.; Frackowiak, E.; Bonnamy, S.; Beguin, F., Electrochemical insertion of lithium in catalytic multi-walled carbon nanotubes. *J. Power Sources* **1999,** *81*, 317-322.

42. Yoo, E.; Kim, J.; Hosono, E.; Zhou, H.; Kudo, T.; Honma, I., Large reversible Li storage of graphene nanosheet families for use in rechargeable lithium ion batteries. *Nano Letters* **2008,** *8* (8), 2277-2282.

43. Liu, X.; Hu, Y. S.; Muller, J. O.; Schlogl, R.; Maier, J.; Su, D. S., Composites of molecular-anchored graphene and nanotubes with multitubular structure: a new type of carbon electrode. *Chemsuschem* **2010,** *3* (2), 261-265.

44. Lian, P. C.; Zhu, X. F.; Liang, S. Z.; Li, Z.; Yang, W. S.; Wang, H. H., Large reversible capacity of high quality graphene sheets as an anode material for lithium-ion batteries. *Electrochim. Acta* **2010,** *55* (12), 3909-3914.

45. Chan, C. K.; Peng, H.; Liu, G.; McIlwrath, K.; Zhang, X. F.; Huggins, R. A.; Cui, Y., High-performance lithium battery anodes using silicon nanowires. *Nat Nano* **2008,** *3* (1), 31-35.

46. (a) Park, M.-H.; Kim, M. G.; Joo, J.; Kim, K.; Kim, J.; Ahn, S.; Cui, Y.; Cho, J., Silicon nanotube battery anodes. *Nano Letters* **2009,** *9* (11), 3844-3847; (b) Wu, H.; Chan, G.; Choi, J. W.; Ryu, I.; Yao, Y.; McDowell, M. T.; Lee, S. W.; Jackson, A.; Yang, Y.; Hu, L.; Cui, Y., Stable cycling of double-walled silicon nanotube battery anodes through solid-electrolyte interphase control. *Nat Nano* **2012,** *7* (5), 310-315.

47. Ge, M.; Rong, J.; Fang, X.; Zhou, C., Porous doped silicon nanowires for lithium ion battery anode with long cycle life. *Nano Letters* **2012,** *12* (5), 2318-2323.

48. Wu, H.; Yu, G.; Pan, L.; Liu, N.; McDowell, M. T.; Bao, Z.; Cui, Y., Stable Li-ion battery anodes by in-situ polymerization of conducting hydrogel to conformally coat silicon nanoparticles. *Nat Commun* **2013,** *4*.

49. Kennedy, T.; Mullane, E.; Geaney, H.; Osiak, M.; O'Dwyer, C.; Ryan, K. M., High-performance germanium nanowire-based lithium-ion battery anodes extending over 1000 cycles through in situ formation of a continuous porous network. *Nano Letters* **2014,** *14* (2), 716-723.

50. Qin, J.; He, C.; Zhao, N.; Wang, Z.; Shi, C.; Liu, E.-Z.; Li, J., Graphene networks anchored with Sn@Graphene as lithium ion battery anode. *ACS Nano* **2014,** *8* (2), 1728-1738.

51. Morita, M.; Ishikawa, M.; Matsuda, Y., Organic electrolytes for rechargeable lithium ion batteries. In *Lithium Ion Batteries*, Wiley-VCH Verlag GmbH: 2007; pp 156-180.

52. Kamaya, N.; Homma, K.; Yamakawa, Y.; Hirayama, M.; Kanno, R.; Yonemura, M.; Kamiyama, T.; Kato, Y.; Hama, S.; Kawamoto, K.; Mitsui, A., A lithium superionic conductor. *Nat Mater* **2011,** *10* (9), 682-686.

53. Scrosati, B.; Vincent, C. A., Polymer Electrolytes: The key to lithium polymer batteries. *MRS Bulletin* **2000,** *25* (03), 28-30.

54. Croce, F.; Appetecchi, G. B.; Persi, L.; Scrosati, B., Nanocomposite polymer electrolytes for lithium batteries. *Nature* **1998,** *394* (6692), 456-458.

55. (a) Appetecchi, G. B.; Croce, F.; Romagnoli, P.; Scrosati, B.; Heider, U.; Oesten, R., High-performance gel-type lithium electrolyte membranes. *Electrochem. Commun.* **1999,** *1* (2), 83-86; (b) Persi, L.; Croce, F.; Scrosati, B., A $LiTi_2O_4$–$LiFePO_4$ novel lithium-ion polymer battery. *Electrochem. Commun.* **2002,** *4* (1), 92-95.

56. Takada, K., Progress and prospective of solid-state lithium batteries. *Acta Materialia* **2013,** *61* (3), 759-770.

57. Kanehori, K.; Matsumoto, K.; Miyauchi, K.; Kudo, T., Thin film solid electrolyte and its application to secondary lithium cell. *Solid State Ionics* **1983,** *9–10, Part 2* (0), 1445-1448.

58. Aono, H.; Sugimoto, E.; Sadaoka, Y.; Imanaka, N.; Adachi, G. y., Ionic conductivity of the lithium titanium phosphate $Li_{1+x}M_xTi_{2-x}(PO4)_3$, (M = Al, Sc, Y, and La) systems. *J. Electrochem. Soc.* **1989,** *136* (2), 590-591.

59. Inaguma, Y.; Liquan, C.; Itoh, M.; Nakamura, T.; Uchida, T.; Ikuta, H.; Wakihara, M., High ionic conductivity in lithium lanthanum titanate. *Solid State Communications* **1993,** *86* (10), 689-693.

60. Mizuno, F.; Hayashi, A.; Tadanaga, K.; Tatsumisago, M., New, Highly ion-conductive crystals precipitated from Li_2S–P_2S_5 glasses. *Adv. Mater.* **2005,** *17* (7), 918-921.

61. Kanno, R.; Murayama , M., Lithium Ionic Conductor Thio-LISICON: The Li_2S -GeS_2 -P_2S_5 System. *J. Electrochem. Soc.* **2001,** *148* (7), A742-A746.

62. Bruce, P. G.; Freunberger, S. A.; Hardwick, L. J.; Tarascon, J.-M., Li-O_2 and Li-S batteries with high energy storage. *Nat Mater* **2012,** *11* (1), 19-29.

63. Bruce, P. G.; Freunberger, S. A.; Hardwick, L. J.; Tarascon, J. M., Li-O_2 and Li-S batteries with high energy storage. *Nat. Mater.* **2012,** *11* (1), 19-29.

64. (a) Yamin, H.; Peled, E., Electrochmistry of a non-aqueous lithium sulfur cell. *J. Power Sources* **1983,** *9* (3-4), 281-287; (b) Kumaresan, K.; Mikhaylik, Y.; White, R. E., A mathematical model for a lithium-sulfur cell. *Journal of the Electrochemical Society* **2008,** *155* (8), A576-A582.

65. Yamin, H.; Penciner, J.; Gorenshtain, A.; Elam, M.; Peled, E., The electrochemical behavior of polysulfides in tetrahydrofuran. *J. Power Sources* **1985,** *14* (1-3), 129-134.

66. Rao, M. L. B., U.S. Patent. **1968,** *413* , (3), 154.

67. Rauh, R. D.; Shuker, F. S.; Marston, J. M.; Brummer, S. B., Formation of lithium polysulfides in aprotic media. *Journal of Inorganic & Nuclear Chemistry* **1977,** *39* (10), 1761-1766.

68. (a) Cheon, S. E.; Ko, K. S.; Cho, J. H.; Kim, S. W.; Chin, E. Y.; Kim, H. T., Rechargeable lithium sulfur battery - II. Rate capability and cycle characteristics. *Journal of the Electrochemical Society* **2003,** *150* (6), A800-A805; (b) Hassoun, J.; Sun, Y. K.; Scrosati, B., Rechargeable lithium sulfide electrode for a polymer tin/sulfur lithium-ion battery. *J. Power Sources* **2011,** *196* (1), 343-348.

69. Mikhaylik, Y. V.; Akridge, J. R., Polysulfide shuttle study in the Li/S battery system. *Journal of the Electrochemical Society* **2004,** *151* (11), A1969-A1976.

70. Zheng, W.; Liu, Y. W.; Hu, X. G.; Zhang, C. F., Novel nanosized adsorbing sulfur composite cathode materials for the advanced secondary lithium batteries. *Electrochim. Acta* **2006,** *51* (7), 1330-1335.

71. Wang, Y.-X.; Huang, L.; Sun, L.-C.; Xie, S.-Y.; Xu, G.-L.; Chen, S.-R.; Xu, Y.-F.; Li, J.-T.; Chou, S.-L.; Dou, S.-X.; Sun, S.-G., Facile Synthesis of a interleaved expanded graphite-embedded sulphur nanocomposite as cathode of Li-S batteries with excellent lithium storage performance. *Journal of Materials Chemistry* **2012,** *22* (11), 4744-4750.

72. Rao, M.; Song, X.; Cairns, E. J., Nano-carbon/sulfur composite cathode materials with carbon nanofiber as electrical conductor for advanced secondary lithium/sulfur cells. *J. Power Sources* **2012,** *205* (0), 474-478.

73. Xiao, L.; Cao, Y.; Xiao, J.; Schwenzer, B.; Engelhard, M. H.; Saraf, L. V.; Nie, Z.; Exarhos, G. J.; Liu, J., A soft approach to encapsulate sulfur: polyaniline nanotubes for lithium-sulfur batteries with long cycle life. *Adv. Mater.* **2012,** *24* (9), 1176-1181.

74. Schuster, J.; He, G.; Mandlmeier, B.; Yim, T.; Lee, K. T.; Bein, T.; Nazar, L. F., Spherical ordered mesoporous carbon nanoparticles with high porosity for lithium-sulfur batteries. *Angewandte Chemie International Edition* **2012,** *51* (15), 3591-3595.

75. Ji, X.; Lee, K. T.; Nazar, L. F., A highly ordered nanostructured carbon-sulphur cathode for lithium-sulphur batteries. *Nat Mater* **2009,** *8* (6), 500-506.

76. Li, W.; Zheng, G.; Yang, Y.; Seh, Z. W.; Liu, N.; Cui, Y., High-performance hollow sulfur nanostructured battery cathode through a scalable, room temperature, one-step, bottom-up approach. *Proceedings of the National Academy of Sciences* **2013**.

77. Wei Seh, Z.; Li, W.; Cha, J. J.; Zheng, G.; Yang, Y.; McDowell, M. T.; Hsu, P.-C.; Cui, Y., Sulphur–TiO_2 yolk–shell nanoarchitecture with internal void space for long-cycle lithium–sulphur batteries. *Nat Commun* **2013,** *4*, 1331.

78. Seh, Z. W.; Zhang, Q.; Li, W.; Zheng, G.; Yao, H.; Cui, Y., Stable cycling of lithium sulfide cathodes through strong affinity with a bifunctional binder. *Chemical Science* **2013,** *4* (9), 3673-3677.

79. Song, M.-K.; Zhang, Y.; Cairns, E. J., A long-life, High-rate lithium/sulfur cell: a multifaceted approach to enhancing cell performance. *Nano Letters* **2013,** *13* (12), 5891-5899.

80. Ji, X.; Lee, K.; Nazar, L., A highly ordered nanostructured carbon-sulphur cathode for lithium-sulphur batteries. *Nat. Mater.* **2009,** *8* (6), 500-6.

81. Lin, Z.; Liu, Z.; Fu, W.; Dudney, N. J.; Liang, C., Phosphorous pentasulfide as a novel additive for high-performance lithium-sulfur batteries. *Adv. Funct. Mater.* **2013,** *23* (8), 1064-1069.

82. Zhang, S. S., Role of $LiNO_3$ in rechargeable lithium/sulfur battery. *Electrochim. Acta* **2012,** *70* (0), 344-348.

83. Suo, L.; Hu, Y.-S.; Li, H.; Armand, M.; Chen, L., A new class of Solvent-in-Salt electrolyte for high-energy rechargeable metallic lithium batteries. *Nat Commun* **2013,** *4*, 1481.

84. Agostini, M.; Aihara, Y.; Yamada, T.; Scrosati, B.; Hassoun, J., A lithium–sulfur battery using a solid, glass-type P_2S_5–Li_2S electrolyte. *Solid State Ionics* **2013,** *244* (0), 48-51.

85. Kobayashi, T.; Imade, Y.; Shishihara, D.; Homma, K.; Nagao, M.; Watanabe, R.; Yokoi, T.; Yamada, A.; Kanno, R.; Tatsumi, T., All solid-state battery with sulfur electrode and thio-LISICON electrolyte. *J. Power Sources* **2008,** *182* (2), 621-625.

86. (a) Lin, Z.; Liu, Z.; Dudney, N. J.; Liang, C., Lithium superionic sulfide cathode for all-solid lithium-sulfur batteries. *ACS Nano* **2013,** *7* (3), 2829-2833; (b) Liu, Z.; Fu, W.; Payzant, E. A.; Yu, X.; Wu, Z.; Dudney, N. J.; Kiggans, J.; Hong, K.; Rondinone, A. J.; Liang, C., Anomalous high ionic conductivity of nanoporous β-Li_3PS_4. *J. Am. Chem. Soc.* **2013,** *135* (3), 975-978.

87. Yang, Y.; Yu, G.; Cha, J. J.; Wu, H.; Vosgueritchian, M.; Yao, Y.; Bao, Z.; Cui, Y., Improving the performance of lithium-sulfur batteries by conductive polymer coating. *ACS Nano* **2011,** *5* (11), 9187-9193.

88. Lu, S.; Cheng, Y.; Wu, X.; Liu, J., Significantly improved long-cycle stability in high-rate Li–S batteries enabled by coaxial graphene wrapping over sulfur-coated carbon nanofibers. *Nano Letters* **2013,** *13* (6), 2485-2489.

89. Rong, J.; Ge, M.; Fang, X.; Zhou, C., Solution ionic strength engineering as a generic strategy to coat graphene oxide (GO) on various functional particles and its application in high-performance lithium–sulfur (Li–S) batteries. *Nano Letters* **2013,** *14* (2), 473-479.

90. Moon, S.; Jung, Y. H.; Jung, W. K.; Jung, D. S.; Choi, J. W.; Kim, D. K., Encapsulated monoclinic sulfur for stable cycling of Li–S rechargeable batteries. *Adv. Mater.* **2013,** *25* (45), 6547-6553.

91. Xin, S.; Gu, L.; Zhao, N.-H.; Yin, Y.-X.; Zhou, L.-J.; Guo, Y.-G.; Wan, L.-J., Smaller sulfur molecules promise better lithium–sulfur batteries. *J. Am. Chem. Soc.* **2012,** *134* (45), 18510-18513.

92. Su, Y.-S.; Fu, Y.; Cochell, T.; Manthiram, A., A strategic approach to recharging lithium-sulphur batteries for long cycle life. *Nat Commun* **2013,** *4*.

93. Zoski, C., *Handbook of Electrochemistry*. 1st ed.; Elsevier: Amsterdam, 2007; p 432.

94. Jo, M.; Hong, Y. S.; Choo, J.; Cho, J., Effect of $LiCoO_2$ cathode nanoparticle size on high rate performance for Li-ion batteries. *J. Electrochem. Soc.* **2009,** *156* (6), A430-A434.

95. Kawamura, T.; Makidera, M.; Okada, S.; Koga, K.; Miura, N.; Yamaki, J., Effect of nano-size $LiCoO_2$ cathode powders on Li-ion cells. *J. Power Sources* **2005,** *146* (1-2), 27-32.

96. Okubo, M.; Hosono, E.; Kim, J.; Enomoto, M.; Kojima, N.; Kudo, T.; Zhou, H. S.; Honma, I., Nanosize effect on high-rate Li-ion intercalation in $LiCoO_2$ electrode. *J. Am. Chem. Soc.* **2007,** *129* (23), 7444-7452.

97. (a) Amatucci, G. G.; Tarascon, J. M.; Klein, L. C., Cobalt dissolution in $LiCoO_2$-based non-aqueous rechargeable batteries. *Solid State Ionics* **1996,** *83* (1-2), 167-173; (b) Aurbach, D., Review of selected electrode-solution interactions which determine the performance of Li and Li ion batteries. *J. Power Sources* **2000,** *89* (2), 206-218.

98. (a) Ohzuku, T.; Ueda, A., Solid-state redox reactions of $LiCoO_2$ (R^{3m}) for 4 volt secondary lithium cells. *J. Electrochem. Soc.* **1994,** *141* (11), 2972-2977; (b) Wang, H.; Jang, Y.-I.; Huang, B.; Sadoway, D. R.; Chiang, Y.-M., TEM study of electrochemical cycling-induced damage and disorder in $LiCoO_2$ cathodes for rechargeable lithium batteries. *J. Electrochem. Soc.* **1999,** *146* (2), 473-480.

99. (a) Liu, L.; Chen, L.; Huang, X.; Yang, X.-Q.; Yoon, W.-S.; Lee, H. S.; McBreen, J., Electrochemical and in situ synchrotron XRD studies on Al_2O_3-coated $LiCoO_2$ cathode material.

J. Electrochem. Soc. **2004,** *151* (9), A1344-A1351; (b) Cho, J.; Kim, C. S.; Yoo, S. I., Improvement of structural stability of $LiCoO_2$ cathode during electrochemical cycling by sol-gel coating of SnO_2. *Electrochem. Solid State Lett.* **2000,** *3* (8), 362-365; (c) Mladenov, M.; Stoyanova, R.; Zhecheva, E.; Vassilev, S., Effect of Mg doping and MgO-surface modification on the cycling stability of $LiCoO_2$ electrodes. *Electrochem. Commun.* **2001,** *3* (8), 410-416; (d) Chen, Z. H.; Dahn, J. R., Effect of a ZrO_2 coating on the structure and electrochemistry of Li_xCoO_2 when cycled to 4.5 V. *Electrochem. Solid State Lett.* **2002,** *5* (10), A213-A216; (e) Kim, Y. J.; Cho, J. P.; Kim, T. J.; Park, B., Suppression of cobalt dissolution from the $LiCoO_2$ cathodes with various metal-oxide coatings. *J. Electrochem. Soc.* **2003,** *150* (12), A1723-A1725; (f) Kannan, A. M.; Rabenberg, L.; Manthiram, A., High capacity surface-modified $LiCoO_2$ cathodes for lithium-ion batteries. *Electrochem. Solid State Lett.* **2003,** *6* (1), A16-A18.

100. (a) Kim, J.; Noh, M.; Cho, J.; Kim, H.; Kim, K.-B., Controlled nanoparticle metal phosphates (Metal = Al, Fe, Ce, and Sr) coatings on $LiCoO_2$ cathode materials. *J. Electrochem. Soc.* **2005,** *152* (6), A1142-A1148; (b) Lee, J.-G.; Kim, B.; Cho, J.; Kim, Y.-W.; Park, B., Effect of $AlPO_4$-nanoparticle coating concentration on high-cutoff-voltage electrochemical performances in $LiCoO_2$. *J. Electrochem. Soc.* **2004,** *151* (6), A801-A805; (c) Li, G.; Yang, Z. X.; Yang, W. S., Effect of $FePO_4$ coating on electrochemical and safety performance of $LiCoO_2$ as cathode material for Li-ion batteries. *J Power Sources* **2008,** *183* (2), 741-748.

101. (a) Fu, L. J.; Liu, H.; Li, C.; Wu, Y. P.; Rahm, E.; Holze, R.; Wu, H. Q., Surface modifications of electrode materials for lithium ion batteries. *Solid State Sci.* **2006,** *8* (2), 113-128; (b) Du, Q. L.; Zheng, M. B.; Zhang, L. F.; Wang, Y. W.; Chen, J. H.; Xue, L. P.; Dai, W. J.; Ji, G. B.; Cao, J. M., Preparation of functionalized graphene sheets by a low-temperature thermal exfoliation approach and their electrochemical supercapacitive behaviors. *Electrochim. Acta* **2010,** *55* (12), 3897-3903.

102. Wang, H.; Zhang, W. D.; Zhu, L. Y.; Chen, M. C., Effect of $LiFePO_4$ coating on electrochemical performance of $LiCoO_2$ at high temperature. *Solid State Ion.* **2007,** *178* (1-2), 131-136.

103. Yi, T. F.; Shu, J.; Yue, C. B.; Zhu, X. D.; Zhou, A. N.; Zhu, Y. R.; Zhu, R. S., Enhanced cycling stability of microsized $LiCoO_2$ cathode by $Li_4Ti_5O_{12}$ coating for lithium ion battery. *Mater. Res. Bull.* **2010,** *45* (4), 456-459.

104. Sun, K.; Dillon, S. J., A mechanism for the improved rate capability of cathodes by lithium phosphate surficial films. *Electrochem. Commun.* **2011,** *13* (2), 200-202.

105. Kang, B.; Ceder, G., Battery materials for ultrafast charging and discharging. *Nature* **2009,** *458* (7235), 190-193.

106. Kobayashi, Y.; Miyashiro, H.; Takei, K.; Shigemura, H.; Tabuchi, M.; Kageyama, H.; Iwahori, T., 5 V class all-solid-state composite lithium battery with Li_3PO_4 coated $LiNi_{0.5}Mn_{1.5}O_4$. *J. Electrochem. Soc.* **2003,** *150* (12), A1577-A1582.

107. Song, H. G.; Kim, J. Y.; Kim, K. T.; Park, Y. J., Enhanced electrochemical properties of $Li(Ni_{0.4}Co_{0.3}Mn_{0.3})O_2$ cathode by surface modification using Li_3PO_4-based materials. *J. Power Sources* **2011,** *196* (16), 6847-6855.

108. Kawamura, J.; Kuwata, N.; Toribami, K.; Sata, N.; Kamishima, O.; Hattori, T., Preparation of amorphous lithium ion conductor thin films by pulsed laser deposition. *Solid State Ion.* **2004,** *175* (1-4), 273-276.

109. Lee, J. W.; Park, S. M.; Kim, H. J., Enhanced cycleability of $LiCoO_2$ coated with vanadium oxides. *J Power Sources* **2009,** *188* (2), 583-587.

110. Fey, G. T. K.; Lu, C. Z.; Kumar, T. P.; Chang, Y. C., TiO_2 coating for long-cycling $LiCoO_2$: A comparison of coating procedures. *Surf. Coat. Technol.* **2005,** *199* (1), 22-31.

111. Pu, X.; Yin, L.; Yu, C., Functional surface modifications on nanostructured $LiCoO_2$ with lithium vanadates. *J. Nanopart. Res.* **2012,** *14* (4), 1-7.

112. (a) Jo, M.; Hong, Y. S.; Choo, J.; Cho, J., Effect of $LiCoO_2$ Cathode Nanoparticle size on high rate performance for Li-ion batteries. *J. Electrochem. Soc.* **2009,** *156* (6), A430-A434; (b) Scott, I. D.; Jung, Y. S.; Cavanagh, A. S.; An, Y. F.; Dillon, A. C.; George, S. M.; Lee, S. H., Ultrathin coatings on nano-$LiCoO_2$ for Li-ion vehicular applications. *Nano Lett.* **2011,** *11* (2), 414-418.

113. Yang, Z. X.; Yang, W. S.; Evans, D. G.; Li, G.; Zhao, Y. Y., Enhanced overcharge behavior and thermal stability of commercial $LiCoO_2$ by coating with a novel material. *Electrochem. Commun.* **2008,** *10* (8), 1136-1139.

114. Bruce, P. G.; Saidi, M. Y., The mechanism of electrointercalation. *J. Electroanal. Chem.* **1992,** *322* (1-2), 93-105.

115. Aurbach, D.; Levi, M. D.; Levi, E.; Teller, H.; Markovsky, B.; Salitra, G.; Heider, U.; Heider, L., Common electroanalytical behavior of Li intercalation processes into graphite and transition metal oxides. *J. Electrochem.Soc.* **1998,** *145* (9), 3024-3034.

116. Ji, X.; Nazar, L. F., Advances in Li-S batteries. *Journal of Materials Chemistry* **2010,** *20* (44), 9821-9826.

117. (a) Pu, X.; Yu, C., Enhanced overcharge performance of nano-$LiCoO_2$ by novel Li3VO4 surface coatings. *Nanoscale* **2012,** *4* (21), 6743-6747; (b) Pu, X.; Yin, L.; Yu, C., Functional surface modifications on nanostructured $LiCoO_2$ with lithium vanadates. *J Nanopart Res* **2012,** *14* (4), 1-7.

118. (a) Yin, L.; Wang, J.; Yang, J.; Nuli, Y., A novel pyrolyzed polyacrylonitrile-sulfur@MWCNT composite cathode material for high-rate rechargeable lithium/sulfur batteries. *Journal of Materials Chemistry* **2011,** *21* (19), 6807-6810; (b) Elazari, R.; Salitra, G.; Garsuch, A.; Panchenko, A.; Aurbach, D., Sulfur-impregnated activated carbon fiber cloth as a binder-free cathode for rechargeable Li-S batteries. *Adv. Mater.* **2011,** *23* (47), 5641-5644.

119. Yamin, H.; Penciner, J.; Gorenshtain, A.; Elam, M.; Peled, E., The electrochemical behavior of polysulfides in tetrahydrofuran. *J. Power Sources* **1985,** *14* (1–3), 129-134.

120. Jayaprakash, N.; Shen, J.; Moganty, S. S.; Corona, A.; Archer, L. A., Porous hollow carbon@sulfur composites for high-power lithium–sulfur batteries. *Angewandte Chemie International Edition* **2011,** *50* (26), 5904-5908.

121. Su, Y.-S.; Manthiram, A., Lithium–sulphur batteries with a microporous carbon paper as a bifunctional interlayer. *Nat Commun* **2012,** *3*, 1166.

122. Hassoun, J.; Kim, J.; Lee, D.-J.; Jung, H.-G.; Lee, S.-M.; Sun, Y.-K.; Scrosati, B., A contribution to the progress of high energy batteries: A metal-free, lithium-ion, silicon–sulfur battery. *J. Power Sources* **2012,** *202* (0), 308-313.

123. Kasavajjula, U.; Wang, C.; Appleby, A. J., Nano- and bulk-silicon-based insertion anodes for lithium-ion secondary cells. *J. Power Sources* **2007,** *163* (2), 1003-1039.

124. (a) Kovalenko, I.; Zdyrko, B.; Magasinski, A.; Hertzberg, B.; Milicev, Z.; Burtovyy, R.; Luzinov, I.; Yushin, G., A major constituent of brown algae for use in high-capacity Li-ion batteries. *Science* **2011,** *334* (6052), 75-79; (b) Koo, B.; Kim, H.; Cho, Y.; Lee, K. T.; Choi, N.-S.; Cho, J., A highly cross-linked polymeric binder for high-performance silicon negative electrodes in lithium ion batteries. *Angewandte Chemie International Edition* **2012,** *51* (35), 8762-8767.

125. (a) Elazari, R.; Salitra, G.; Gershinsky, G.; Garsuch, A.; Panchenko, A.; Aurbach, D., Rechargeable lithiated silicon–sulfur (SLS) battery prototypes. *Electrochem. Commun.* **2012,** *14* (1), 21-24; (b) Liu, N.; Hu, L.; McDowell, M. T.; Jackson, A.; Cui, Y., Prelithiated silicon nanowires as an anode for lithium ion batteries. *ACS Nano* **2011,** *5* (8), 6487-6493.

126. Yang, Y.; McDowell, M. T.; Jackson, A.; Cha, J. J.; Hong, S. S.; Cui, Y., New nanostructured Li_2S/silicon rechargeable battery with high specific energy. *Nano Letters* **2010,** *10* (4), 1486-1491.

127. Lang, J.W.; Yan, X.B.; Yuan, X.Y.; Yang, J.; Xue, Q.J., Study on the electrochemical properties of cubic ordered mesoporous carbon for supercapacitors. *J. Power Sources* **2011,** *196* (23), 10472-10478.

128. Yu, C.; Fan, J.; Tian, B.; Zhao, D., Morphology development of mesoporous materials: a colloidal phase separation mechanism. *Chem. Mat.* **2004,** *16* (5), 889-898.

129. Xu, W.; Wang, J.; Ding, F.; Chen, X.; Nasybulin, E.; Zhang, Y.; Zhang, J.-G., Lithium metal anodes for rechargeable batteries. *Energy & Environmental Science* **2014,** *7* (2), 513-537.

130. Su, Y.-S.; Manthiram, A., A new approach to improve cycle performance of rechargeable lithium-sulfur batteries by inserting a free-standing MWCNT interlayer. *Chem. Commun.* **2012,** *48* (70), 8817-8819.

131. Bang, H. J.; Kim, S.; Prakash, J., Electrochemical investigations of lithium-aluminum alloy anode in Li/polymer cells. *J. Power Sources* **2001,** *92* (1–2), 45-49.

132. Rauh, R. D.; Abraham, K. M.; Pearson, G. F.; Surprenant, J. K.; Brummer, S. B., A lithium/dissolved sulfur battery with an organic electrolyte. *J. Electrochem. Soc.* **1979,** *126* (4), 523-527.

133. (a) Yang, Y.; Zheng, G.; Cui, Y., A membrane-free lithium/polysulfide semi-liquid battery for large-scale energy storage. *Energy & Environmental Science* **2013,** *6* (5), 1552-1558; (b) Fan, F. Y.; Woodford, W. H.; Li, Z.; Baram, N.; Smith, K. C.; Helal, A.; McKinley, G. H.; Carter, W. C.; Chiang, Y.-M., Polysulfide flow batteries enabled by percolating nanoscale conductor networks. *Nano Letters* **2014**.

134. Barchasz, C.; Mesguich, F.; Dijon, J.; Leprêtre, J.-C.; Patoux, S.; Alloin, F., Novel positive electrode architecture for rechargeable lithium/sulfur batteries. *J. Power Sources* **2012,** *211* (0), 19-26.

135. Demir-Cakan, R.; Morcrette, M.; Gangulibabu; Gueguen, A.; Dedryvere, R.; Tarascon, J.-M., Li-S batteries: simple approaches for superior performance. *Energy & Environmental Science* **2013,** *6* (1), 176-182.

136. Fu, Y.; Su, Y.-S.; Manthiram, A., Highly reversible lithium/dissolved polysulfide batteries with carbon nanotube electrodes. *Angewandte Chemie International Edition* **2013,** *52* (27), 6930-6935.

137. Gui, X.; Wei, J.; Wang, K.; Cao, A.; Zhu, H.; Jia, Y.; Shu, Q.; Wu, D., Carbon Nanotube Sponges. *Adv. Mater.* **2010,** *22* (5), 617-621.

138. Gui, X.; Zeng, Z.; Zhu, Y.; Li, H.; Lin, Z.; Gan, Q.; Xiang, R.; Cao, A.; Tang, Z., Three-dimensional carbon nanotube sponge-array architectures with high energy dissipation. *Adv. Mater.* **2014,** *26* (8), 1248-1253.

139. Hata, K.; Futaba, D. N.; Mizuno, K.; Namai, T.; Yumura, M.; Iijima, S., Water-assisted highly efficient synthesis of impurity-free single-walled carbon nanotubes. *Science* **2004,** *306* (5700), 1362-1364.

140. Patole, S. P.; Alegaonkar, P. S.; Shin, H. C.; Yoo, J. B., Alignment and wall control of ultra long carbon nanotubes in water assisted chemical vapour deposition. *Journal of Physics D-Applied Physics* **2008,** *41* (15).